Aluminum-induced Crystallization of Semiconductor Thin Films

Von der Fakultät Chemie der Universität Stuttgart
zur Erlangung der Würde eines Doktors der Naturwissenschaften
(Dr. rer. nat.) genehmigte Abhandlung

Vorgelegt von
Fei Qu
aus Tongling, V. R. China

Hauptberichter: Prof. Dr. Guido Schmitz
Mitberichter: Prof. Dr. Joachim Bill

Tag der mündlichen Prüfung: 28. Oktober 2015

Institut für Materialwissenschaft der Universität Stuttgart
2015

Abstract

Thin film materials of the semiconductors, such as silicon (Si), germanium (Ge) or their alloys, are turning into the most promising functional materials in the energy technology. However, the morphologies of these semiconductor thin films must be varied to be suitable for the different applications, e.g. a large-grained layer as the seed layer of thin film solar cells, a porous structure for anode materials of high energy rechargeable lithium (Li) ion batteries. Due to the collective interdiffusion process during the aluminum (Al)-induced crystallization, in this thesis, the suitable morphologies are achieved for the corresponding applications under the different fabrication conditions.

A large-grained Si layer can be formed by the crystallization of Si in a porous Al layer, which is obtained by applying a bias voltage. Since the Al grain boundaries are contaminated by e.g. oxygen (O), the diffusion of Si in the Al grain boundaries is retarded. It can lead to a reduction of the nucleation density of Si. At a certain high temperature, a collective diffusion process of Si in Al is activated. Consequently, a large-grained Si layer with (100) texture can be formed.

By purposely interrupting the annealing of nanocrystalline Al/amorphous Si (a-Si) bilayers, a porous structure of the crystallized Si can be developed due to the incomplete intermixing of Si and Al. Due to the different dominant diffusion processes of Si in Al at the different annealing temperatures, the most Si diffuses along the different paths in the Al layer, such as triple junction, grain boundary and Al bulk. Therefore, it can develop the different morphologies of the porous Si layers after the selectively etching of Al.

By introducing an amorphous Ge interlayer between the crystalline Al and amorphous Si layer, the Al grain boundaries are not essential for the crystallization of the amorphous Si in contrast to the case in Al/Si bilayer system. Si crystallizes continuously on the pre-crystallized Ge seeds which form initially at the original interface of crystalline Al and amorphous Ge.

The thermodynamic models to interpret the fundamentals of these different crystallization behaviors of Si are established based on the change of the interface energy between the different phases of the whole system during the crystallization. Using the effective diffusivity, the

dominant diffusion process of Si in Al can be investigated to explore the morphological dependence of the crystallized Si layer on the annealing conditions.

Zusammenfassung

Dünnschichtmaterialien vom Halbleiter, z.B. Silizium (Si), Germanium (Ge) oder ihre Legierungen, werden als die angemessenen Funktionsmaterialien in Energietechnologie angewendet. Je nach den Anwendungen muss sich die Morphologie dieser Dünnschichthalbleiter eignen, wie zum Beispiel eine grobkörnige Schicht als die Keimschicht für die Herstellung der Dünnschichtsolarzelle, eine poröse Struktur als Anodenmaterial für die Lithium-Ionen-Batterie mit einer hohen Energiedichte. Während der Aluminium-induzierten Kristallisation der amorphen Halbleiter findet ein kollektiver Interdiffusionsprozess statt. In dieser Arbeit wird die je nach den Anwendungen gezielte Morphologie der Halbleiterdünnschichten über diese Methode unter den unterschiedlichen Herstellungsbedingungen erlangt.

Eine grobkörnige Si-Schicht kann durch die Kristallisation in einer porösen Al-Schicht, die mit einer Biasspannung hergestellt wurde, gebildet werden. Die Al Korngrenzen in dieser porösen Al-Schicht werden wie zum Beispiel durch Sauerstoff (O) kontaminiert. Deshalb wird die Diffusion von Si in den Al Korngrenzen verlangsamt. Es führt zu einer Abnahme der Keimbildungsdichte vom Si. Höher als eine bestimmte Auslagerungstemperatur wird ein kollektiver Diffusionsprozess aktiviert. Daraus folgt, dass sich diese grobkörnige Si-Schicht mit (100) orientierter Textur bildet.

Über eine gezielte Unterbrechung der Wärmebehandlung von Proben mit einer nanokristallines Al/amorphes Si Doppelschichtstruktur kann sich eine poröse Struktur vom kristallisierten Si nach dem Wegätzen von Al bilden, weil der Interdiffusionsprozess von Al und Si in der Zwischenzeit abbricht. Bei verschiedenen Auslagerungstemperaturen diffundiert das meiste Si entlang den unterschiedlichen Wegen in Al-Schicht, z.B. Trippellinien, Korngrenzen und Al-Körner. Die unterschiedlichen dominierten Diffusionsprozesse von Si in Al variieren die gebildete Morphologie von der porösen Si-Schicht.

Über die Anwesenheit einer Zwischenschicht vom amorphen Ge zwischen der kristallinen Al- und amorphen Si-Schicht spielen die Al Korngrenzen keine entscheidende Rolle mehr für die Kristallisation vom amorphen Si im Vergleich zu dem Fall vom Al/Si Doppelschichtsystem. Si kristallisiert kontinuierlich auf den vorkristallisierten Ge Kristalliten, die sich zuerst an der ehemaligen Grenzfläche vom kristallinen Al und amorphen Ge bilden können.

Die Fundamente, die die unterschiedlichen Kristallisationsverhaltene von Si thermodynamisch interpretieren können, werden anhand der Änderung der Grenzflächenenergien zwischen den unterschiedlichen Phasen im ganzen System während der Kristallisation aufgebaut. Mit der effektiven Diffusivität wird der dominierte Diffusionsprozess von Si in Al in den unterschiedlichen Temperaturintervallen ermittelt. Dadurch kann der Einfluss der Auslagerungsbedingung auf der Morphologie vom kristallisierten Si erkundet werden.

Content

Chapter 1
Introduction

Nowadays many different methods are developed to find out a simple way of the crystallization of amorphous semiconductor materials, such as silicon (Si), germanium (Ge) or Si_xGe_{1-x} alloys. Generally, the amorphous phase can transit irreversibly to the crystalline phase, provided it is, e.g., heated up to a certain high temperature (e.g. for Si above 700 °C and for Ge above 450 °C).[1-3] Based on this method, some technologies were developed, e.g. solid phase crystallization (SPC) [4-7] and excimer laser crystallization (ELC).[8-11] However, these technologies are hardly for some substrates with favorable functionalities, such as conductive polymers, due to the modification or even loss of their functionalities or to decomposition at such high temperatures. Metal-induced crystallization was adopted to be an alternative method lowering the crystallization temperature of the amorphous semiconductor materials.[12] Many different metals or alloys can be chosen as the crystallization inducer, e.g. aluminum (Al), [13-15], gold (Au),[16-19] nickel (Ni),[20, 21] titanium (Ti),[22] silver-copper (Ag-Cu) alloy.[23]

Since last century, Al has also become a forerunner for the crystallization of amorphous Si, Ge and their alloys. Compare to the other metals or alloys, Al has many advantages as the crystallization inducer. First, due to the little solubility of Al in Si, Ge and their alloys, there is no formation of intermetallic phases. Second, Al, as a dopant for these semiconductor materials, can improve the conductivity of these semiconductor materials through a post treatment.[24] Third, Al is one of the most abundant elements in the crust. Fourth, as one of the amphoteric metals, Al can be easily etched off either by acids or by bases.

In this work, by varying the character of the Al layers and post treatment conditions, different crystallization mechanisms induced by Al in these semiconductor thin films will be elaborated, as well as the various morphological structures that can be tailored to fit optimally the functions suitable to be used in the different applications of energy technology.

1.1 Seed Layer for thin film solar cells

The normally low angle grain boundaries or the high-Σ coincidence site lattice (CSL) boundaries and the contaminations in them generally cause a high recombination activity between conducting electrons and holes.[25] Therefore, in order to fabricate Si thin film solar cells with high efficiency, Si grains as large as possible are needed. However, by the direct deposition of Si on foreign substrates, the resulting Si layers possess usually small grains and poor crystallographic quality.[26] As a consequence, an initial step is needed to earn a thin Si layer with large grains (> 10 μm) and good crystallographic quality to be usable as a seed layer for further epitaxial thickening of Si to a few tens of micrometers.

There are two prominent techniques which can be used to fabricate a Si seed layer: laser crystallization and metal-induced crystallization.[12, 27, 28] Laser crystallization is still not suitable for industrial application due to the low productivity (scanning over the whole area with a narrow beam is usually slow) and high maintenance costs. In comparison with laser crystallization, metal-induced crystallization achieves the lowering of the crystallization temperature of amorphous Si with low maintenance costs and little limit on the geometry of the area. It can be a potential solution for the industrial application.

Since last century, the researchers have found several candidates to be applied for the crystallization of Si with large grains, e.g. Au,[17] Ni,[12, 20] Ag,[29] etc.. However, many undesired grain boundaries (the normal low-angle grain boundaries or the high-Σ CSL boundaries) are formed in the Si films created by these metals. In addition, all these metals can either form an intermetallic phase with Si or contaminate the Si grains heavily.[30] Such a contamination leads to the recombination between the conducting electrons and holes, as well as to the lowering of the efficiency of the Si thin film solar cells. On the contrary, Al acts as an acceptor dopant in Si, forms no intermetallic phase and diffuses in bulk Si relatively slowly. Thus, it is considered to be the best candidate of the metal-induced crystallization progress for forming the Si seed layer.

The morphology of the crystallized Si layer depends on the character of Al layers. Generally, the enlarging of Al grains is beneficial for crystallization of Si into the large grains.[31] Furthermore, an Al oxide buffer layer between Al and Si layer as diffusion barrier can also enhance the crystallization of amorphous Si into the large grains.[32] Usually, the crystallized Si, which is induced by an Al layer and used as seed layer, possesses the average grain size about 10 to 15 μm.[32-34] However, it is still a challenge to get even larger Si grains.

In this work, we explored the crystallization of amorphous Si by using the Al layers with very different morphology. Instead of using a compact Al layer as usual, a porous Al layer is de-

veloped by applying an extra bias voltage during the deposition. Compared to the generally applied crystallization of Si induced by a compact Al layer, the nucleation density of Si in such porous Al layers is reduced and the grain size distribution in this case becomes significantly wider. With the aid of an Al oxide layer, Si can crystallize into even larger grains. The average grain size we have reached in this case can was even larger than 20 μm.

1.2 Anode material for Li ion batteries

In addition to the Si solar cell technology, Si-based materials as typical anode materials are attractive candidates for the high capacity energy storage in Li ion battery (4200 mAh/g), exceeding that of the widely used graphite insertion anode (372 mAh/g) by more than a factor of 10.[35]

Unfortunately, during the lithiation of a Si anode, a high volume expansion (~ 300 % for a-Si[36] and ~ 400 % for c-Si[35]) occurs. It leads to electrode pulverization/delamination, electrical contact loss and early capacity degradation. As observed in 1 μm thick samples, the capacity of continuous Si thin films fades seriously after several cycles with repeating volume expansion and contraction.[37] According to the lithiation-induced deformation in Si lattice, *K. J. Zhao* et al. suggested a theoretical critical dimension size of Si (130 nm), to solve these problems.[38] This prediction agreed well with the experimental observation.[39, 40] Therefore, Si nanostructures have been exploited, such as nanopowder, nanowires and nanoparticles.[41-43]

In addition, during the lithiation, Si reacts with the organic electrolyte and forms an unstable inherent solid electrolyte interphase (SEI phase).[44] This irreversible reaction leads to the lowering of coulombic efficiency. In order to overcome this problem, surface coating to create an artificial passivation layer on Si, e.g. an conformal auxiliary Al oxide layer, has been proven to be an effective approach.[45]

To get the better performance of the Si anode, effective binders/additives are also used to be applied alternative strategies, such as fluoroethylene carbonate (FEC), carboxymethyl cellulose (CMC) and polyacrylic acid (PAA).[46-48]

Unfortunately, for the green productions or commercial industrial fabrication, these above-mentioned conventional solutions are not suitable, due to the demand of the dangerous chemicals (e.g. hydrofluoric acid) to generate the nanostructure or extra chemicals as additive and binder. The extra coating process of Al oxide layer with controllable nanometer thickness is typically realized by atomic layer deposition (ALD) which brings more costs. Due to these impediments, the application of Si anodes for Li ion batteries stays nowadays still at the experimental stage.

As usual, Al-induced crystallization of amorphous Si was widely applied to produce a continuous polycrystalline layer as seed layer for thin film solar cells. In this work, different to the other traditional methods, we develop a porous Si layer by Al-induced crystallization with purposely interrupting the post treatment. These procedures require a very thorough analysis of the diffusion currents and reaction kinetics during the various processing steps. As will be seen, after an almost final selective etch of Al with the alkali solution, a conformal auxiliary oxide layer with several nanometers is formed concomitantly on the nano-structured Si layer. This produced Si layer prevents the deleterious SEI layer to form and thus optimally satisfies the structural and functional demands as an anode material for lithium ion batteries. Due to the continuity and conveniency of this method, it can be a potential solution for the industrial manufacturing of Si anode.

1.3 Fundamental research on Al/Ge/Si trilayer system

By inducing an Al layer, the crystallization temperature of Si is decreased to 165 °C,[49] however, it is still too high for substrates with favorable functionalities but lower maximum processing temperature, e.g. the conductive polymers. On the other hand, in order to realize energy-efficient fabrication, it is desirable to reduce the crystallization temperature as much as possible.

Due to the lower crystallization temperature of Ge in an Al layer and the complete miscibility between Si and Ge,[50, 51] in this work, an amorphous Ge layer between the crystalline Al and amorphous Si layer is incorporated to change the crystallization temperature and mechanism of Si. A thermodynamic model is developed to interpret the crystallization of Si in this trilayer systems as well as to estimate the crystallization temperature of Si in this case.

Chapter 2

Al-induced Crystallization

Meta-induced crystallization of amorphous semiconductor thin films, preferentially Si, Ge or their alloys films, mostly by using of an Al layer has attracted considerable interest in recent decades.[13, 14, 52] X-ray diffraction has proved that Al can induce the crystallization of these amorphous semiconductor materials below their eutectic temperature (e.g. for Si 577 °C and for Ge 424 °C).[13, 53] Combining the experimental results by valence energy-filtered transmission electron microscope (VEFTEM) and the thermodynamic calculation, *Z. M. Wang* established a model to explain the process of Al-induced crystallization.[50, 54] According to this proposition, the whole process can be divided into three steps: 1) Al grain boundary wetting by amorphous semiconductors; 2) interface or grain boundary nucleation of semiconductor crystals; 3) continued crystallization of semiconductors.[50] In this chapter, the fundamentals about the Al-induced crystallization of amorphous Si and Ge layer will be explained.

2.1 Grain boundary wetting by amorphous semiconductors

Compared to the covalent bonds in the bulk a-Si (or a-Ge), the bonds between the Si (or Ge) atoms at the interface with the Al layer are weakened due to the screening effect by the free electrons in Al layer.[55] These relative weakly bonded Si (or Ge) atoms are named here 'free' atoms. Since the activation energy for the diffusion of these interface-adjacent 'free' atoms are reduced, the mobility of these atoms is much higher than that of the atoms in the bulk a-Si (or a-Ge). These atoms can easily diffuse along the different interfaces, e.g. the Al grain boundaries or the a-Si (or a-Ge)/c-Al interfaces. In case the Al grain boundaries can be wetted by the segregation of the 'free' Si (or Ge) atoms due to the energetic favorable conditions, these short circuit diffusion paths can provide the heterogeneous sites for the nucleation of these amorphous phases at the low temperatures.[15, 56]

By the diffusion of the 'free' Si (or Ge) atoms into the Al grain boundaries, two new a-Si (or a-Ge)/c-Al interfaces may form replacing one original c-Al/c-Al interface (Fig. 2.1). Thermodynamically, if the total energy of the newly formed interfaces between a-Si (or a-Ge) and c-Al ($\gamma^{\text{interf}}_{\langle Al\rangle/\{Si\}}$ or $\gamma^{\text{interf}}_{\langle Al\rangle/\{Ge\}}$) is lower than the original c-Al grain boundary energy ($\gamma^{\text{GB}}_{\langle Al\rangle}$), the Al-grain boundaries can be wetted by the second phase of amorphous semiconductors.[57] Otherwise, the 'free' atoms would like to diffuse through the Al grain boundaries and segregate on the surface of Al layer.
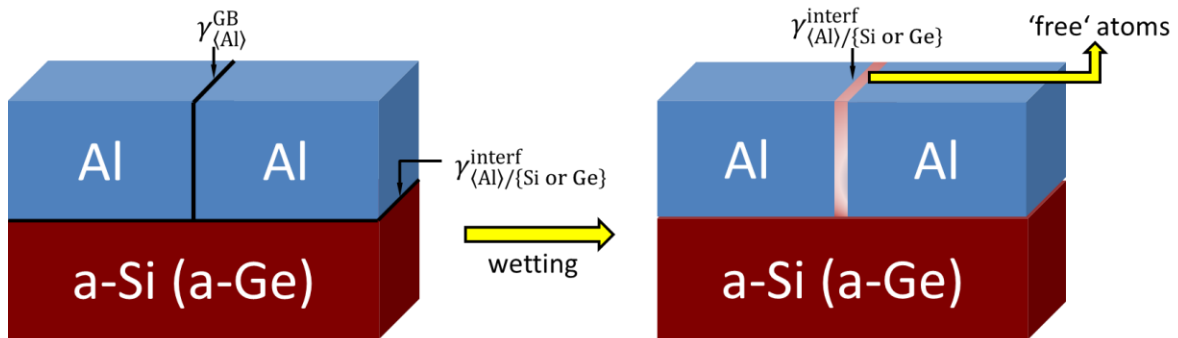
Fig. 2.1   Wetting in the Al grain boundaries by the 'free' Si or Ge atoms

Fig. 2.2 plots the calculated Al grain boundary energy $\gamma^{\text{GB}}_{\langle Al\rangle}$ and the newly formed interface energy between crystalline Al and amorphous semiconductors ($2 \times \gamma^{\text{interf}}_{\langle Al\rangle/\{Si\}}$ or $2 \times \gamma^{\text{interf}}_{\langle Al\rangle/\{Si\}}$) in dependence of the temperature. The original Al grain boundary energy $\gamma^{\text{GB}}_{\langle Al\rangle}$ is higher than the total interface energy $2 \times \gamma^{\text{interf}}_{\langle Al\rangle/\{Si\}}$ (red curve in Fig. 2.2) or likewise $2 \times \gamma^{\text{interf}}_{\langle Al\rangle/\{Ge\}}$ (blue curve in Fig. 2.2).[50] .
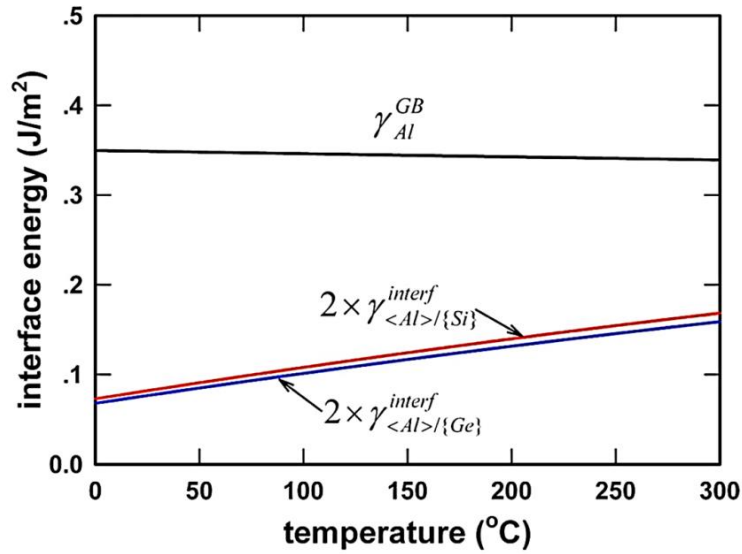
Fig. 2.2   **The total interface energy before and after the wetting with the 'free' Si and Ge atoms: black line: the original c-Al grain boundary energy; red line: total newly formed interface energy between a-Si and c-Al; blue line: total newly formed interface energy between a-Ge and c-Al. Both differences between before and after wetting with Si or Ge atoms i.e. the driving force for wetting are positive. Thereby, the Al grain boundaries may be wetted by the 'free' Si or Ge atoms to reduce the total interface energy. [50]**

The a-Si/c-Al interface energy is slightly higher than that of a-Ge/c-Al interface. The driving force for the Al grain boundary wetting by a-Si or a-Ge phase ($\Delta\gamma_{\mathrm{D}}^{\mathrm{Si\ in\ Al\ GB}}$ or $\Delta\gamma_{\mathrm{D}}^{\mathrm{Ge\ in\ Al\ GB}}$) can be described by:

$$\Delta\gamma_{\mathrm{D}}^{\mathrm{Si\ in\ Al\ GB}} = \gamma_{\langle\mathrm{Al}\rangle}^{\mathrm{GB}} - 2\gamma_{\langle\mathrm{Al}\rangle/\{\mathrm{Si}\}}^{\mathrm{interf}} \qquad\qquad \text{Eq. 1}$$

$$\Delta\gamma_{\mathrm{D}}^{\mathrm{Ge\ in\ Al\ GB}} = \gamma_{\langle\mathrm{Al}\rangle}^{\mathrm{GB}} - 2\gamma_{\langle\mathrm{Al}\rangle/\{\mathrm{Ge}\}}^{\mathrm{interf}} \qquad\qquad \text{Eq. 2}$$

The positive values of $\Delta\gamma_{\mathrm{D}}^{\mathrm{Si\ in\ Al\ GB}}$ or $\Delta\gamma_{\mathrm{D}}^{\mathrm{Ge\ in\ Al\ GB}}$ satisfy the wetting condition of the Al grain boundaries by the 'free' Si or Ge atoms and reduce the total system energy

2.2 Interface and grain boundary nucleation of semiconductor crystals

Without the aid of Al, the phase transformation from amorphous Si or Ge to their crystalline phases could occur only at temperatures above 700 °C for Si and 500 °C for Ge.[1] Therefore, the homogeneous nucleation in the bulk a-Si or a-Ge is impossible at the lower temperatures. But the 'free' Si or Ge atoms, which diffuse into the Al grain boundaries or at the interface between c-Al and amorphous Si or Ge, could form nuclei heterogeneously at the lower tem-

peratures (Fig. 2.3). Due to the interface energy between the crystalline Al and amorphous semiconductors ($\gamma^{\text{interf}}_{\langle\text{Al}\rangle/\{\text{Si}\}}$ or $\gamma^{\text{interf}}_{\langle\text{Al}\rangle/\{\text{Ge}\}}$) being lower than that between the crystalline Al and crystalline semiconductors ($\gamma^{\text{interf}}_{\langle\text{Al}\rangle/\langle\text{Si}\rangle}$ or $\gamma^{\text{interf}}_{\langle\text{Al}\rangle/\langle\text{Ge}\rangle}$), the amorphous semiconductors are thermodynamically stable at first. At a critical thickness, however, the differences between the interface energy due to the amorphous and crystalline semiconductor phases can be compensated by the crystallization of the amorphous semiconductor phases.
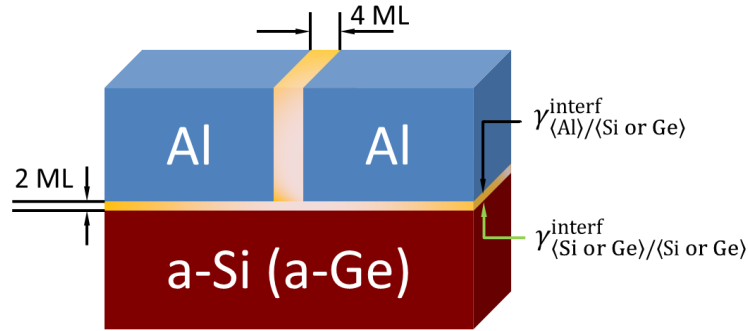
Fig. 2.3   **The nucleation possibilities for the crystalline phase by Al-induced crystallization: 2 mono layers (2 ML) at the interface between a-Si and c-Al; 4 mono layer(4 ML) in the c-Al grain boundaries**

There are two nucleation possibilities for Si or Ge, at the Al grain boundaries or at the interface between c-Al and a-Si (or a-Ge). As a consequence of the two newly formed interfaces between Al and the semiconductor phases at the Al grain boundaries (Fig. 2.3), the critical thicknesses for the nucleation of a-Si and a-Ge at the Al grain boundaries can be expressed by:

$$h^{\text{crit}}_{\text{Si at Al GB}} = \frac{2 \cdot \left(\gamma^{\text{interf}}_{\langle\text{Al}\rangle/\langle\text{Si}\rangle} - \gamma^{\text{interf}}_{\langle\text{Al}\rangle/\{\text{Si}\}}\right)}{-\Delta G^{\text{cryst}}_{\langle\text{Si}\rangle-\{\text{Si}\}}} \qquad \text{Eq. 3}$$

$$h^{\text{crit}}_{\text{Ge at Al GB}} = \frac{2 \cdot \left(\gamma^{\text{interf}}_{\langle\text{Al}\rangle/\langle\text{Ge}\rangle} - \gamma^{\text{interf}}_{\langle\text{Al}\rangle/\{\text{Ge}\}}\right)}{-\Delta G^{\text{cryst}}_{\langle\text{Ge}\rangle-\{\text{Ge}\}}} \qquad \text{Eq. 4}$$

Analogously to the case of the nucleation of amorphous semiconductors at the interface with Al, the critical thickness for the nucleation at the interface between the c-Al and amorphous semiconductors can be described by:

$$h^{\text{crit}}_{\langle\text{Al}\rangle/\{\text{Si}\}} = \frac{\gamma^{\text{interf}}_{\langle\text{Al}\rangle/\langle\text{Si}\rangle} + \gamma^{\text{interf}}_{\langle\text{Si}\rangle/\{\text{Si}\}} - \gamma^{\text{interf}}_{\langle\text{Al}\rangle/\{\text{Si}\}}}{-\Delta G^{\text{cryst}}_{\langle\text{Si}\rangle-\{\text{Si}\}}} \qquad \text{Eq. 5}$$

$$h_{\langle Al \rangle/\{Ge\}}^{crit} = \frac{\gamma_{\langle Al \rangle/\langle Ge \rangle}^{interf} + \gamma_{\langle Ge \rangle/\{Ge\}}^{interf} - \gamma_{\langle Al \rangle/\{Ge\}}^{interf}}{-\Delta G_{\langle Ge \rangle-\{Ge\}}^{cryst}} \qquad Eq.\,6$$
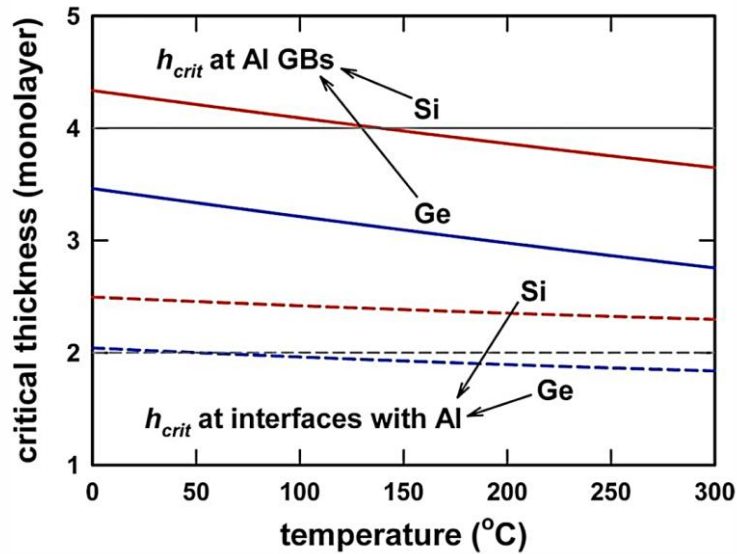
Fig. 2.4   **Critical thickness for nucleation as the function of temperature: the red solid line: the critical thickness for the nucleation of Si at Al grain boundaries; the blue solid line: the critical thickness for the nucleation of Ge at Al grain boundaries; grey solid line: the thickness of the wetting layer by the a-Si or a-Ge at Al grain boundaries; the red dotted line: the critical thickness for the nucleation of Si at the interface between a-Si and c-Al; the blue dotted line: the critical thickness for the nucleation of Si at the interface between a-Ge and c-Al; grey dotted line: the thickness of the wetting layer by the a-Si or a-Ge at the a-Si (or a-Ge)/c-Al interface [50]**

Fig. 2.4 shows the curves of the critical thicknesses for nucleation as a function of temperature. *Z. M. Wang* et al. assumed that the thickness of the wetting layer at the interface between the a-Si or a-Ge and c-Al is 2 monolayers (2 ML), while that in the Al grain boundaries is 2×2 monolayers (4 ML) (Fig. 2.3).[50] The critical thickness for nucleation of Si at the c-Al/a-Si interface is larger than 2 ML (red dotted line in Fig. 2.4). Therefore, Si cannot nucleate there. Exceeding a certain temperature i.e. about 150 °C, the critical thickness for the nucleation of a-Si at Al grain boundaries will be less than 4 ML (red solid curve in Fig. 2.4). Consequently, a-Si may nucleate at the Al grain boundaries above this temperature. Comparatively, the critical thicknesses for the nucleation of a-Ge for the both possibilities are less than the thickness of the a-Ge wetting layer (blue curves in Fig. 2.4). Thus, Ge can crystallize either at a-Si/c-Al interface or at Al grain boundaries.

2.3 Continued crystallization of semiconductors

After the initial crystallization, the 'free' Si atoms may further diffuse into the c-Al/c-Si interface to reduce the total system energy by the newly formed a-Si/c-Al and a-Si/c-Si interfaces (Fig. 2.5). The same holds for the Ge/Al system. The driving force for the further wetting is given by:

$$\Delta\gamma_{\mathrm{D}}^{\mathrm{Si\ in\ }\langle Al\rangle/\langle Si\rangle} = \gamma_{\langle Al\rangle/\langle Si\rangle}^{\mathrm{interf}} - \left(\gamma_{\langle Al\rangle/\{Si\}}^{\mathrm{interf}} - \gamma_{\langle Si\rangle/\{Si\}}^{\mathrm{interf}}\right) \qquad \text{Eq. 7}$$

$$\Delta\gamma_{\mathrm{D}}^{\mathrm{Ge\ in\ }\langle Al\rangle/\langle Ge\rangle} = \gamma_{\langle Al\rangle/\langle Ge\rangle}^{\mathrm{interf}} - \left(\gamma_{\langle Al\rangle/\{Ge\}}^{\mathrm{interf}} - \gamma_{\langle Ge\rangle/\{Ge\}}^{\mathrm{interf}}\right) \qquad \text{Eq. 8}$$

The positive driving force indicates that the further wetting by the 'free' Si (or Ge) is energetic favorable.
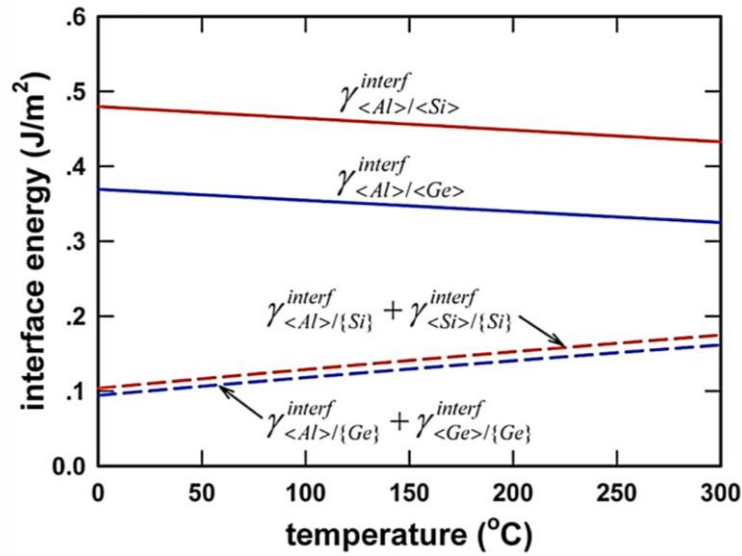
Fig. 2.5 **The total interface energy of continued wetting at the c-Si/c-Al (or c-Ge/c-Al) interface with the Si (or Ge) 'free' atoms: the red solid line: the interface energy between c-Si and c-Al; the blue solid line: the interface energy between c-Ge and c-Al; red dotted line: the total interface energy of the by 'free' Si atoms wetted c-Si and c-Al interface; blue dotted line: the total interface energy of the by 'free' Ge atoms wetted c-Ge and c-Al interface [50]**

Similar to the cost of initial crystallization, this further wetting by the amorphous Si or Ge is thermodynamically stable until to a critical thickness, where beyond the wetting layer begins to crystallize also. There are two possibilities for the further crystallization of the wetting phases, which is located between the c-Si (or c-Ge)/c-Al layers (Fig. 2.6 left): 1) continuous crystallization at the c-Si (or c-Ge)/c-Al interface (Fig. 2.6 middle); 2) new nucleation of Si (or c-Ge) at the c-Si (or c-Ge)/c-Al interface (Fig. 2.6 right).
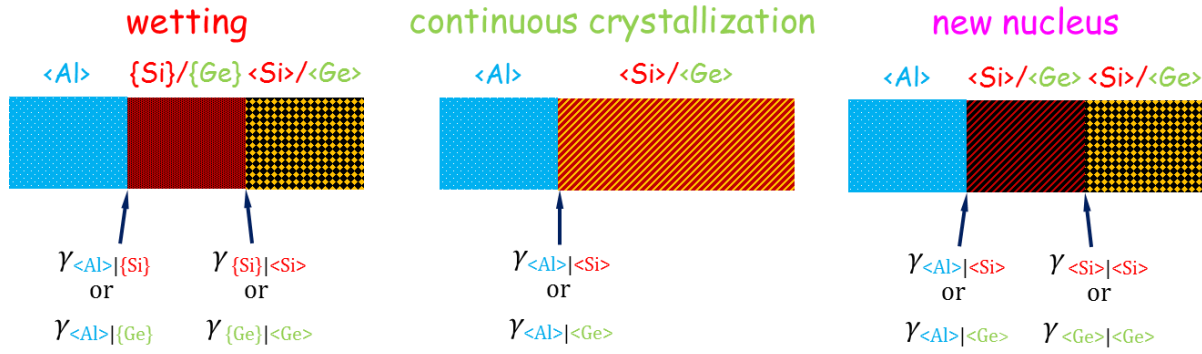
Fig. 2.6 **Two possibilities for the continued crystallization after the further wetting by the amorphous phase: a) continued crystallization at the c-Si (or c-Ge)/c-Al interphase boundaries; b) new nucleation at the c-Si (or c-Ge)/c-Al interfaces.**

Analogously to the calculation of the critical thickness for the nucleation of the amorphous semiconductors, the critical thickness for the continuous crystallization of a-Si and a-Ge can be described by:

$$h_{\text{Si grain growth}}^{\text{crit}} = \frac{\gamma_{\langle\text{Al}\rangle/\langle\text{Si}\rangle}^{\text{interf}} - \left(\gamma_{\langle\text{Al}\rangle/\{\text{Si}\}}^{\text{interf}} + \gamma_{\langle\text{Si}\rangle/\{\text{Si}\}}^{\text{interf}}\right)}{-\Delta G_{\langle\text{Si}\rangle-\{\text{Si}\}}^{\text{cryst}}} \qquad \text{Eq. 9}$$

$$h_{\text{Ge grain growth}}^{\text{crit}} = \frac{\gamma_{\langle\text{Al}\rangle/\langle\text{Ge}\rangle}^{\text{interf}} - \left(\gamma_{\langle\text{Al}\rangle/\{\text{Ge}\}}^{\text{interf}} + \gamma_{\langle\text{Ge}\rangle/\{\text{Ge}\}}^{\text{interf}}\right)}{-\Delta G_{\langle\text{Ge}\rangle-\{\text{Ge}\}}^{\text{cryst}}} \qquad \text{Eq. 10}$$

Similar to the previous case, the critical thickness for the new nucleation of a-Si and a-Ge can be calculated by:

$$h_{\text{Si new nucleation}}^{\text{crit}} = \frac{\left(\gamma_{\langle\text{Al}\rangle/\langle\text{Si}\rangle}^{\text{interf}} + \gamma_{\langle\text{Si}\rangle/\langle\text{Si}\rangle}^{\text{interf}}\right) - \left(\gamma_{\langle\text{Al}\rangle/\{\text{Si}\}}^{\text{interf}} + \gamma_{\langle\text{Si}\rangle/\{\text{Si}\}}^{\text{interf}}\right)}{-\Delta G_{\langle\text{Si}\rangle-\{\text{Si}\}}^{\text{cryst}}} \qquad \text{Eq. 11}$$

$$h_{\text{Ge new nucleation}}^{\text{crit}} = \frac{\left(\gamma_{\langle\text{Al}\rangle/\langle\text{Ge}\rangle}^{\text{interf}} + \gamma_{\langle\text{Ge}\rangle/\langle\text{Ge}\rangle}^{\text{interf}}\right) - \left(\gamma_{\langle\text{Al}\rangle/\{\text{Ge}\}}^{\text{interf}} + \gamma_{\langle\text{Ge}\rangle/\{\text{Ge}\}}^{\text{interf}}\right)}{-\Delta G_{\langle\text{Ge}\rangle-\{\text{Ge}\}}^{\text{cryst}}} \qquad \text{Eq. 12}$$

The critical thickness for the new nucleation of a-Si (or a-Ge) is larger than the thickness of the wetting layer by the 'free' Si (or Ge) atoms, 2 ML (Fig. 2.7). In this case, it is thermodynamically unfavorable for the new nucleation of the amorphous semiconductors at the interface between the crystalline Al and the crystallized semiconductors. In the case of the continuous crystallization, there is less than 2 ML needed. Thus, the amorphous phase crystallizes continuously on the preexisting crystallites.
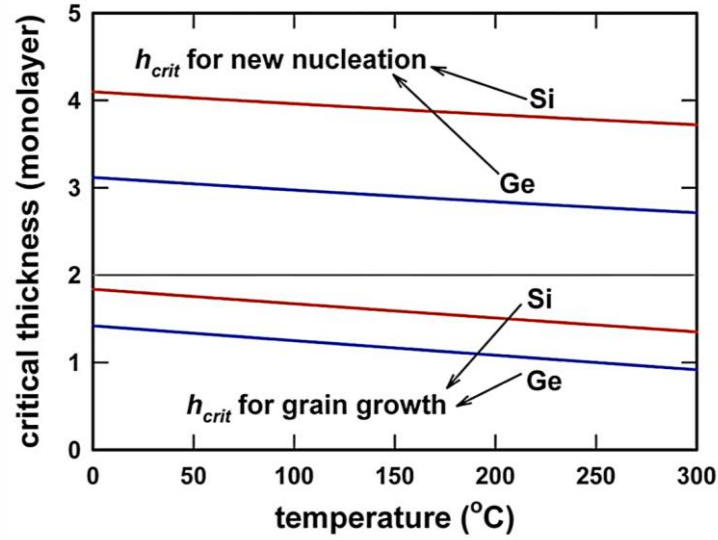
Fig. 2.7   **Critical thickness for the continued crystallization as a function of temperature: red solid line: continued crystallization of a-Si; blue solid line: continued crystallization of a-Ge; grey solid line: the thickness of the wetting layer by the a-Si or a-Ge [50].**

Combined with section 2.2, the grain growth of Si is restricted to the preexisting nuclei that crystallized at the Al grain boundaries. Comparatively, Ge grows simultaneously on both types of nuclei formed at the Al grain boundaries and at the a-Ge/c-Al interface. Consequently, a-Ge crystallizes kinetically faster than a-Si at the same temperature.

Chapter 3

Sample Characterization

The physical and chemical properties of the samples in this work were investigated with different methods, such as morphological structures, crystallographic information, chemical compositions and electrochemical performances. The experimental setup of these different characterization methods will be provided in this chapter.

3.1 Morphological characterization

3.1.1 Scanning electron microscopy

To investigate the surface morphology, scanning electron microscopy (SEM) is a good candidate besides the conventional optical microscopy. Compared to the optical microscopy, the resolution of the SEM equipment can reach down to the nanometer scale. Using the corresponding detectors for the different signals, such as the secondary electrons, backscattered electrons, the surface of the sample could be investigated to get different information, e.g. material contrast, surface topology. In this work all the specimens were investigated by a Carl Zeiss LEO 1530-VP microscope. The accelerating voltage was chosen between 3 to 20 kV.

3.1.2 Focused ion beam

Besides scanning electron microscopy (SEM), focused ion beam (FIB) can also image the surface morphology of the samples. Instead of the electron beam in SEM, the Ga-ion beam is used as the beam source in FIB. The gallium (Ga) ions possess a much higher kinetic energy due to their much larger mass. Therefore, the surface of the sample could be easily etched by the Ga-ion beam with a certain high current. The lower current was chosen to image the surface morphology or the microstructure of the cross-section. The cross-sectional images in this work were operated by FIB200 from company Fei. For the ionic etching and polishing the current was adjusted to 1000 pA and 150 pA respectively, while it was varied from 4 to 11 pA to image the surface or cross-sections. The whole process was operated at an accelerating voltage of 30 kV.

3.1.3 Transmission electron microscopy

To investigate the samples with an atomic scale, high resolution atomic images of the samples were obtained by the high resolution transmission electron microscopy (HRTEM) with JEOL 4000FX microscope. With this measurement method the crystalline phases can be graphically differed to the amorphous phases. The whole processes were operated at an acceleration voltage of 400 kV.

3.2 Crystallographic characterization

3.2.1 X-ray diffraction

X-ray diffraction (XRD) is one of the nondestructive analysis techniques used for the material science. With this characterization method the crystallographic information about the crystallinity, texture as well as the lattice structure of the sample can be directly analyzed by the

peaks' positions and their intensities. In addition, XRD can also provide indirectly the information about the internal stress and the dislocation density.

In this work, the crystallinity of each specimen was investigated by a Philps X´Pert MRD Pro diffractometer in θ-2θ geometry.

3.2.2 Electron backscattering diffraction

Applying a conventional optical microscopy, some crystallographic information of the sample can be determined, such as the grain size or different phases by the different contrasts or colors. However, the information about the orientation of each grain is lacking. As compared to the optical microscopy, the X-ray diffraction (XRD) can give the general information about the texture of the sample. But the distribution or the mapping of the grain orientation and grain size cannot be illustrated. Electron backscattering diffraction (EBSD) is evaluated by an auxiliary secondary detector mounted in the scanning electron microscope (SEM). It combines the advantages of the optical microscopy and X-ray diffraction. In this work the EBSD measurement was performed using a detector from Oxford Instruments, named 'HKL Channel 5'.
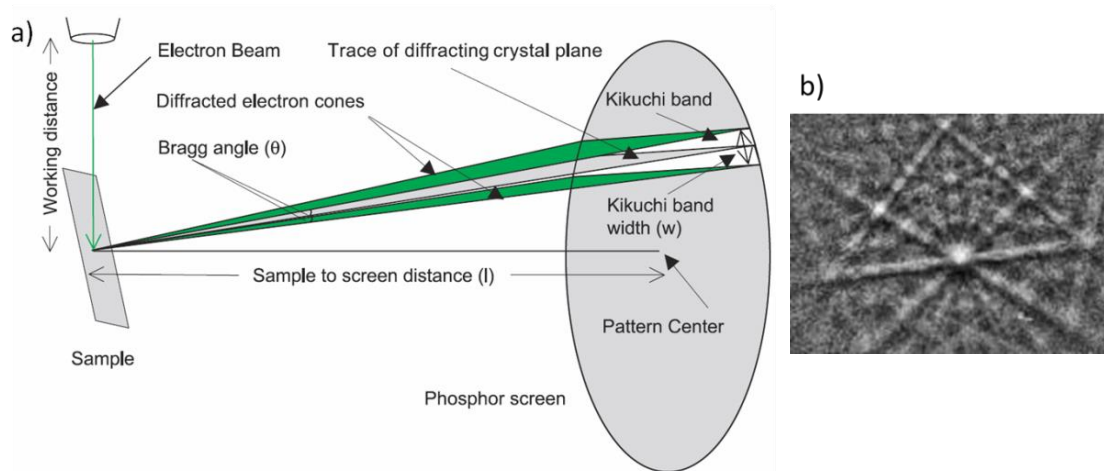
Fig. 3.1 **a) Functionality of the EBSD measurement** [58]; **b) Diffraction pattern from Si collected at 20 kV accelerating voltage**

Fig. 3.1a[58] illustrates the principle of the EBSD measurement. The primary electron beam is focused on the surface of a sample tilted at 70°. The electron beam scattered by the surface is then diffracted by the lattice planes based on the Bragg's law. Then on a phosphor screen, which stands in front of the CCD camera, the Kikuchi bands are detected (Fig. 3.1b). Using the Hough-transformation the lattice orientation at this point can be calculated. The measured region is scanned from a pixel to another. Consequently, a color-coded mapping from the in-

vestigated region can be achieved, which provides the graphical information about the grain size and orientation as well as the grain boundary character, even the local lattice strain.

To avoid the shadowing from the surface roughness, the specimens must be polished, to get a smooth surface. The samples were embedded with 'Crystalbond' mounting wax (Part No. 40-8150, Company Buehler) on an Al sample holder at first. Subsequently, they were grinded with sand paper (SiC paper, grit 600, Company Struers) and then polished with 1 μm diamond suspension through an automatic polisher (Tegra Pol-35, Company Struers). Every 15 minutes the samples were inspected under the optical microscope to control the polished depth. Finally, they were fine polished with 1/4 μm diamond suspension on a vibratory polisher (Vibromet 2, Company Buehler).

3.3 Chemical compositional characterization

3.3.1 Energy dispersive X-ray spectroscopy, Auger electron spectroscopy and X-ray photoelectron spectroscopy

The chemical composition can be determined usually by three methods, e.g. energy dispersive X-ray spectroscopy (EDX), Auger electron spectroscopy (AES) and X-ray photoelectron spectroscopy (XPS). In EDX and AES measurement the electron beam is operated as a primary excitation (Fig. 3.2a and b), while an X-ray beam is applied in XPS measurement (Fig. 3.2c). To investigate the chemical composition, the emissions of the different characteristic signals are collected with the corresponding detectors. The characteristic X-ray radiation is utilized for EDX measurement (Fig. 3.2a), while the kinetic energy of the Auger electrons is measured for the material characterization in AES (Fig. 3.2b). During the XPS measurement the photoelectron are detected and evaluated (Fig. 3.2c).
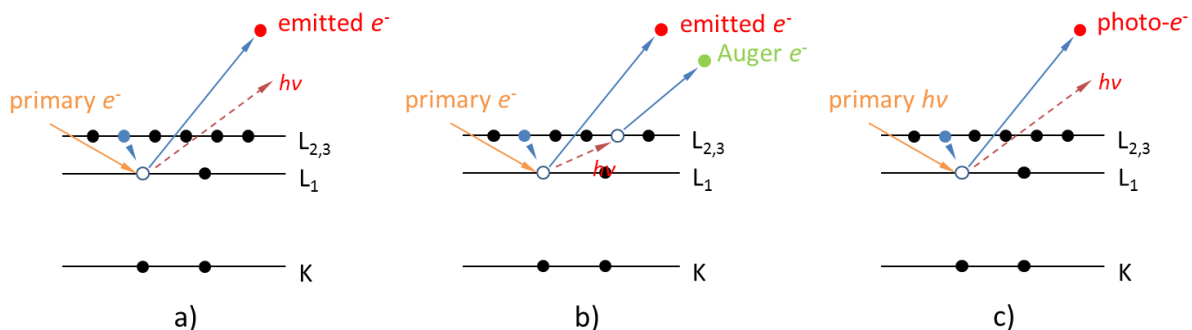
Fig. 3.2   **Functionality for characterization of the chemical composition: a) EDX; b) AES; c) XPS**

In this work, an EDX detector from 'Oxford instruments' was mounted in the SEM equipment, Carl Zeiss Leo 1530-VP. The measurement was operated at an accelerating voltage of

10 kV. The chemical composition of the surface and surface-near volume of the specimen was investigated by Auger-electron spectroscopy (AES) depth profiling, as well as the local analysis in a scanning Auger microscope (JEOL JAMP-7830F) equipped with a secondary electron microscope. A focused 10 keV electron probe of 20 nm spot size was used to determine the local composition at the regions of interest.

3.3.2 Electron energy loss spectroscopy

The chemical composition can be also analyzed through electron energy loss spectroscopy (EELS). The measurements in the core-loss range were operated in a Zeiss EM912 Omega microscope at 120 kV. The element mappings of the low-loss region were carried out at the sub-elecronvolt sub-angstrom microscope 'SESAM' (Company Carl Zeiss, Germany) using an accelerating voltage of 200 kV. The SESAM is equipped with field-emission gun, a symmetric electrostatic Omega-type electron monochromator and an in-column MANDOLINE energy filter. A series of energy-filtered images were recorded in the range from 14 to 30 eV using a slit of 0.45 eV. The acquisition time per frame was 10 s with a CCD binning of two. The specimen drift in the image series was corrected by using the script "statistically determined spatial drift correction" (SDSD correction).[59]

3.4 Electrochemical performance characterization

To test the electrochemical performance of the Si thin films as anode material for Li ion batteries, the samples were assembled into a Swagelok cell as working electrodes (Fig. 3.3). Pure Li foil delivered by 'Aldrich' was used as the counter electrode. On the electrodes the glass fiber (GF/D) from 'Whatman' was employed as the separator to the electrolyte. Between the electrodes, 1 M $LiPF_6$ in a non-aqueous mixture of ethylene carbonate (EC) and dimethyl carbonate (DMC) with a volume ratio of 1:1 (Ube Industries Ltd) was filled as electrolyte. The cells were assembled in an Ar-filled glove box. Subsequently, charge-discharge measurements were performed at room temperature under different rates from 0.1C to 8C (1C denotes the current density to theoretically achieve complete reaction to form $Li_{22}Si_5$ phase within 1 h) in a voltage range of 0.01-1.5 V on an Arbin MSTAT battery test system.
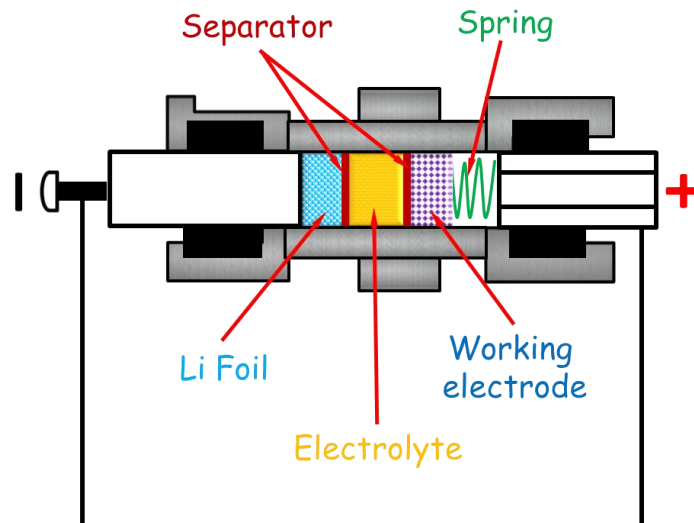
Fig. 3.3   Installation of the Swagelok cell

Chapter 4

Large-grained Si induced by Porous Al Layer

Large-grained Si layers with good crystallographic quality can be applied as the seed layers for further epitaxial thickening to be the thin film solar cells. Using a compact Al layer to induce the crystallization of an amorphous Si layer, the crystallized Si with an average grain size of 10 to 15 μm is achieved. However, it is still a challenge to get even larger Si grains. In this chapter, the crystallization behavior of an amorphous Si layer induced by a porous Al layer will be investigated, to explore the difference on the crystallographic results and the crystallization process to the compact Al layer.

4.1 Fabrication

- **Substrate Preparation**

Before the layer deposition, glass substrates (Hevasil 102) were rinsed with ethanol in an ultrasonic cleaner to remove the contaminations on the surface. Subsequently, the substrates were placed in a multi-target DC sputtering system with ultra-high vacuum. When the base vacuum pressure reached below $1 \cdot 10^{-7}$ mbar, the substrates were cleaned with Ar^+ ions for 1 minute.

- **Layer Deposition**

A 750 nm thick Al layer was deposited with an electrical power of 100 W under different bias voltages varied from -100 to -200 V. As a reference sample, an Al layer with the same thickness was coated on glass substrates. The electrical power was also 100 W without applying a bias voltage. After sputtering the Al layer, a 1000 nm thick Si layer was deposited with an electrical power of 100 W. The whole deposition progress was kept at room temperature. The structures of these as-deposited samples are sketched like Fig. 4.1a.

On the other glass substrates the Al layer was coated with the same electrical power and the bias voltages varied also from -100 to -200 V. After the deposition of the Al layer, they were annealed in the oven under 333 mbar (250 torr) Ar atmospheres at 400 °C for 5 hours to form a thin Al oxide layer. Afterwards a 1000 nm thick Si layer was deposited with 100 W in the same sputtering chamber. The layer sequence is sketched like Fig. 4.1b.
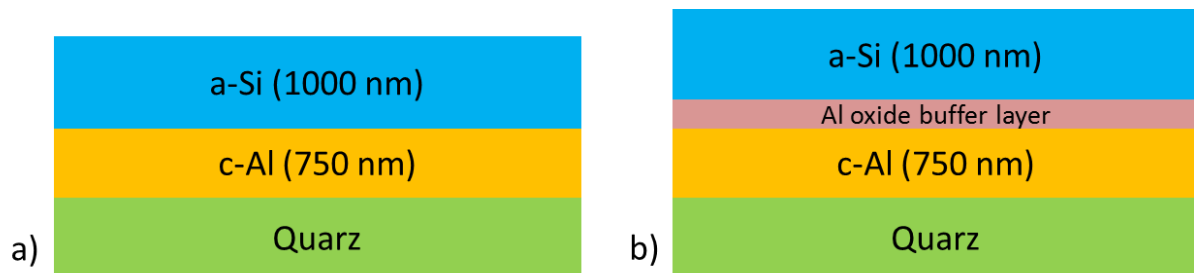
Fig. 4.1   Structure construction of Al-Si bilayer system

- **Post Treatment**

To find out the differences in the crystallization behavior of the amorphous Si, all samples were investigated after annealing in a vacuum oven at 400 °C for 15 hour. Then they were annealed further at the same temperature for longer time till a continuous c-Si layer was formed.

4.2 Results

4.2.1 Morphologies of Al layers

Compared to the compact Al thin film deposited with the normal conditions (Fig. 4.2a), a porous Al layer can be formed with a bias voltage (Fig. 4.2b). Applying a bias voltage, Al adatoms are accelerated and fly to the substrate with higher kinetic energy. When the adatoms reach the surface of the substrate, they need certain time to reach an equilibration position, to form a compact layer. However, the next adatoms arrive too "quickly" at the surface. They keep the earlier arrived adatoms from reaching the equilibration position. Therefore, atoms are "frozen" in the nonequilibration positions and a porous layer can be formed.
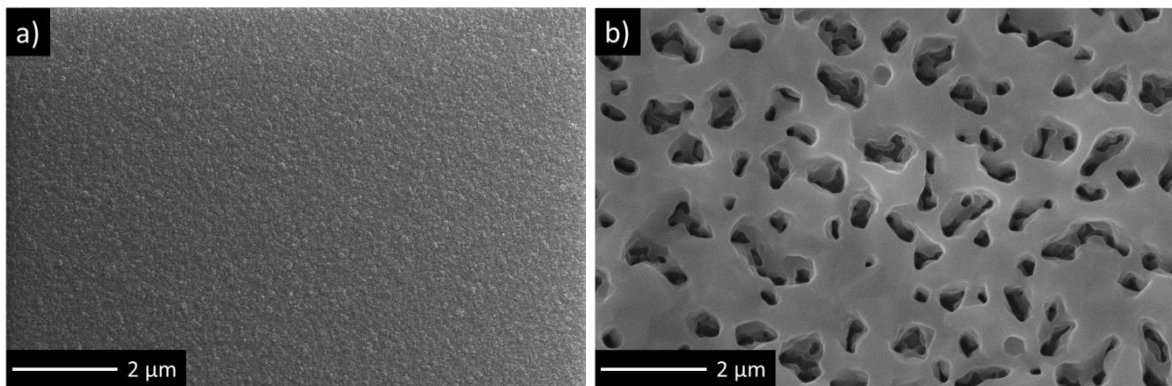
Fig. 4.2   Surface morphology of Al layer prepared with different sputtering parameter: a) a compact Al layer (without applying a bias voltage); b) a porous Al layer (with applying a bias voltage).

4.2.2 Grain growth of crystallized Si layer

Upon annealing at 400 °C for 15 hours, Al induces the crystallization of the amorphous Si. Using the optical microscope, the microstructure of the crystallized Si is studied. Due to the difference of the optical contrast between Al and Si, the crystallized Si can be distinguished from the Al matrix (Al: bright phase in Fig. 4.3; Si: dark phase in Fig. 4.3).

In the compact Al layer, amorphous Si crystallizes all over the Al grain boundaries and transits into small grains connecting to each other (Fig. 4.3a). In the porous Al layer (100 W with -100 V bias voltage), Si crystallized in dendrites with much lower nucleation density and larger grains (Fig. 4.3b). These crystallized large Si dendritic grains may consist of Si subgrains.
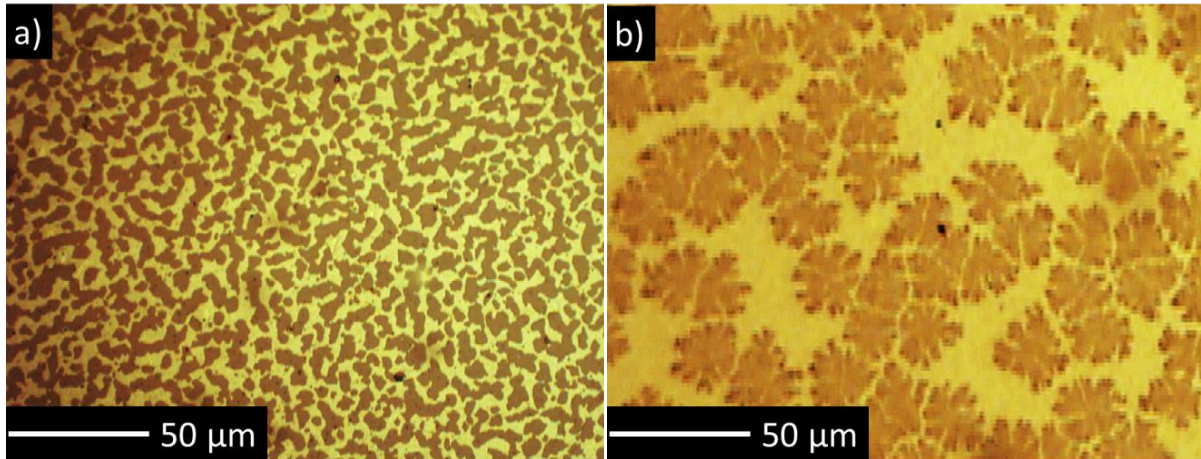
Fig. 4.3   **Optical microscopy image of crystallized Si grains after annealing at 400 °C for 15 hours: a) with compact Al layer; b) with porous Al layer.**

4.2.2.1 Crystallographic analysis of single Si grains

To analyze the crystallographic characters of a single large Si grain (such as grain orientation, type of grain boundaries), EBSD measurements were performed. According to the results of the color-coded orientation mapping (Fig. 4.4a), a large Si grain consists of subgrains with different orientations. Since the lattice distortion deteriorates the sharpness, width as well as the position of the Kikuchi-bands, the quality of the Kikuchi band indicates the distortion in the Si lattice. The worse band contrast reflects the lower quality of Kikuchi band and the higher distortion in the lattice due to the higher internal strain in the bulk of the subgrains (Fig. 4.4b). Therefore, the local distortion in each Si subgrain can be investigated qualitatively in this way. From characterizing the grain boundaries in a large Si grain (Fig. 4.4c), most of these Si grain boundaries are CSL Σ3 boundaries (red lines in Fig. 4.4c). Sometimes, as a consequence of the interaction between two CSL Σ3 boundaries, a CSL Σ9 boundary (purple lines in Fig. 4.4c), i.e. the second order of CSL Σ3 boundary, is developed from the meeting points of two CSL Σ3 boundaries. Combined with Fig. 4.4b the subgrains with higher band contrasts (darker subgrains) have neighbours with lower band contrasts (brighter subgrains). It indicates that the lattice distortion in the Si subgrains can be relaxed by the formation of the twins. Since Si possesses relatively low stacking fault energy, the twins are constructed to reduce the developed internal strain in the Si subgrains. CSL Σ3 has a much lower energy (30 mJ/m^2) than other CSL grain boundaries, for example Σ9 (664 J/m^2).[60] Therefore, the most formed subgrain boundaries in the Si large grains are Σ3 boundaries.
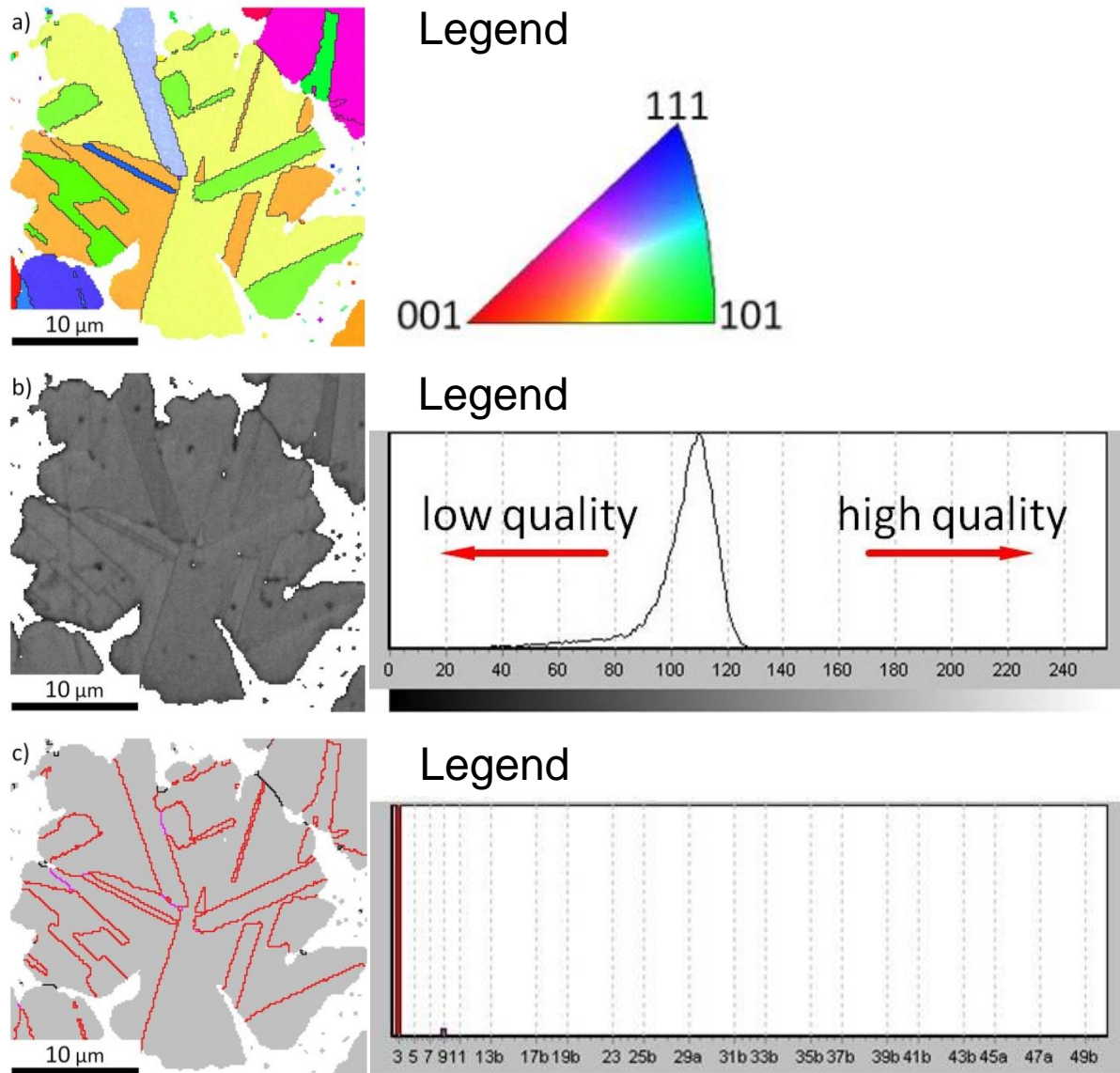
Fig. 4.4   **EBSD images of a crystallized Si grain upon porous Al layer: a) orientation mapping; b) band contrast (lowest quality in black, while highest quality in white); c) characterization of grain boundaries (black lines are normal low angle grain boundaries, red lines are CSL Σ3 boundaries and purple lines are CSL Σ9 boundaries).**

J. Chen, D. Cavalcoli et al. proved by electron-beam-induced current that the recombination activity between the conducting electrons and holes in these CSL boundaries is very weak.[25, 61] Therefore, the existing of these CSL grain boundaries is not responsible for reducing the efficiency of the thin film solar cells. The black lines in the mapping (Fig. 4.4c), the normal low-angle grain boundaries, are the recombination centers between the conducting electrons and holes. Therefore, the grain size of a Si grain could be defined as the grain area surrounded by the normal low-angle grain boundaries (the black lines). The CSL boundaries (colored lines) are not considered for the determination of the grain size.

4.2.2.2   Crystallographic analysis of continuous c-Si layers

After further annealing, a continuous crystalline Si layer is formed. After the polishing with the diamond suspensions, the exchanged Al in the upper layer could be removed. Using EBSD measurements performed on the continuous c-Si layers in several different regions of each sample, the crystallographic information about the grain size distribution and orientation mapping can be obtained by the color-coded mappings.

The Si layer crystallized by a compact Al layer and without an Al oxide buffer layer possesses the narrowest grain size distribution and the smallest average grain size, $\bar{d} = 1.1$ μm (Fig. 4.5a). *H. Kim* et al. proved experimentally, with the aid of an alumina buffer layer, the average grain size of crystallized Si increased.[32] Indeed, a compact Al layer with an Al oxide buffer layer induces the crystallization of the Si layer with a wider grain size distribution and a larger average grain size of 4.4 μm (Fig. 4.5b). Compared to the above-mentioned cases, a porous Al layer has a greater influence on the formation of large-grained Si layer than the Al oxide buffer layer. In this case, the average Si grain size reaches to 12.4 μm and the grain size distribution of crystallized Si becomes much wider (Fig. 4.5c). Some Si grains exceed 35 μm. Therefore, under both promoting influences (i.e. using a porous Al layer and an Al oxide buffer layer), very large Si grains could be consequently formed. The average grain size of this crystallized Si layer reaches 23.5 μm. The maximal Si grains are over 90 μm (Fig. 4.5d). In additions, from Fig. 4.5d it is obvious that there are much fewer twin boundaries in (100) grains (grains in red) than in the grains with other orientations (grains in other colors), because the (100) planes are less densely packed planes.
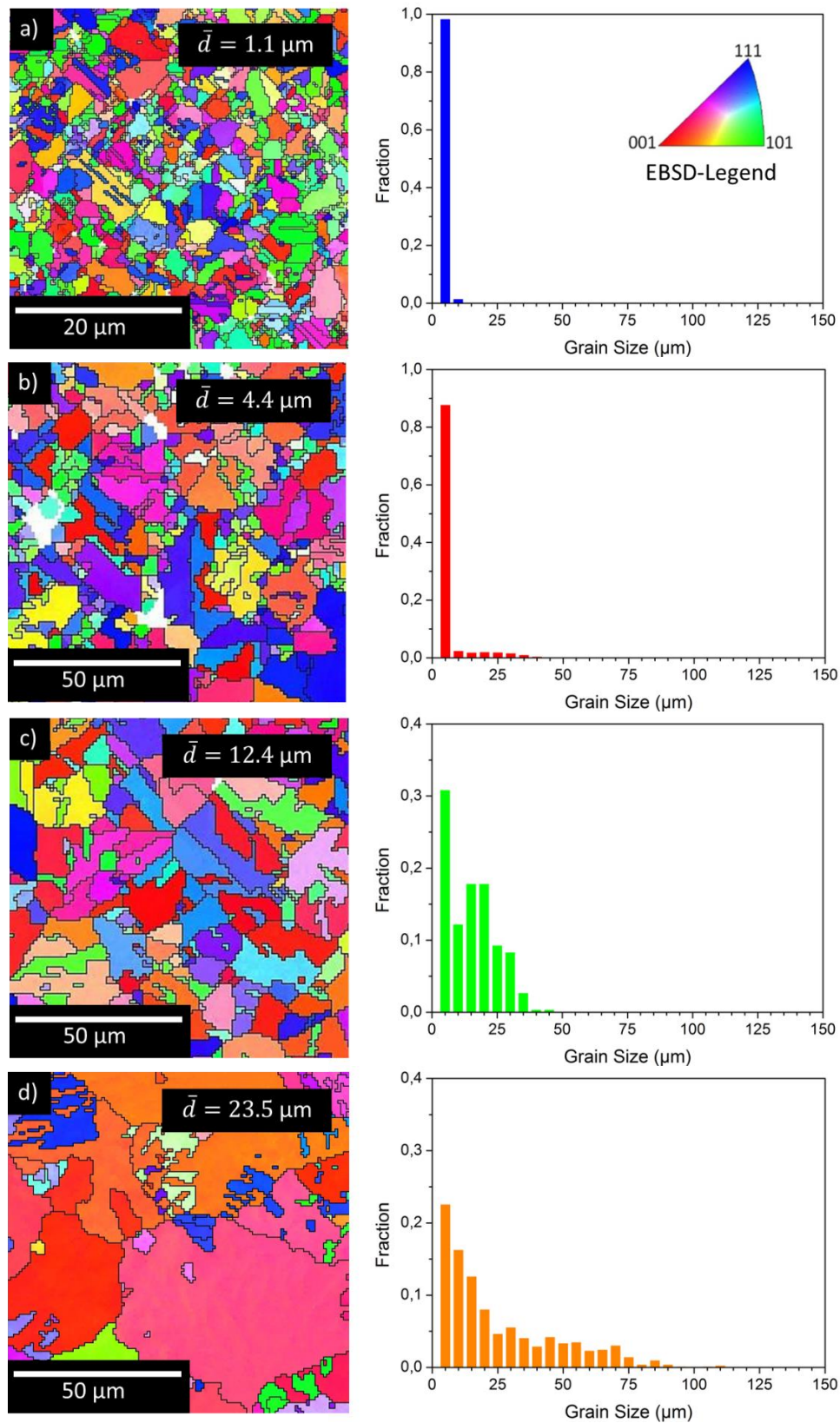
Fig. 4.5   **EBSD mapping and grain size distribution of the crystallized Si layer: a) without bias voltage and alumina buffer layer (blue); b) without bias voltage but with alumina buffer layer (red); c) with bias voltage but without alumina buffer layer (green); d) with bias voltage and alumina buffer layer (orange).**

4.3 Discussion

4.3.1 Crystallization of Si induced by a porous Al layer

In the compact Al layer, every Al grain boundary is ready to be wetted by the 'free' Si atoms. As soon as the a-Si wetting layer exceeds the critical thickness, Si nucleates in the Al grain boundaries (Fig. 4.6a).[50] As a consequence, due to the high nucleation density, Si can hardly crystallize into large grains.
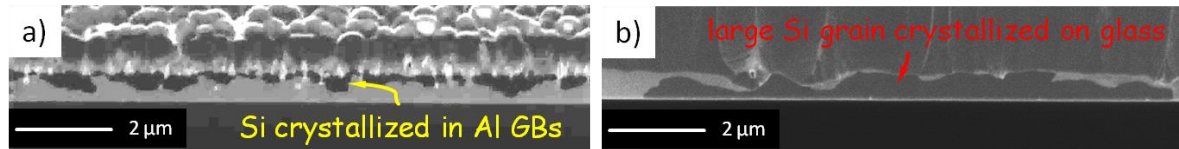
Fig. 4.6   **Cross-section of annealed samples with different Al layers: a) in the compact Al layer Si crystallized generally all over the Al grain boundaries (annealed at 400 °C for 1 hour); b) in porous Al layer Si diffused along the inner surface of the pores in Al layer and then crystallized heterogeneous on the surface of substrate (annealed at 400 °C for 15 h).**

In contrast, the crystallized Si grains induced by a porous Al layer are much larger (Fig. 4.6b comparing with Fig. 4.6a). In the porous Al layer, Al grain boundaries can be partially contaminated by O. These contaminated Al grain boundaries are not likely the active nucleation site for amorphous Si. Furthermore, the porous structure of Al possesses overall lower density of Al grain boundaries. It leads to lower nucleation probability of c-Si in the Al grain boundaries and thereby the formation of large Si grains. Unlike the crystallization of Si induced by the compact Al layer, Si deposited on the porous Al layer crystallizes heterogeneously on the glass substrate (comparing Fig. 4.6a and b)

Fig. 4.7 describes schematically the above-discussed crystallization mechanism of Si. Due to the high deposition rate many defects can be formed within the bulk Al grains, e.g. vacancies, dislocations. At the certain high annealing temperature (e.g. 400 °C) the intragranular diffusion, which involves the pipe and lattice diffusion, should occur (violet arrow Fig. 4.7). On the other hand, the inner surface of pores in Al layer offers another convenient diffusion path for the Si atoms (red line in Fig. 4.7). Therefore, a collective diffusion process can take place. During the annealing the free Si atoms can move through the Al grains by the intragranular diffusion. Once they reach the pores in Al grains, they would diffuse along the inner side in the Al pores till the surface of the substrate. As soon as the critical thickness of crystallization is reached, Si nucleated heterogeneously on the surface of the substrate and grew laterally further (Fig. 4.7). From these two reasons the large crystalline Si grains can be developed by a porous Al layer. However, due to lower nucleation density, lower effective diffusivity and

longer diffusion path, the formation of a continuous crystalline Si layer needs more time comparing to the crystallization induced by a compact Al layer.
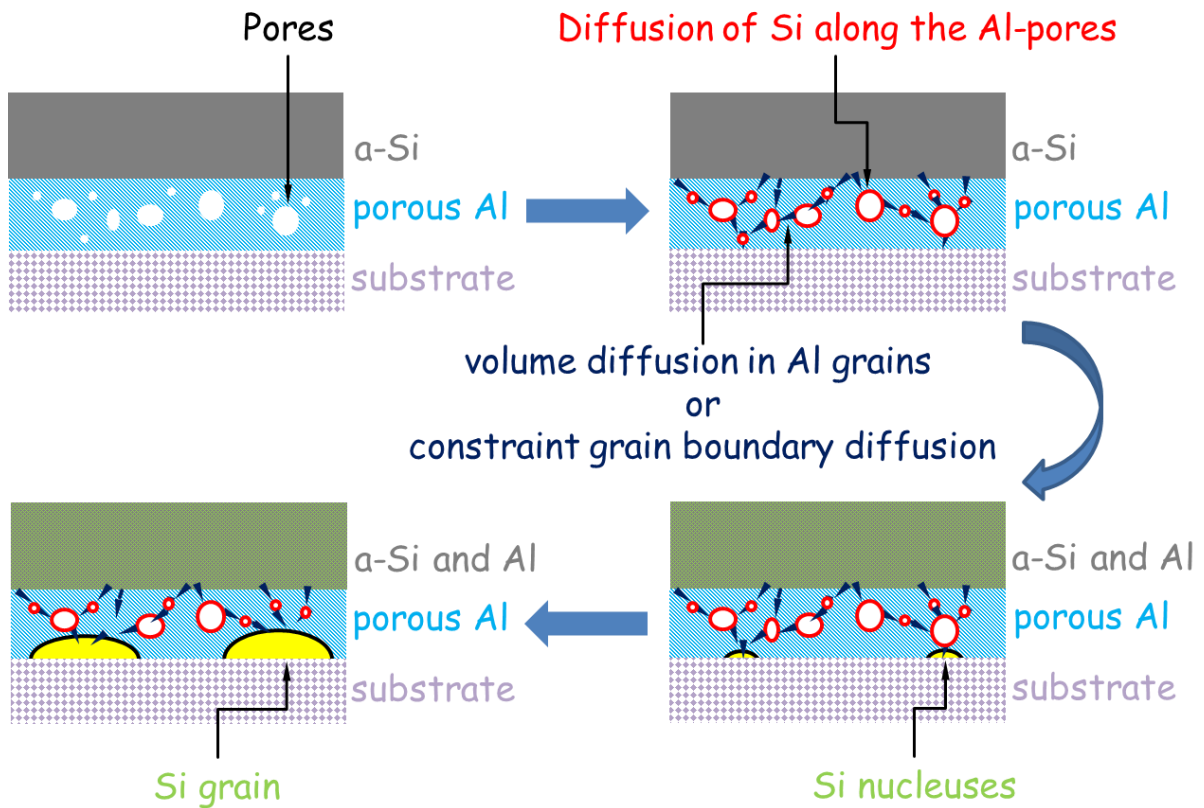
Fig. 4.7 Crystallization process of amorphous Si in porous Al layer

4.3.2 Texture evolution of Si in dependence on the grain size

With the aid of the EBSD color-coded mapping (Fig. 4.5), the grain orientation distribution in dependence on the average grain size can be investigated.(Fig. 4.8) Fig. 4.8 shows that the fraction of the (111) orientated Si grains decreases with increasing Si grain size, while the fraction of (100) Si grains increases.

Generally, the texture development in thin films is controlled by the minimization of its total energy which consists of elastic strain, interface and grain boundary energy.[62] Therefore, the total energy in the case of the Al induced crystallized Si layer can be described:

$$\Delta G = \Delta G_{\varepsilon} + \Delta G_i + +\Delta G_{\text{GB}} \qquad \text{Eq. 13}$$

ΔG_{ε}, ΔG_i and ΔG_{GB} stand for the elastic strain energy developed in crystallized Si layer, the difference in the interface energy between a-Si and Si grains to the glass substrate and total grain boundary energy.
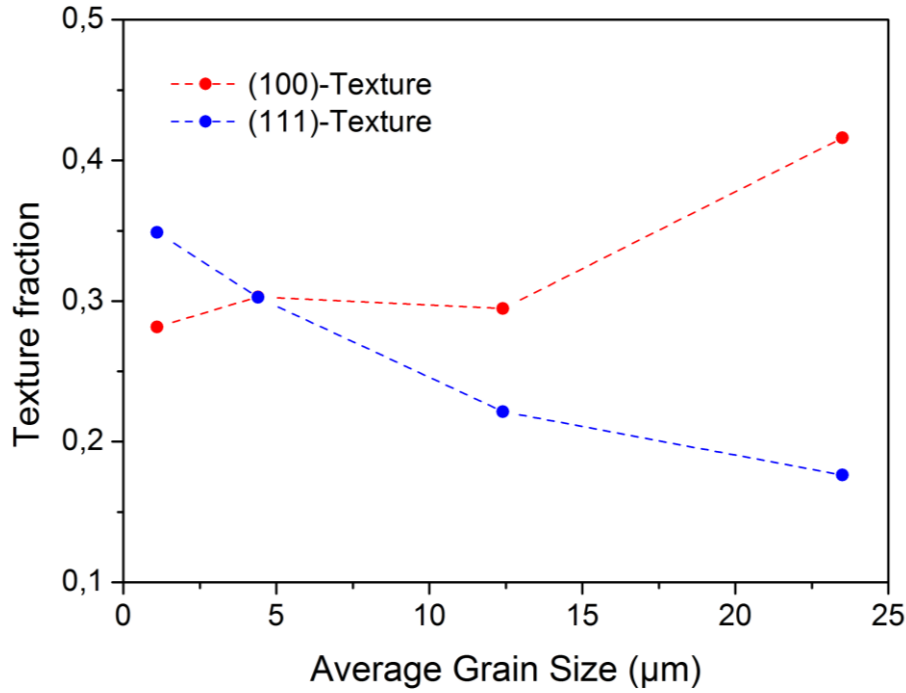
Fig. 4.8   Texture frequency in dependence on the grain size of the crystalline Si

As a consequence of the asymmetric diffusion between Si atoms in Al layer and Al atoms in Si layer, an internal stress would be developed during annealing.[54] With the further continuous growth of the crystalline Si, the internal stress i.e. the elastic strain energy ΔW_ε, increased. Analog to the model from *J. M. Zhang* and *P. Sonnweber-Ribic*,[62, 63] the elastic strain energy developed in crystallized Si layer ΔG_ε can be described by:

$$\Delta G_\varepsilon = \sum x_i \cdot \left(M_{(hkl)} - M_{a-Si} \right) \cdot \varepsilon^2 \qquad \text{Eq. 14}$$

x_i stands for the fraction of the grains in every orientation. ε means the elastic lattice strain in the Si grain with (hkl) orientation. $M_{(hkl)}$, $M_{a\text{-}Si}$ express respectively the elastic modulus in (hkl) Si grains and amorphous Si.

Based on the suggestion from *P. Sonnweber-Ribic*,[62] the change of the total interface energy ΔG_i during the crystallization of Si layer with a constant thickness h can be calculated by:

$$\Delta G_i = \sum x_i \cdot \frac{\left(\gamma_{i(hkl)} - \gamma_{ia-Si} \right)}{h} \qquad \text{Eq. 15}$$

$\Delta \gamma_{i_{(hkl)}}$ and γ_{ia-Si} stand for the interface energies of the Si grains with (hkl) orientation and amorphous Si to the glass substrate. h means in this case the thickness of the Si layer.

The grain boundary energy in the whole c-Si layer can be expressed by:

$$\Delta G_{GB} = \frac{1}{\bar{r}} \cdot \sum x_{GB_i} \cdot \Delta \gamma_{GB_i} \qquad \text{Eq. 16}$$

$\bar{r}$ notes the average grain size in the crystalline Si layer. $x_{\mathrm{GB_i}}$ and $\Delta\gamma_{\mathrm{GB_i}}$ stand for the fractions of the different grain boundaries and the corresponding grain boundary energy, respectively. According to four above-mentioned factors, the change of the favored texture in Fig. 4.8 can be explained by the following. (111)-orientated Si grains have lower interface energy to the substrate but higher strain energy as compared to the (100)-orientated Si grains. To minimize the total energy of the whole system, the texture with the favorite orientation develops in dependence on whether ΔG_ε or ΔG_i dominates. With a small average grain size of Si, the total system energy can be reduced by more (111) Si texture because the (111) interface energy dominates. With the increasing grain size of Si, the strain energy and grain boundary energy become dominant. The total system energy can be reduced through the development of (100) Si texture Fig. 4.8 indicates that there exists a transition from (111)-texture to (100)-texture of the formed c-Si layer upon a critical average grain size of Si.

4.4 Conclusion

The porous Al layer has a positive influence on the formation of a large-grained Si layer. The grain boundary diffusion of Si in the Al layer can be retarded due to the contaminations in the Al grain boundaries. At relatively high temperatures, a collective diffusion process could be activated in this case. Besides the retarded grain boundary diffusion of Si in the porous Al layer, the free Si atoms can also diffuse through the bulk Al grains via the defects in the Al grains, e.g. dislocations, vacancies. Moreover, the Si atom also diffused along the inner surface of the pores in Al layer. This whole collective diffusion process leads to a lower nucleation density and slower crystallization velocity. This influence can be even enhanced with an Al oxide buffer layer.

To reduce the developed internal stress during the crystallization, many CSL Σ3 twin grain boundaries are formed in the large Si grains except in the grains with (100) orientation. Due to the low recombination activity in these twin grain boundaries, the grain size of Si can be defined by the surrounded normal grain boundaries. With the increasing of the grain size the distortion energy will be dominant. Above a critical grain size the Si grain prefers to develop the (100) texture.

Chapter 5

Porous Si Layer by Al-induced Crystallization

Si is one of the most attractive candidates as anode material for the high capacity Li ion batteries. Due to the huge volume expansion during the lithiation, a porous structure of the Si layer is required to increase the durability. The porous structure of the Si layers is achieved by interrupting the post treatment of the Al-induced crystallization process of the nanocrzstalline Al/amorphous Si bilayers. The crystallized porous Si layers are investigated with different methods, such as TEM, SEM, FIB AES, XPS etc. To test their electrochemical performances, they are mounted in a Swagelok-cell as working electrodes. The thermodynamic and kinetic fundamentals of the formation of these porous Si layer are discussed in the following sections.

5.1 Fabrication

- **Substrate Preparation**

Pure Ti foils (99.6%, Goodfellow) or pure Ni plates were used as substrates for the deposition of Si/Al bilayers. The substrates were cleaned with ethanol in ultrasonic bath to remove organic contaminants from the surface before film deposition.

- **Layer Deposition**

After reaching a background vacuum pressure less than 1×10^{-7} mbar, the substrates were cleaned with Ar^+ ions for 1 min. The Si/Al bilayers were deposited by sequentially sputtering Si target and Al target in a high-vacuum multi-target DC sputtering system. At first, a 1500 nm thick Si layer was deposited by using a sputtering power of 100 W in an Ar atmosphere of 5.9×10^{-3} mbar, followed by depositing a Al layer in different thickness (from 150 nm to 1500 nm) with 200 W under the same Ar pressure. The deposition processes were accomplished under room temperature. The Al/Si bilayers were constructed as shown in Fig. 5.1
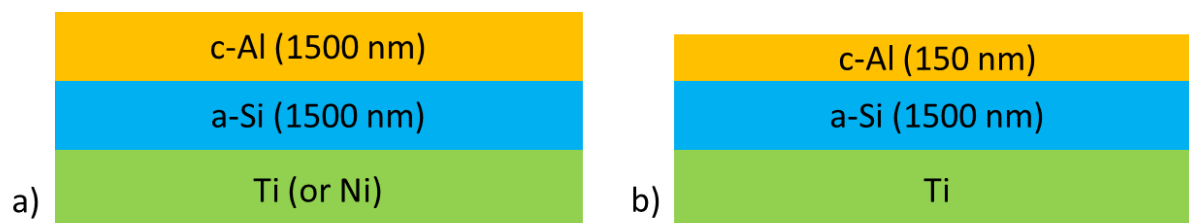
Fig. 5.1   Structure construction of Al/Si bilayer system for Li ion battery

- **Post Treatment**

The deposited Si/Al samples were then annealed in a vacuum oven at different temperatures (varied from 180 °C to 600 °C) for different time (varied from 5 minutes to 80 hours) to find out the optimal annealing conditions to build the suitable morphologies of the Si layer as anode materials.

- **Chemical Etching**

The annealed samples were further etched by 1 mol/L NaOH solution to remove Al, which served as sacrificial template. Finally, they were flushed with distilled water and dried with Ar.

5.2 Results

5.2.1 Crystallization of a-Si at different temperatures

It is known that the different diffusion processes can be activated at different temperatures. To investigate the influences of the annealing temperature on the morphology of the porous Si layer, the samples were annealed at different temperatures and characterized with different methods.

5.2.1.1 Crystallization of a-Si below the eutectic point

- **Crystallization of a-Si in Al triple junctions**

An a-Si/c-Al bilayer sample (the deposited layer sequence is sketched in Fig. 5.1a) was annealed at 200 °C (i.e. much lower than the eutectic point of Al-Si system 577 °C) for 60 hours. Fig. 5.2 is a secondary electon image of the structure and the yellow circles mark out the Si diffused from the layer underneath. Therefore, it can deduce that the Si diffuse along the triple junctions of Al grains rather than along the planar Al grain boundaries at this temperature.
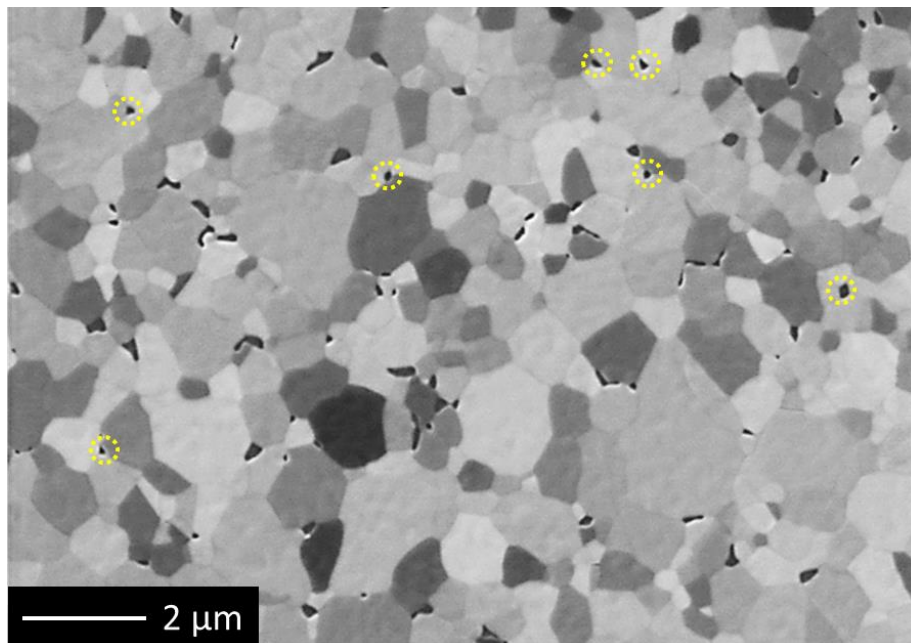
Fig. 5.2   **Al/Si bilayers that were annealed at 200 °C for 10 hours crystallized in the triple junction of Al grains at first (the yellow circles are c-Si)**

Fig. 5.3 shows the cross-section of an a-Si/c-Al bilayer sample. From the different material contrasts, Al and Si can be easily distinguished from each other. In Fig. 5.3a (bright phase: Al; dark phase: Si), it could be observed that Si diffused upwards into the Al layer, while Al moved downwards into the original a-Si layer. The Si atoms prefer to diffuse vertically and

the diffusion trails are thin and long in the direction of z-axis. After etching of Al, porous Si frameworks are developed in the upper layer, while many nano-sized pores are formed in the lower layer.
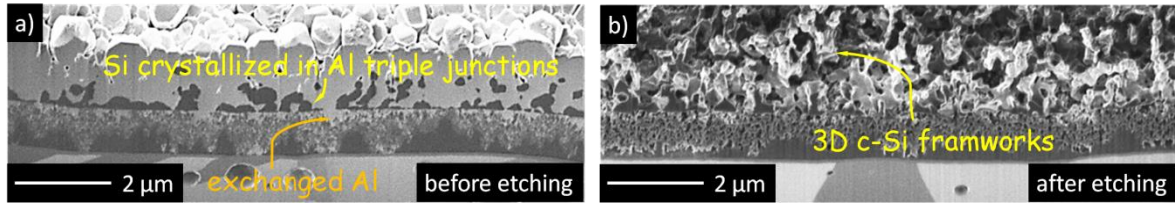
Fig. 5.3   **Cross-section of Al induced crystalline Si at 200 °C for 60 h: a) before etching (bright phase: Al; dark phase Si); b) after etching.[64]**

After the selective etching of the Al component, the surface morphology of the crystallized Si layer can be inspected by scanning electron microscopy (SEM) (Fig. 5.4). The nano-sized thin frameworks consisted of c-Si are developed on the surface (Fig. 5.4).
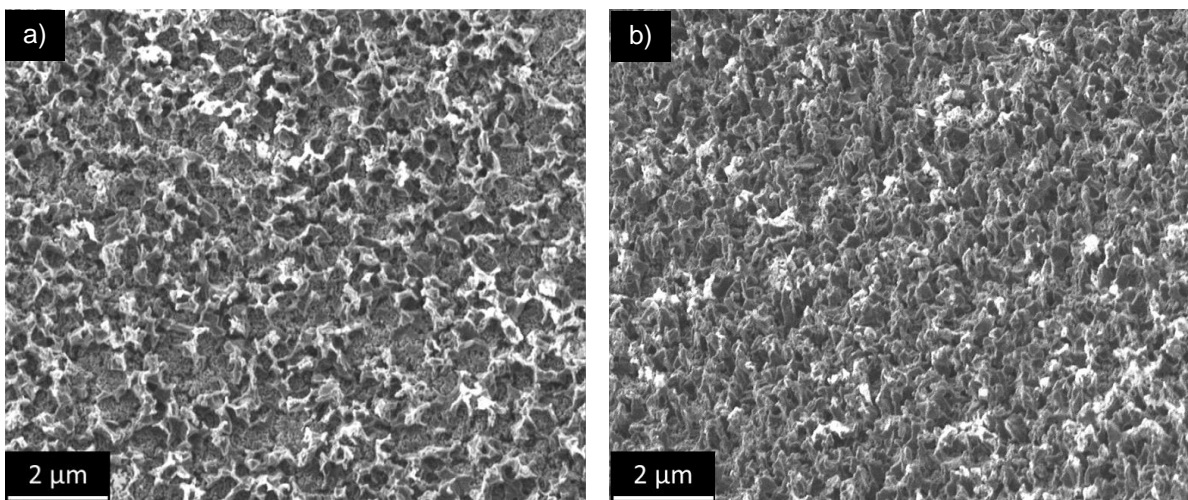
Fig. 5.4   **Overview surface SEM images of porous Si films annealed at 200 °C for 60 hours (a) and the corresponding overview SEM images with 45 tilt (b)**

- **Crystallization of a-Si in Al grain boundaries**

An a-Si/c-Al bilayer fabricated structurally like Fig. 5.1a was annealed in a vacuum oven at 450 °C (i.e. slightly under the eutectic point of Al-Si system of 577 °C) for 30 min. Al component was etched with alkali solution.

Fig. 5.5 shows the corresponding microstructures by focused ion beam microscopy (FIB) and scanning electron microscopy (SEM). The initial a-Si/c-Al bilayer with Al on top was deposited on a polished Ti foil substrate at room temperature. The distinct interface between the Si and Al sublayers is seen by the contrast of the FIB image (Fig. 5.5a). The structural state of the samples after annealing is depicted in Fig. 5.5b. Si diffused upwards into the Al layer,

likely along the Al grain boundaries. Al penetrated into the area of the initial a-Si. At a certain stage, a discontinuous c-Si layer formed above the original a-Si sublayer (called the primary crystallized Si, PC-Si) as shown in Fig. 5.5c. After an alkali solution removed practically the entire Al, this layer was only loosely connected to the substrate-attached Si by statistically distributed 'bridges'. This remaining frail Si layer was easily removed by washing with distilled water, probably aided by the development of a compressive stress field as outlined below. A final nano-columnar architecture was left attaching to the substrate as shown in Fig. 5.5d, e and f.
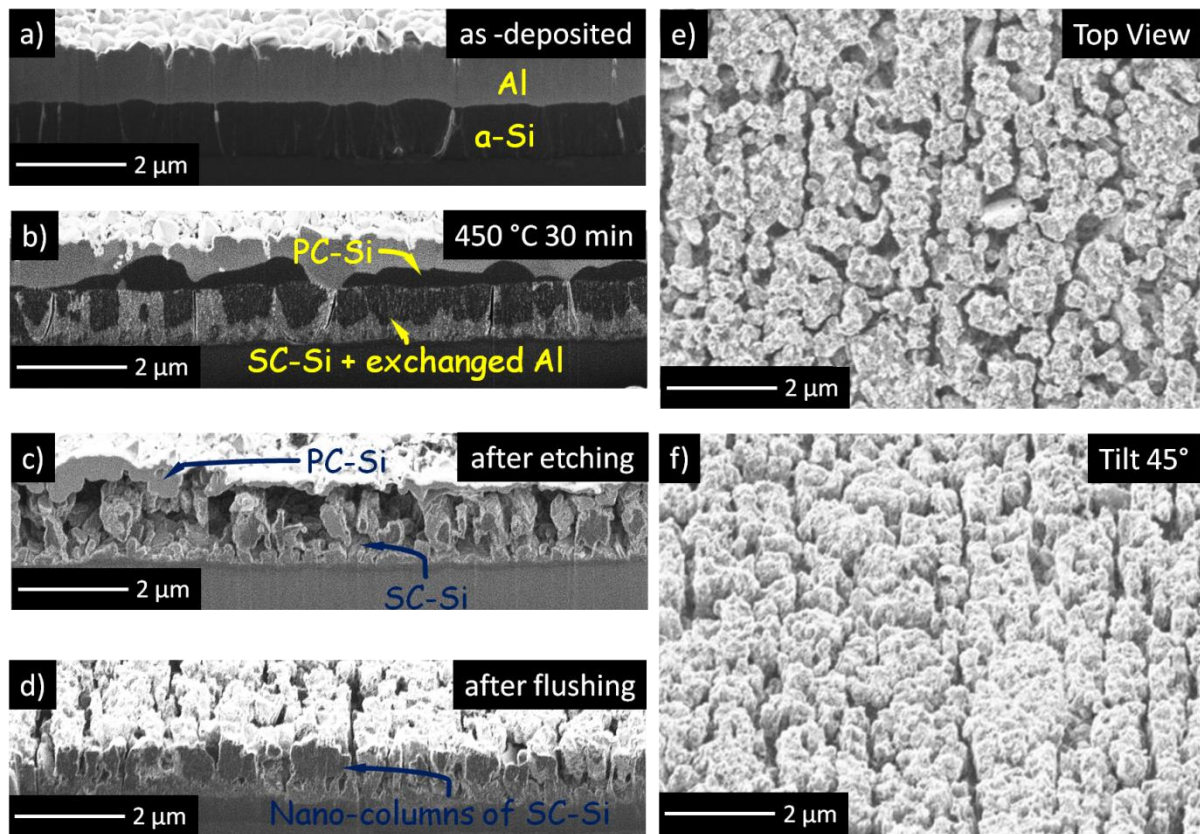
Fig. 5.5   **Cross-sectional FIB images: a) before annealing, Al layer (bright) was deposited on Si layer (dark); b) after annealing at 450 °C for 30 min; c) after etching with NaOH solution; d) final columnar structure of SC-Si; e) shows the overview surface SEM images of Al$_2$O$_3$-coated SC-Si nano-columns annealed at 450 °C for 30 minutes and the corresponding overview SEM images with 45 tilt f).[64, 65]**

An amorphous Si layer was fabricated as reference sample, which is evidenced by the corresponding X-ray diffraction (XRD) analysis (green curve in Fig. 5.6). After the annealing of a-Si/c-Al bilayer sample under vacuum, the Si (111), (220) and (311) peaks were detected (red curve in Fig. 5.6), which confirmed the crystallization of a-Si. As indicated by the disappearance of Al peaks (blue curve in Fig. 5.6) the Al layer was etched with the alkali solution. The

loose PC-Si layer was flushed away during the cleaning with distilled water, which is reflected by the weakened Si peaks.
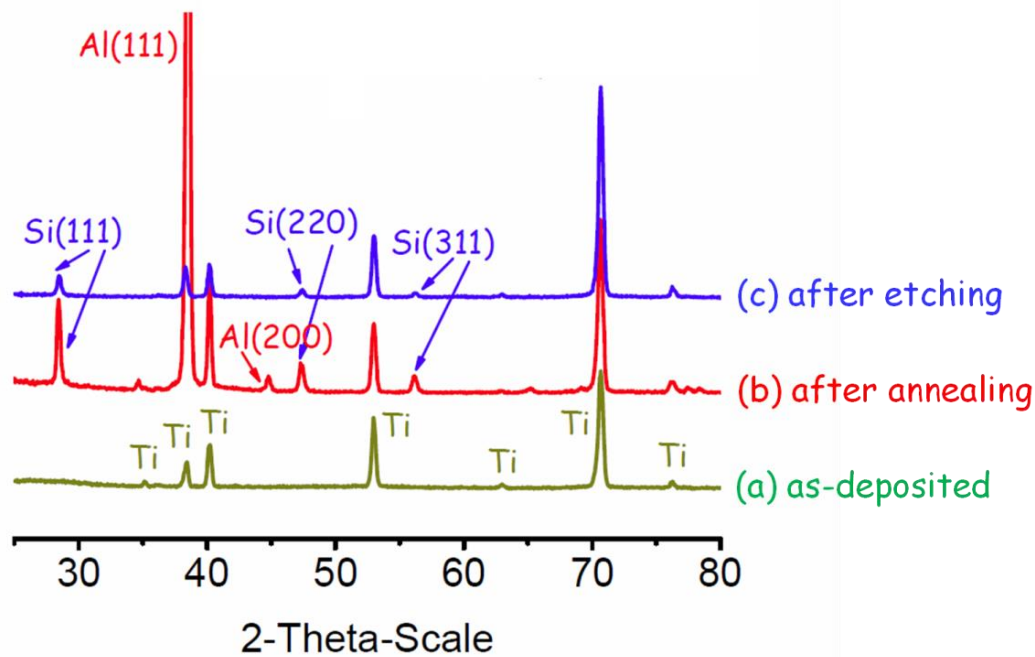
Fig. 5.6   XRD patterns of the sample at the different stage: a) as-deposited Si film (green); b) Al/Si bilayer after annealing at 450°C for 30 min (red); c) nano-columnar SC-Si thick film after annealing and Al etching (blue) on Ti substrates. The diffraction peaks of Ti substrate, Al template, Si active material are labelled.[64, 65]

The processing steps to fabricate Si films with a nano-columnar microstructure are summarized in Fig. 5.7. An a-Si/c-Al bilayer is deposited on a conductive substrate, which doesn't react with Li ion electrolyte, likewise Ti, Cu, Ni, TiN. According to the interpretation from *Z. M. Wang*, the formation of this corrugated c-Si layer is the result from the intermixing between Si and Al and Al induced crystallization of Si.[50, 54] The diffusion of Si in Al grain boundary plays a very important role. However, at this intermediate annealing temperature (450 °C), some other diffusion processes could also be activated, e.g. volume diffusion. Which diffusion process is dominant, will be discussed in the following section. During annealing, the 'free' Si atoms diffuse practically into the Al grain boundaries to reduce the grain boundary energy of Al. Exceeding a critical thickness, Si crystallizes in the Al grain boundaries. Simultaneously, the Al atoms squeeze downwards into the original a-Si sublayer. With further annealing, the intermixing proceeds until Si- and Al-layers are progressively exchanged. At a certain stage, a discontinuous c-Si is formed above the original a-Si sublayer. This crystalline Si layer is named primary crystallized Si (PC-Si). Due to the intermixed Al, the lower a-Si layer also begins to crystallize. The crystallized Si in the lower original a-Si sublayer is called secondary crystallized Si (SC-Si). The intermixing between Al and Si layer

evolutes the compressive stress in upper original c-Al sublayer and the tensile stress in lower original a-Si sublayer.[54] As a consequence of the build-up of this large stress gradient at the interface between upper and lower layer, the PC-Si layer is loosely connected to the SC-Si after the etching of the Al. The remaining frail PC-Si layer could be easily removed by washing with distilled water. Finally, the nano-columnar architecture is developed.
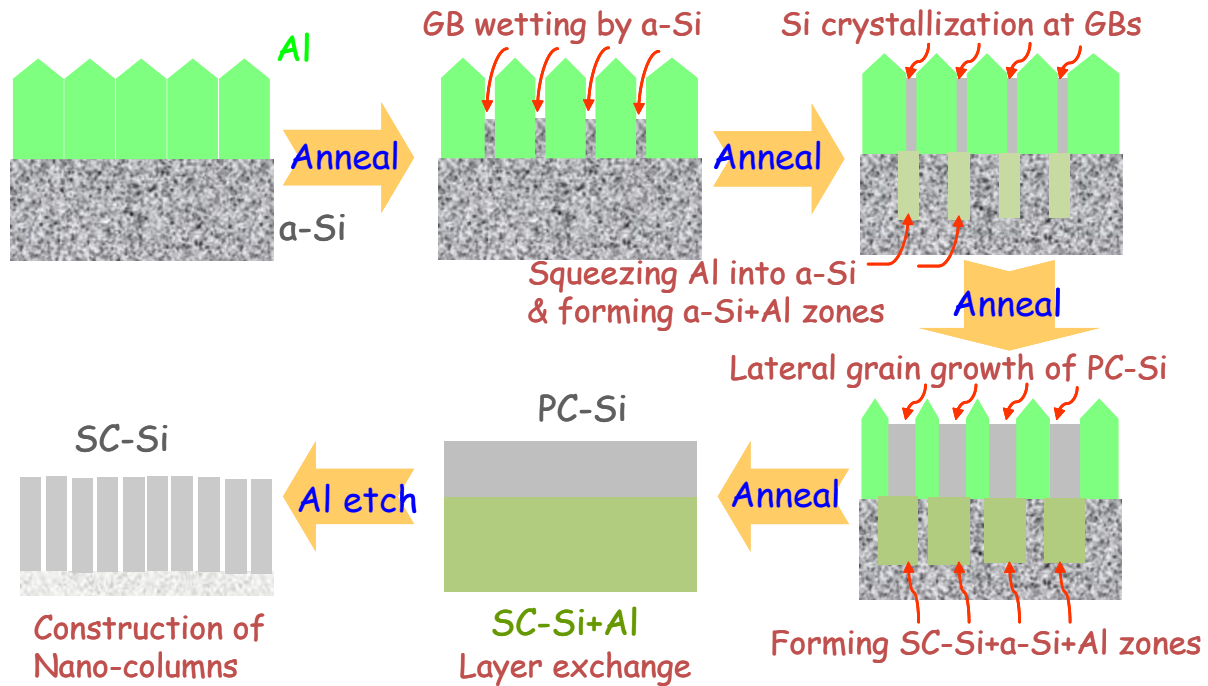
Fig. 5.7 **Annealing/etching steps to construct nano-columnar Si thick films from Al/Si bilayers. It includes (1) Al grain boundary wetting and splitting by a-Si, (2) crystallization of a-Si and crystalline Si growth at Al grain boundaries, (3) transport of Al downwards into original a-Si, leading to secondary crystallization of Si therein, (4) Al-induced layer exchange, (5) etching off Al and leaving behind nanostructured Si thick films.[65]**

5.2.1.2 Crystallization of a-Si above the eutectic point

The Si porous framework is in this work prepared as thick film by starting with the deposition in a high-vacuum multi-target direct-current (DC) sputtering system of an Al/Si bilayer with asymmetric sublayer thicknesses (i.e.1500 nm for Si and 150 nm for Al, sketched like Fig. 5.1b). A polished Ti foil substrate kept at room temperature serves as substrate. A cross-sectional focused-ion-beam (FIB) image of as-deposited film specimen is shown in Fig. 5.8a. The specimens with a-Si/c-Al bilayers were annealed in a vacuum oven at 600 °C (i.e. slightly above the eutectic point of Al-Si system of 577 °C) for 30 min, followed by fast cooling to room temperature within 2 minutes. Compared to the as-deposited specimen (Fig. 5.8a), a nearly continuous Si film (dark phase in Fig. 5.8b) with a thickness of about 150 nm has formed at the original location of Al overlayer (bright phase in Fig. 5.8a) which is similar to

the samples annealed below eutectic temperature. The observed exchange of Al and Si sublayer sequence upon annealing at 600 °C is associated with the Al-induced crystallization of a-Si[66] at temperatures that are lower than the bulk crystallization temperature of a-Si (about 700 °C[67]). The Al-induced crystallization of a-Si has been reported in literature to occur at temperatures both below [68] and above [13] the eutectic point (577 °C) of Al-Si. The layer exchange of Al and Si layers is a result of the continuous growth of Si crystallites exclusively in the Al layer during the crystallization.[50] The exchanged Al exists mainly in a large amount of small droplet-like precipitates (bright spots) within the original Si sublayer (see the cross-sectional FIB image of Fig. 5.8 b). At last step, the annealed specimen was rinsed in NaOH solution (to selectively etch off the Al), flushed with distilled water and finally dried with Ar. As a result of the described procedures, a nano-porous Si framework structure has been generated, as clearly shown in Fig. 5.8c and e. The Si frameworks are highly porous, containing a very high density of nano-porous.
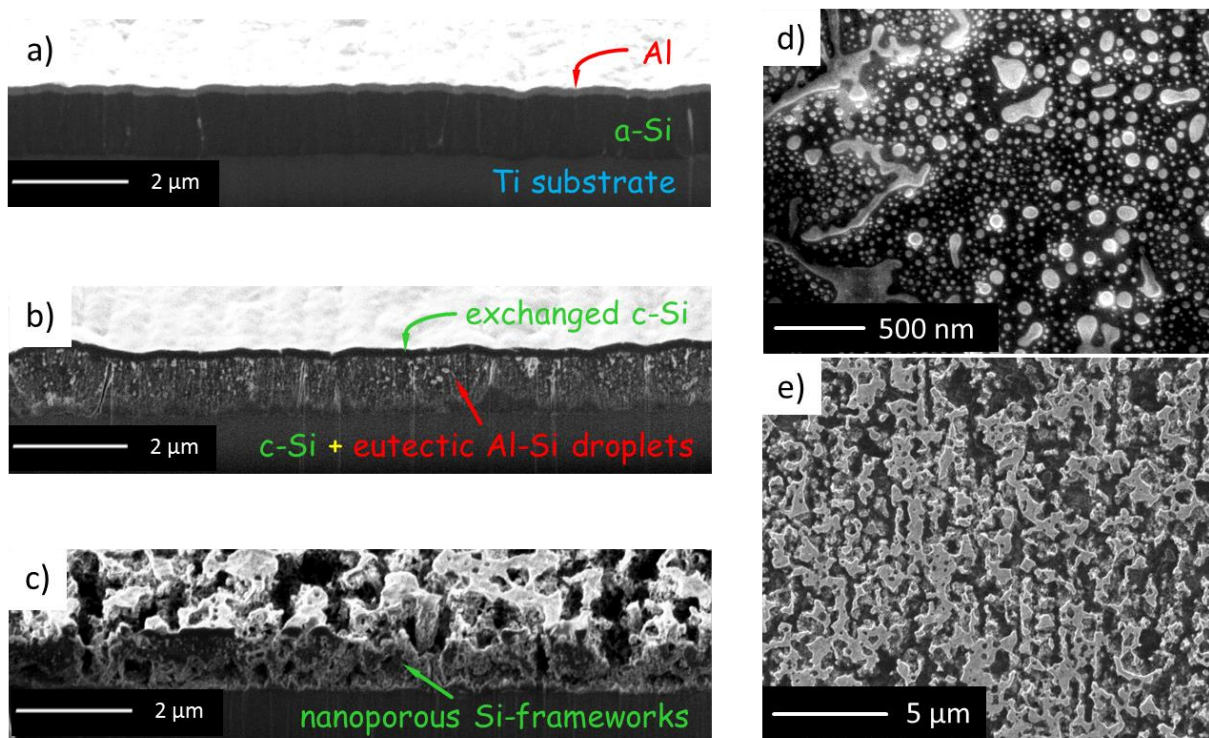
Fig. 5.8 **Overview and cross-section images of nanoporous c-Si frameworks annealed at 600 °C for 30 min: a)-c) cross-sectional FIB images of microstructure evolution in the sample with a ratio between Si and Al 10:1 in different fabrication stages: a) before annealing; b) after annealing but without etching (upper layer: continuous exchanged c-Si; lower layer: bright phase: Al-droplets; dark phase: eutectic c-Si); c) after etching, (nano-porous c-Si frameworks); d) top view which was sputtered with FIB to polish the upper exchanged Si layer away (bright phase: Al nano droplets, dark phase: c-Si matrix); e) top view of the nanoporous c-Si frameworks.[64, 69]**

Detailed investigations of the annealed Al/Si specimens have been carried out in order to find out the formation mechanism of the nano-porous Si frameworks. Fig. 5.8d shows a high-magnification SEM image of the annealed specimen. The exchanged c-Si overlayer was removed by ion sputtering. The Al-rich precipitates (investigated in the latter section) located in the Si bottom film and distributed homogenously (bright phase in Fig. 5.8d). These nano-sized Al-rich precipitates are mostly spherical with diameters of only about 10 nm to 100 nm. Some of them are interconnected to each other.
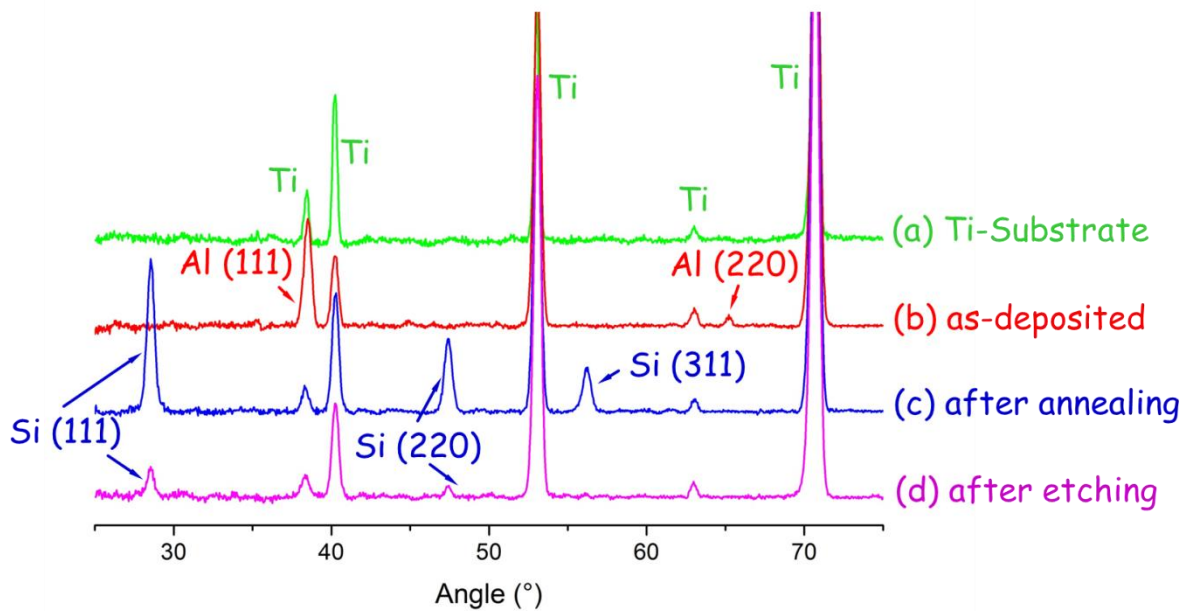
Fig. 5.9   **Characterization by XRD of the sample with a 10:1 ratio between Si and Al in different fabri-cation stages: green line: reference measurement of Ti-substrate; red line: as-deposited Al/a-Si bilayer; blue line: after annealing of the Al/Si bilayer at 600 °C for 30 min; purple line: after further etching of the annealed Al/Si bilayer.[64, 69]**

In the XRD pattern of the annealed specimen, the Al-induced crystallization of a-Si is clearly evidenced by the appearance of strong diffraction peaks of Si(111), Si(220) and Si(311) (blue line in Fig. 5.9) comparing to the diffraction pattern of the as-deposited sample (red line in Fig. 5.9). At the same time, the "exchanged" Al has now diffused into the original a-Si sub-layer (observed by Fig. 5.8b). At the annealing temperature of 600 °C (i.e. above $T_{\mathrm{eutectic}} = 577$ °C), Al would melt eutectically with about 13 at.% Si content (according to the Al-Si phase diagram) and form plenty of these nanosized eutectic melt droplets distributed throughout the Si layer (Fig. 5.8b and d). In the XRD pattern of the annealed specimen (blue line in Fig. 5.9), diffraction peaks corresponding to crystalline Al have indeed disappeared, further evidencing the formation of Al-Si eutectic droplets. It follows that, upon fast cooling of the specimen after annealing (600 K/min), these eutectic Al-13%Si melt droplets have solidified rapidly

without crystallization and phase separation, and thereby are in an amorphous alloy state after cooling to room temperature. By rinsing the annealed specimen in NaOH solution, the interconnected Al-13%Si nano droplets distributed throughout the Si layer can selectively be etched off, thus generating a highly nanoporous Si framework. After flushing of the etched specimen with distilled water, large parts of the c-Si overlayer has been washed away under the effect of its residual stresses.[54] Correspondingly, the diffraction peaks related to c-Si have pronouncedly decreased (purple line in Fig. 5.9). As a result of the above procedures, a highly nanoporous Si framework is consequently generated; see e.g. Fig. 5.8e. The observed very weak diffraction peaks of c-Si of the specimen indicate that the nanoporous Si framework is partially nanocrystalline.
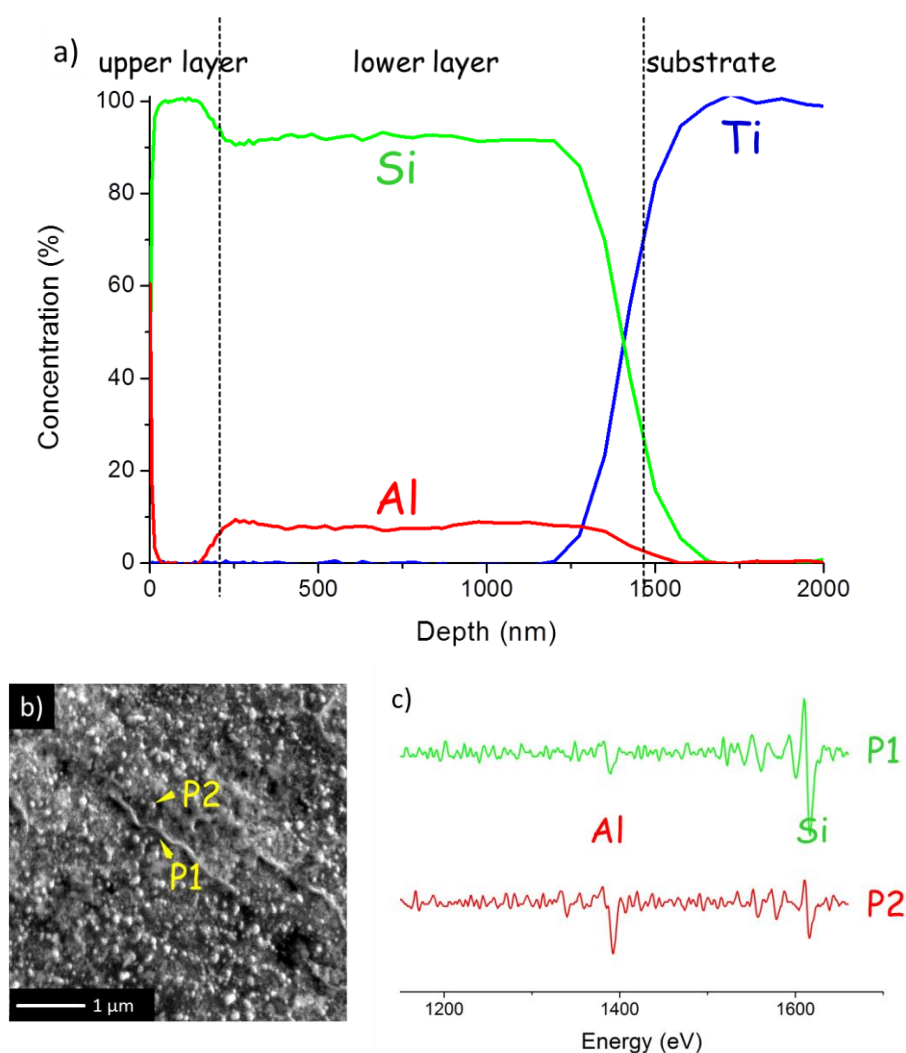
Fig. 5.10 **a) Molar concentration depth profile of the Al/Si bilayer sample after annealing by Auger electron spectroscopy (AES); b) surface secondary electron image of the lower layer with AES spots at different area (P1 at the dark area, P2 at the bright area). The sample was ion-etched with Ga ions to remove the upper layer away; c) AES analysis from P1 and P2. For P1 a strong Si signal is seen and the Al signal is very weak, whereas for P2 both signals are evident.[69]**

Auger electron spectroscopy (AES) depth profiling was used to obtain the elemental concentration-depth profiles of the annealed Al-Si bilayer as shown in Fig. 5.10a. It confirms the occurrence of almost complete exchange of Al and Si with the observation of ~100 at.% Si at the top layer (~ 150 nm) and negligible Al at the same location. Instead, a nearly constant Al molar concentration of about 10% is observed across the lower layer zone with about 90 at.% Si, indicating the uniform diffusion and distribution of Al-rich droplets in the Si matrix. Note that the interface between the lower layer and the Ti substrate appears to be broad in the AES depth profile. The rough surface of the Ti substrate may lead to this phenomenon. Moreover, an interdiffusion between Si and Ti may have occurred during annealing at this temperature and led to interfacial Ti silicides,[23] which are likely amorphous due to the lack of corresponding X-ray diffraction peaks (Fig. 5.9c). Such interfacial reaction could promote the close contact of active materials with substrate surface, suppress their delamination, facilitate electron transport from substrate, and be responsible for the improvement of electrochemical performance as discussed below. The local elemental distribution in the sample has been investigated by AES local analysis. The top view SEM image (Fig. 5.10b) and the following spot AES-spectra (Fig. 5.10c) deduce that the dark matrix region (P1 in Fig. 5.10b) is corresponding to practically pure Si (green curve in Fig. 5.10c), whereas the bright droplets region (P2 in Fig. 5.10b) contains an Al-rich phase (red curve in Fig. 5.10c).
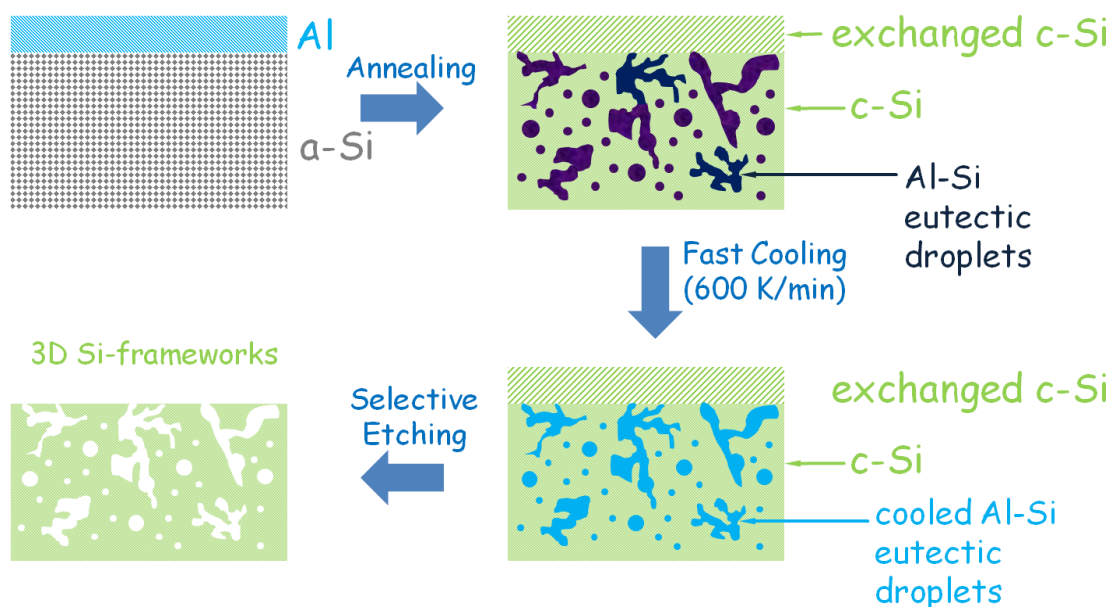
Fig. 5.11   **Procedure to fabricate the Si-frameworks with nanoporous structure from Al/Si bilayers, which is with a Al/Si ratio 1 to 10.**[69]

Fig. 5.11 summarizes the whole procedure to fabricate the Si frameworks with nano-porous structure. During the annealing the Al diffuses downwards into the original a-Si layer similar

to the case of the annealing below the eutectic temperature. The difference is that Al-Si eutectic liquid phase forms above the eutectic temperature instead of solid Al precipitations. Simultaneously, Si 'free' atoms migrate into the original c-Al layer and crystallize there. So the layer exchange occurrs in the sample annealed above the eutectic temperature just in the same manner as below the eutectic temperature. Due to the fast cooling by gas flow of Ar, the Al-Si eutectic liquid phase solidified into a nonequilibrium Al-Si solid phase, which forms an interconnected network. With the aid of alkali solution this nonequilibrium Al-Si phase can be etched away. The upper exchanged c-Si layer will be detached automatically due to the internal stress,[54] which is induced by the asymmetric diffusion between the Si and Al layer. Finally, the nano-porous Si frameworks remain.

5.2.2 Chemical composition of oxide coating after selective etching

After the selective etching of Al with NaOH solution, X-ray photoelectron spectroscopy (XPS) is performed to investigate the chemical composition of the sample.
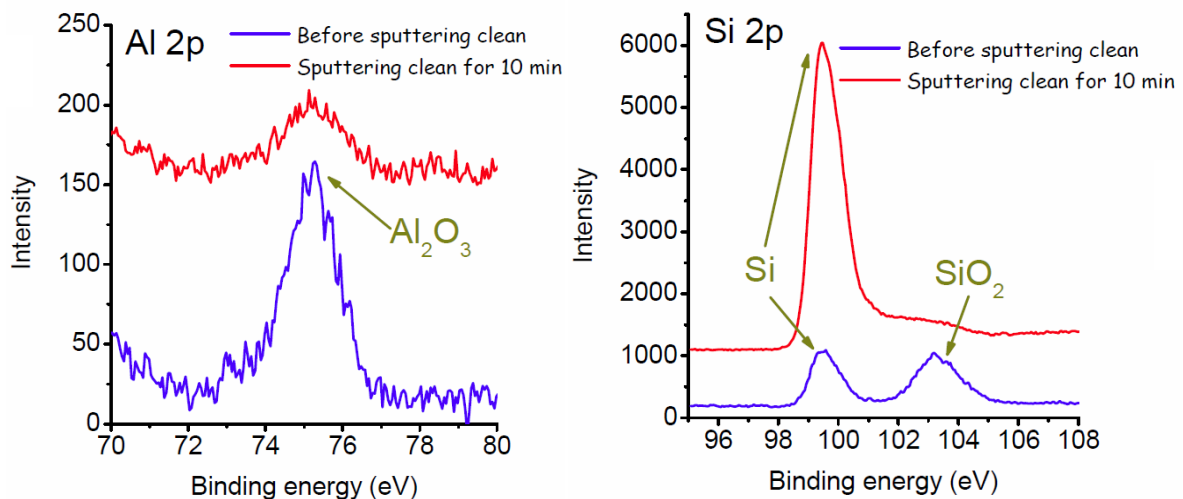
Fig. 5.12 XPS spectra of Si 2p, Al 2p of oxide-coated a-Si thick film and that after surface sputtering clean by Ar$^+$ for 10 min (20 nm deep from sample surface). The oxide coating layer of about 20 nm thickness consists of components such as SiO$_2$, Al$_2$O$_3$ formed by either natural oxidation or alkali etching.[64, 65]

The blue curves in Fig. 5.12 are received from the surface of the crystallized Si after selectively etching of Al. Within the XPS information depth of a few nanometers, the surface layer consists of Si (99.4 eV), SiO$_2$ (103.3 eV, possibly formed by natural oxidation),[70] Al (75.3 eV) and Na (1072.5 eV). These signals decay away practically within 20 nm into the depth as seen by the signals taken at a respective surface exposed by 1 keV Ar$^+$ ion sputtering for 10 min, see red curve in Fig. 5.12. As the information depth of XPS is only about 5 nm, this observation indicates the presence of a thin oxide coating of about a few nm thickness on the

surface. From the reaction with CO_2 (from ambience atmosphere) it is understandable that small amounts of Al_2O_3 and Na_2CO_3 remain at the surface after etching wash and drying in Ar flow.[71, 72]

High-resolution transmission electron microscopy (HRTEM) and electron energy-loss spectroscopy (EELS) provide another way to investigate the atomic structure and composition of Si-based porous framework, respectively (Fig. 5.13). The HRTEM cross-section through the Si-based porous framework (Fig. 5.13a) shows an amorphous nanoscale layer approximately 5 nm thick encapsulating the inner crystalline phase. From the EELS core-loss spectra (solid line in Fig. 5.13b), the Al and Si signals are both detected in the specimen based on the standard values referred to [73]. After removing the background signal, the L_{23} edge spectrum from Al was received at 75 eV (red solid curve in Fig. 5.13b), which is comparable to the referential standard spectrum referred to [73] (red dotted line in Fig. 5.13b). At 1840 eV another edge spectrum was also found (green solid line in Fig. 5.13b). Referring to [73] (red dotted line in Fig. 5.13b) it belongs to the Si K-edge spectrum.

However, Al, Si and their oxides can be hardly distinguished from each other in the core-loss spectrum. In order to discriminate the chemical bond status of Al and Si we resort to the energy-filtering transmission electron microscopy (EFTEM) mapping at the low-loss EELS spectra (Fig. 5.13d).[74] By using the Non-Linear Least Squares Fitting (NLLS) technique, the plasmon peak position of the spectrum from every pixel could be determined. Such low-loss EELS spectra have been used for elemental mapping and the lower micrograph of Fig. 5.13c shows a respective color-coded overlay of the pixel-wise analysis. Inside the specimen the peak of almost every pixel (e.g. P1 in Fig. 5.13c) locates at 17 eV in the low-loss EELS spectra (green solid curve in Fig. 5.13d). It is the characteristic signal of pure Si (green dotted curve in Fig. 4d), which is quite different from its oxide (green dashed curve in Fig. 5.13d) and also different from Al and its oxide (red dotted and dashed curve in Fig. 5.13d). Combined with the HRTEM image (Fig. 5.13a), it indicates that the inner green region in Fig. 5.13c consists of c-Si. Consequently, the Al signal in the core-loss spectra (red solid curve in Fig. 4b) can only result from the outer region of the samples. The spectra of pixels at the outer region (e.g. P2 in Fig. 5.13c and red solid curve in Fig. 5.13d) have an obvious maximum at 24 eV, in accordance with the reference values of Al and Si oxides staying at 24 eV (red dotted and green dashed lines in Fig. 5.13d), but different from the signal of pure Al or Si with a peak at 15 eV or 17 eV (red dashed or green dotted line in Fig. 5.13b). Thus, this amorphous surface layer consisting of Al and Si oxide with several nanometers is successfully investigated with different measurements.
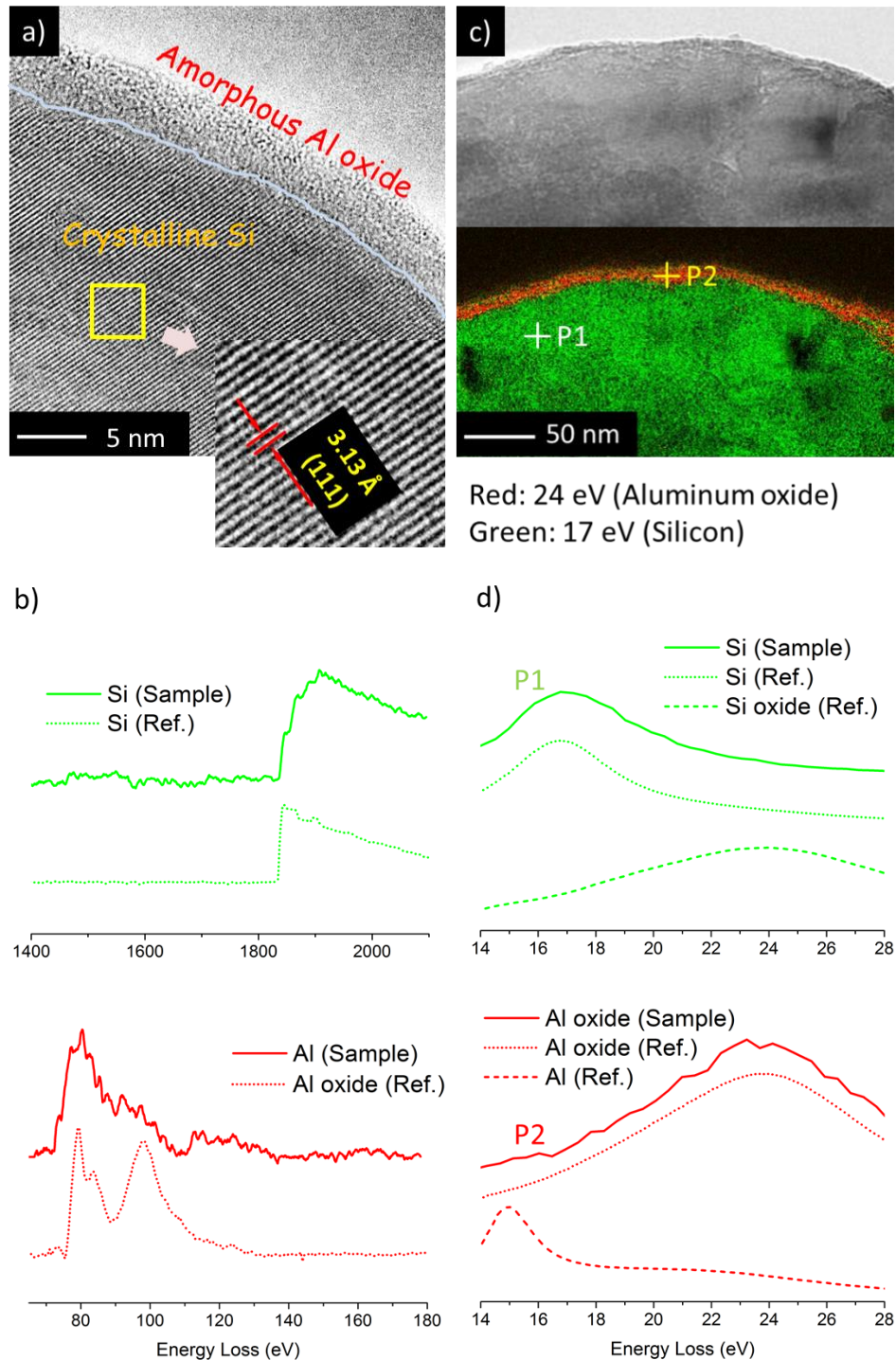
Fig. 5.13 **a) HRTEM image of the same specimen: an amorphous Al oxide layer formed on c-Si surface; b) EELS core-loss spectra of specimen after etching (red solid line for Al and green for Si). The reference values of Al and Si components are also labeled (corresponding dotted lines): Al L$_{23}$-edge spectrum without background (red) and Si K-edge spectrum without background (green); c) Bright-field image (above) and overlaid colored-coded (red for Al oxide and green for Si) EFTEM-mapping (below) based on plasmon peak positions (see d); d) EELS low loss-spectra taken from area marked by the dots P1 (green curve) and P2 (red curve). The reference spectra of Al, Si and their oxides are also labeled as a comparison.[69]**

To test the influence of the oxide layer on the electrochemical performance of Si anode mini-mized the influences from other factors, a reference sample of pure amorphous Si layer was fabricated, e.g. the same thick amorphous Si layers deposited on the same substrate (Ti-foils) with the same sputtering parameter. The electrochemical experimental condition was the same as the sample with a conformal oxide coating. Fig. 5.14 shows the comparison of the gal-vanostatic performance between the uncoated a-Si (red points in Fig. 5.14) and oxide coated a-Si (blue points in Fig. 5.14) under the same charge velocity (0.1 C). Due to the irreversible continual phase transformation between the Si electrode and the organic electrolyte during the cycling, [75] the charge capacity faded very fast in the uncoated a-Si within the first several cycles (red solid points in Fig. 5.14). This newly formed phase is named solid electrolyte in-terphase (SEI). In addition, it caused also the lower coulombic efficiency. As it is seen in Fig. 5.14, the coulombic efficiency in the uncoated a-Si varies from 40 % to maximal 80 % (red hollow points in Fig. 5.14). The coulombic efficiency in the oxide coated a-Si stayed always at almost 100 % (blue hollow points in Fig. 5.14). According to the experimental results from *Y. He* et al., [45] the surfacial Al oxide can prevent the reaction of Si anode with the electrolyte, to form the SEI layer. Furthermore, this Al oxide layer is also a mechanical enforcement against the volume expansion in the Si layer during the lithiation process.[45]
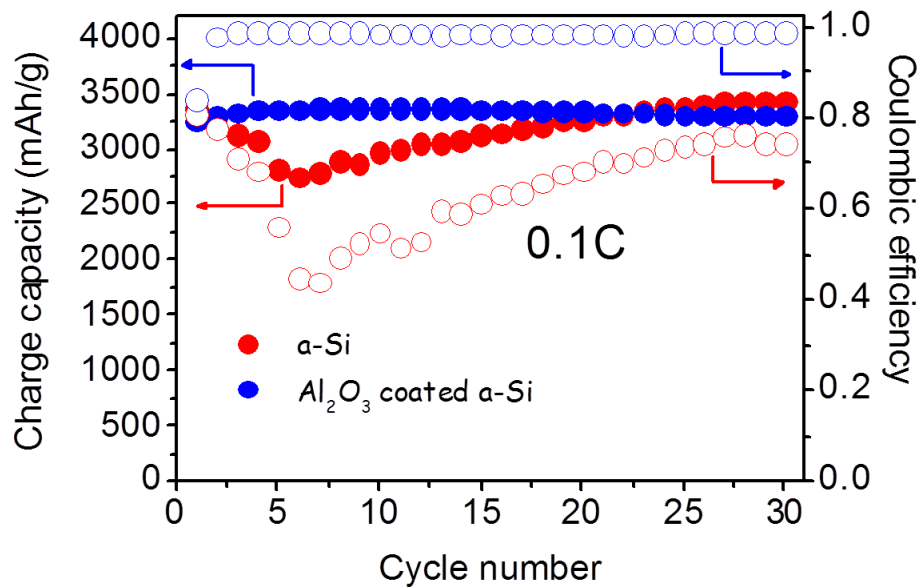
Fig. 5.14 **The charge capacity at 0.1C under a cycling up to 30 cycles: red points: uncoated a-Si; blue points: alumina coated a-Si. The hollow and the solid points indicate respectively the cou-lombic efficiency and the charge capacity of the specimens. The coulombic efficiency of un-coated specimen is much lower than the coated one. Within the first cyclings the charge capac-ity of uncoated a-Si faded very fast.[65]**

5.2.3 Electrochemical performances of porous Si layers

By purposely interrupting the crystalline Si layer growth at the different temperatures, various porous structures are developed. To inspect their suitability as the anode material of lithium ion batteries, the electrochemical performances of these porous Si films were tested.

5.2.3.1   Highly corrugated Si layer below the eutectic point

The highly corrugated Si film, which was annealed at 450 °C for 30 minutes, was amount in the Swagelok-cell as work electrode. As reference specimen, a compact amorphous Si film with the same thickness and also coated with Al oxide was also tested simultaneously. Fig. 5.15 shows the voltage vs. capacity plot of Al oxide coated massive amorphous and porous crystalline Si film. During the first discharge on the amorphous Si film the voltage decreases steadily with the calculated capacity (Fig. 5.15a), while the first voltage curve of the crystalline Si film shows a plateau below 0.1 V, which agreed with its crystalline character (Fig. 5.15b). The following discharge curves of the porous crystalline Si film become sloped with enhanced reaction voltage ranging from 0.3 to 0.01 V (Fig. 5.15b), which is similar to the amorphous Si (Fig. 5.15a). It indicates an irreversible amorphization of the c-Si during the first lithiation as reported before.[76]
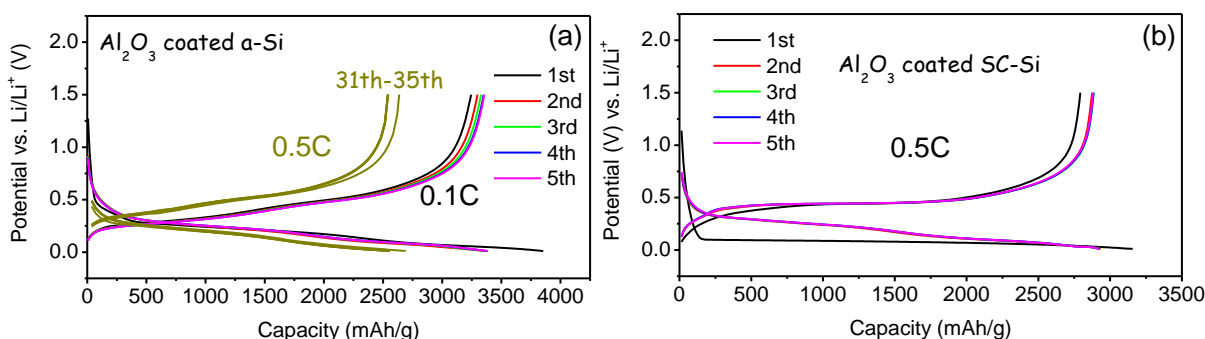
Fig. 5.15   Comparision of electrochemical testing between the Al$_2$O$_3$-coated a-Si and SC-Si films: Voltage vs capacity profiles of Al$_2$O$_3$-coated a-Si (a) and SC-Si thick films (b) as anodes at 0.1C or 0.5 C during the first five cycles or the later cycles at 0.01-1.5 V.[65]

The charge capacity of the massive amorphous Si film increases in the first 30 cycles, then fades very quickly. Up to 500 cycles its capacity is less than 250 mAh/g (blue curve in Fig. 5.16). Benefiting from the porous structure and conformal oxide layer to buffer the volume expansion, the crystalline film displays a significantly better cyclability up to 500 cycles (red curve in Fig. 5.16). Although there is a capacity loss in the first 50 cycles, the charge capacity recovered to 2000 mAh/g up to 150 cycles. In the following 150 to 500 cycles the charge capacity kept a high performance.
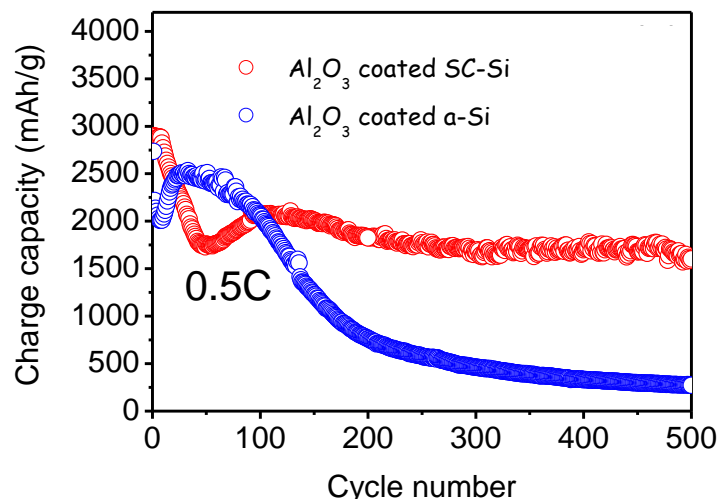
Fig. 5.16 **The charge capacity of coated a-Si and SC-Si thick films at 0.5C under a long-term cycling up to 500 cycles.**[64, 65]

The charge capacity of the both samples was also tested with different charge rates from 0.1 C to 8 C (here unit C stands for capacity. 0.1 C means that 10 hours are needed to charge the battery to its theoretical full capacity). Fig. 5.17a shows the charge capacity of the oxide layer coated compact amorphous Si. Up to 0.5 C it performs well with a high capacity without an obvious fading at about 2500 mAh/g, in the initial state. But with 2 C the capacity becomes very low and decreases very quickly. Within 10 cycles it reduces from about 1000 mAh/g to less than 500 mAh/g. In contrast, the porous crystalline Si with oxide layer coated preserves a very good capacity under high charge rates (Fig. 5.17b). Even with 8 C its capacity stays still more than 1000 mAh/g.
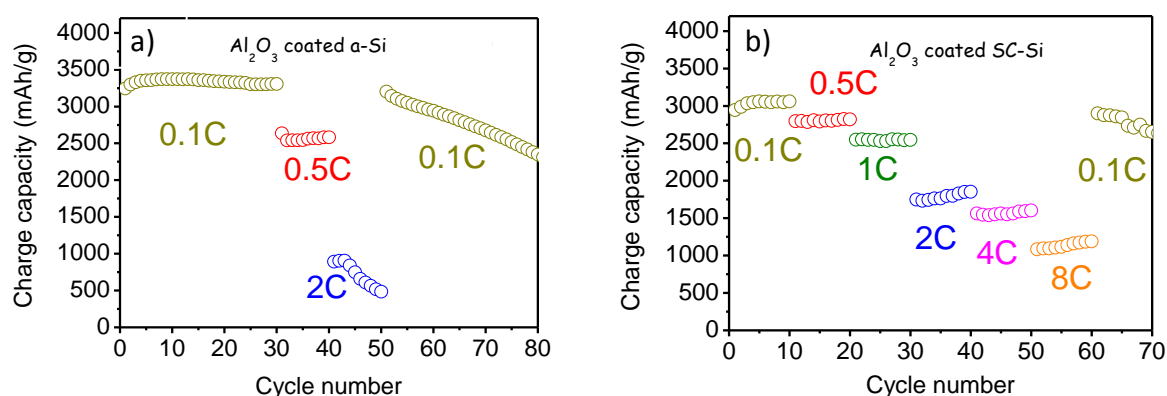
Fig. 5.17 **The charge capacity of coated a-Si (a) and SC-Si (b) thick films were tested with different rates from 0.1C to 8C.**[64, 65]

From the curve of the charge capacity vs. the cycle number (Fig. 5.16) it could be divided into three stages: initial stage, intermediate stage and final stage. At the initial stage the charge capacity fades very quickly. It is likely caused by the contact loss between the main part and

the top or side edge part of SC-Si columns. In the intermediate stage the capacity recovers slightly. It can be attributed to the more exposure of newly formed Si facets to electrolyte during the electrochemical activation. The good retention of capacity in the final stage is indicated by the SEM morphology after longterm cycling (Fig. 5.18), wherein the inter-column spaces are moderately filled to tolerate volume extrusion.
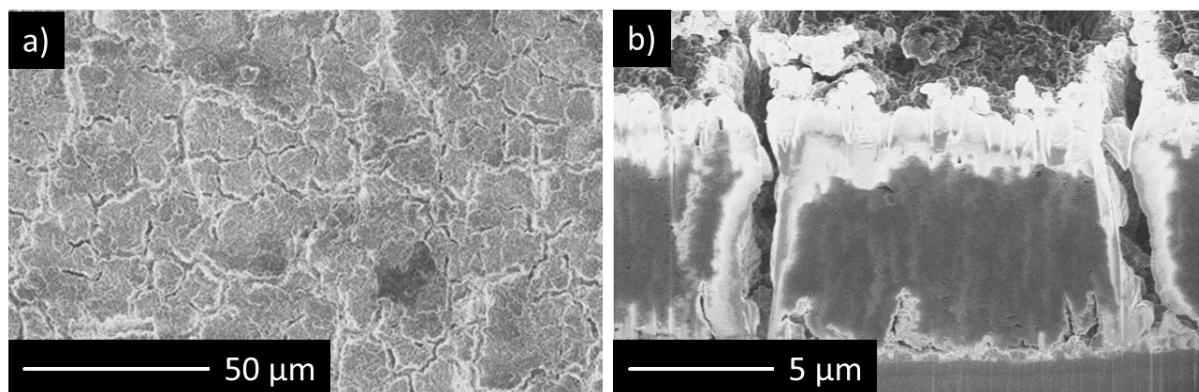
Fig. 5.18 **Surface SEM images of Al$_2$O$_3$-coated SC-Si thick film after longterm cycling. It is found that the original inter-column spaces are moderately filled due to volume expansion during long-term lithiation/delithiation. Macroscopically, no serious cracking and islanding phenomena can be observed as opposed to the case of as-deposited a-Si thick films.[65]**

5.2.3.2   Porous Si frameworks above the eutectic point

To test the electrochemical performance, the nano-porous Si framework, which was annealed at 600 °C for 30 minutes, was assembled in the Swagelok-type cell as working electrode. Fig. 5.19a indicates the galvanostatic performance of the porous Si frameworks in the additive-free electrolyte. Note that there is a sloped electrochemical curve with a substantial capacity of ~500 mAh/g during the first lithiation from 1.5 V to 0.1 V, where a typical plateau curve is followed until the ending of discharge. The voltage plateau is the feature of lithiating poly-Si, which however disappears in the following discharge curves (instead displaying sloped discharge curves between 0.5 and 0.01 V) due to irreversible amorphization of poly-Si during the first cycling. The charge processes always display sloped curves from 0.2 V to 0.7 V. One should note that the capacity (colorful curve in Fig. 5.19a) and coulombic efficiency (green solid points in Fig. 5.19b) are both remarkably improved during the early cycling. As shown in Fig. 5.19a, the charge capacity is increased from ~1370 mAh/g to ~2150 mAh/g with the coulombic efficiency from 67% to 98% at 0.1 C in the first twenty cycles. This unusual electrochemical activation should be ascribed to the more exposure of original or newly formed Si surfaces to the more infiltrated electrolyte inside the porous framework.
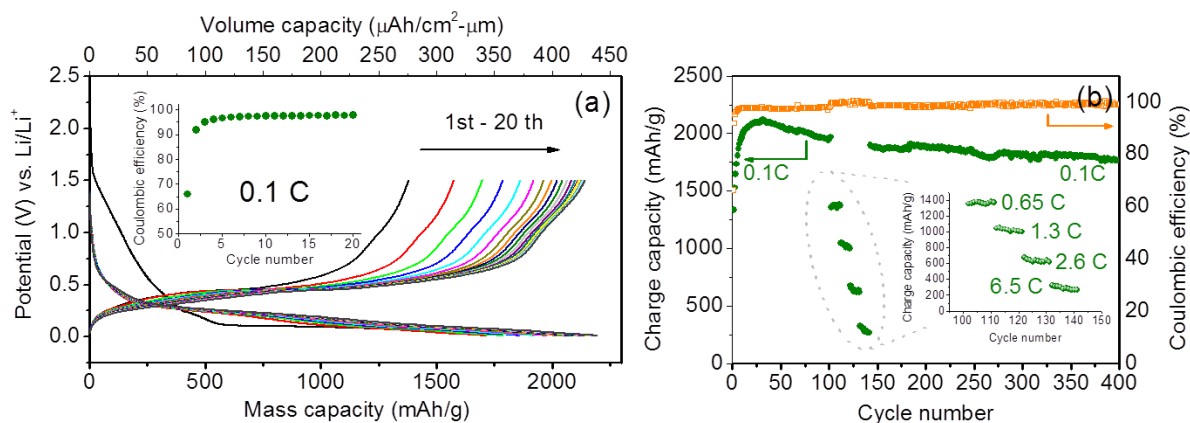
Fig. 5.19 **Electrochemical testing of the specimen, which was annealed at 600 °C: a) voltage vs. capacity profile in the first 20 cycles. The capacity increased very fast within the first 5 cycles. Then it rose slightly within the next cycles; b) the charge capacity at 0.1C under a long-term cycling up to 400 cycles (green curve). After 400 cycles the charge capacity kept always 75 % of the maximal charge capacity. The specimen was also tested with different rates from 0.65 C to 6.5 C. The coumlobic efficiency stayed always near 100% during the whole electrochemical testing process (orange curve).[69]**

The reversible capacity with a coulombic efficiency as high as 99% (orange curve in Fig. 5.19b) is still preserved at ~1780 mAh/g after a long-term cycling of 400 times, about 83% of the maximum capacity achieved at the 30th cycle (green curve in Fig. 5.19b). The excellent cyclability benefits not only from the nanoporous structure for extra volume accommodation and strain release, but also from the conformal coating and p-doping for extra ion/electron conductive networks as well as for less accumulation of electrochemically driven SEIs. The reversible capacities of 1000 mAh/g and 600 mAh/g are also achievable at the higher rates of 1.2 C and 2.4 C respectively. After undergoing a high-rate cycling at 6 C, the capacity at 0.1 C is still recoverable when the current density returns to 0.1 C after 150 cycles, indicating the robustness of Si framework structure under fast or long-term lithiation/delithiation.

Indeed, the nano-porosity and interconnectivity of frameworks are well preserved after long-term galvanostatic test as shown by the SEM morphology of the cycled specimen in Fig. 5.20. In view of the quite large volume-specific capacity (e.g. ~430 mAh/cm2-mm at the 20th cycle and ~350 mAh/cm2-mm at the 400th cycle), this Si porous framework is also thought to be a potential 3D anode for all-solid-sate micro-batteries as long as the pore regions can be partially filled by solid electrolyte components as ion-wires.
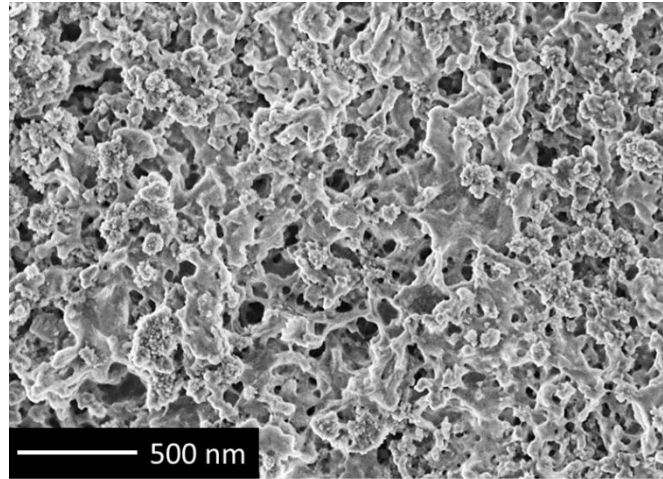
Fig. 5.20   SEM morphology of the cycled specimen after long-term galvanostatic testing[69]

5.3 Discussion

5.3.1 Crystallization of a-Si in Al triple junctions and grain boundaries

Referring to [50], the crystallization of a-Si in the Al grain boundaries was thermodynamically explained (Chapter 2). Based on this thermodynamic model, the crystallization of Si at interface between the original amorphous Si and crystalline Al layer is not an energetically favorite way. However, as observed results in section 5.2.1.1, amorphous Si can crystallize in the Al triple junctions largely under the eutectic point instead of the crystallization at Al grain boundaries. According to the geometrical as well as energetic differences to the grain boundaries, a model will be developed here, to thermodynamically distinguish the crystallization of a-Si in Al triple junctions and grain boundaries.
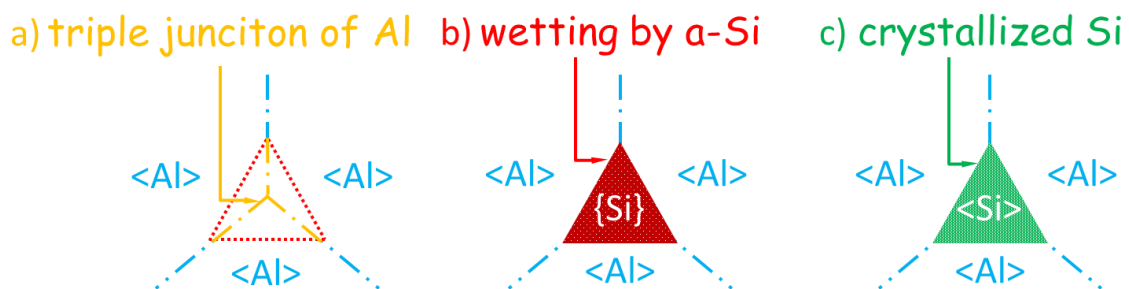
Fig. 5.21   In the simplest case of the triple junctions wetting, three ideal symmetrical Al grain boundaries with the equal grain boundary energy $\gamma_{\langle Al \rangle}$ are wetted by amorphous Si. New interfaces between the amorphous Si and crystalline Al are formed. Referring to the geometric relationship, the wetting condition is: $\gamma_{\langle Al \rangle / \{Si\}}^{triple} = \sqrt{3} \cdot \gamma_{\langle Al \rangle / \{Si\}} < \gamma_{\langle Al \rangle}$. Above a critical thickness Si crystallized in the triple junction of Al

B Straumal et al. constructed a simplest model to demonstrate the thermodynamic possibility for the wetting of the amorphous phase in the triple junctions. [77] This model will be applied here in the case of the in Al-Si system (Fig. 5.21). In this model the grain boundaries at the triple junction are not only geometrically but also energetically symmetrical (orange dot-dashed line in Fig. 5.21a). A triangle prism filled by the amorphous Si replaced the vicinity of the triple junction of the Al grains (red region in Fig. 5.21b).

According to the geometric relationship, after wetting the length of interface between the amorphous Si and crystalline Si (red dot line in Fig. 5.21a) is $\sqrt{3}$ times as long as the original Al grain boundaries at the triple junction (orange dot-dashed line in Fig. 5.21a). Thus, the wetting condition must be:

$$\gamma_{\langle Al \rangle / \{Si\}}^{triple} = \sqrt{3} \cdot \gamma_{\langle Al \rangle / \{Si\}} < \gamma_{\langle Al \rangle} \qquad \text{Eq. 17}$$

where $\gamma_{\langle Al \rangle / \{Si\}}^{triple}$ stands for the specific wetted interface energy between a-Si/c-Al at the triple junction, $\gamma_{\langle Al \rangle / \{Si\}}$ for the specific interface energy in the planar a-Si/c-Al interface and $\gamma_{\langle Al \rangle}$ for the specific grain boundary energy of Al.
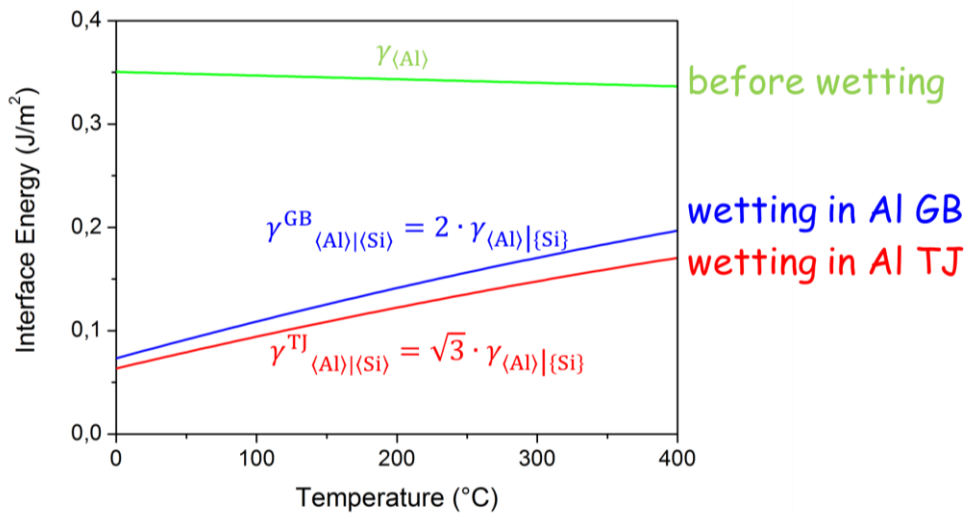
Fig. 5.22   **After wetting with the free Si atoms, the total specific interface energy of c-Al/a-Si in the Al triple junctions (red curve) is lower than the grain boundary energy of the crystalline Al (green curve). Compare to the model of wetting in the Al grain boundaries (blue curve), wetting in the Al triple junctions is more energetically favourable.**

Referring to Eq. 44 and 53, the specific interface energy in the triple junction before and after wetting can be calculated. Fig. 5.22 shows the calculated value of the specific grain boundary energy of Al (green curve in Fig. 5.22) and the specific interface energy after wetting of amorphous Si in Al triple junctions (red curve in Fig. 5.22), which is a function of the temper-

ature *T*. A positive difference between before and after wetting indicates that the reduction of the interface energy is the driving force for wetting Al triple junction with 'free' Si atoms. Compare to the specific interface energy after wetting of amorphous Si in Al grain boundaries (blue curve in Fig. 5.22), wetting in Al triple junction resulting in a lower specific interface energy is more energetically favorable.

Analog to the specific interface energy in the triple junction between a-Si and c-Al, that between the c-Si and c-Al can be also calculated with the same geometric relationship:

$$\gamma_{\langle Al\rangle/\langle Si\rangle}^{triple} = \sqrt{3} \cdot \gamma_{\langle Al\rangle/\langle Si\rangle} \qquad \text{Eq. 18}$$

$\gamma_{\langle Al\rangle/\langle Si\rangle}$ stands for the specific interface energy between c-Si and c-Al. According to Eq. 51, the specific interface energy of Si crystallized in the Al triple junction can be calculated (blue dot-dashed curve in Fig. 5.23). Due to the different geometric relationship between the triple junctions and planar grain boundaries, the crystallization of Si in Al grain boundaries generates a higher specific interface energy between c-Si and c- Al (red dot-dashed curve).
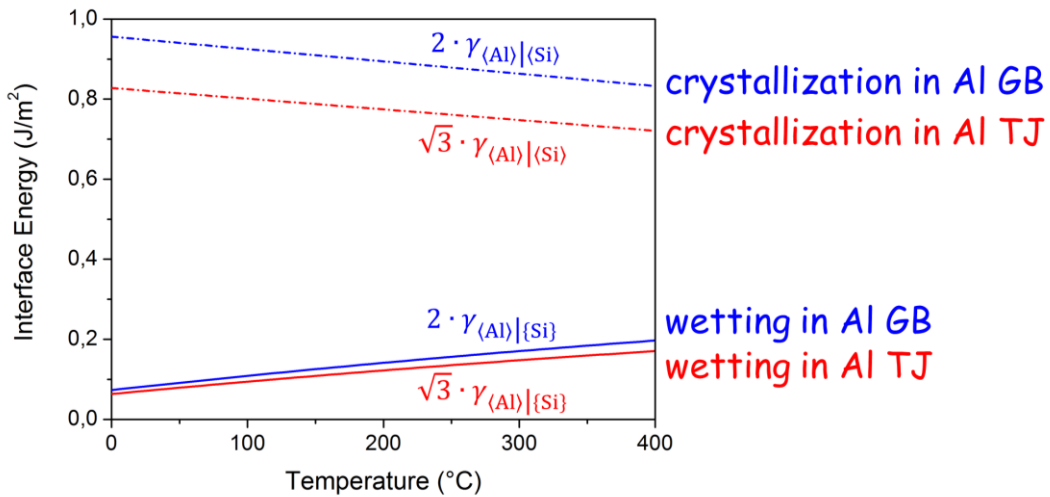
Fig. 5.23   **The interface energy between the crystallized Si and Al in the triple junctions (red dot-dashed curve) is higher than that of wetted Al triple junctions by a-Si (red line). The difference between them is the driving force for the crystallization of Si in the Al triple junctions, which reduces the total Gibbs energy of the whole system. The case of the crystallization of Si in Al grain boundaries will be also calculated (red dot-dashed curve and line) to compare the thermodynamic differences of these two models.**

Analog to the crystallization of Si in the planar Al grain boundaries, the crystallization energy of the amorphous Si can minimize the Gibbs' energy of the whole system in the Al triple junctions since a critical thickness of Si. Consequently, the critical thickness for the crystallization of Si in the Al triple junctions can be calculated at the corresponding temperature. Ana-

log to Eq. 3, the critical thickness for the crystallization of amorphous Si in the Al triple junctions can be described by:

$$h_{\text{Si at Al TJ}}^{\text{crit}} = \frac{\sqrt{3} \cdot \left(\gamma_{\langle Al \rangle / \langle Si \rangle}^{\text{interf}} - \gamma_{\langle Al \rangle / \{Si\}}^{\text{interf}} \right)}{-\Delta G_{\langle Si \rangle - \{Si\}}^{\text{cryst}}} \qquad \text{Eq. 19}$$

The critical crystallization thickness of Si in the Al triple junctions decreases with the increasing annealing temperature (red curve in Fig. 5.24). Unlike the case in the planar Al grain boundaries (blue dashed line in Fig. 5.24), the space for crystallization provided by the Al triple junction is $4\sqrt{3}$ monolayers (ML) (red dashed line in Fig. 5.24). Thus, the critical crystallization temperature of Si in both cases can be indicated by the intercept point from the normal curve and the dashed line with the same color (Fig. 5.24). Due to the much lower intercept point in the case of the Al triple junctions, Si can crystallize in the Al triple junctions at lower temperatures even if it can't occur in the case of the Al grain boundaries at the same temperature.
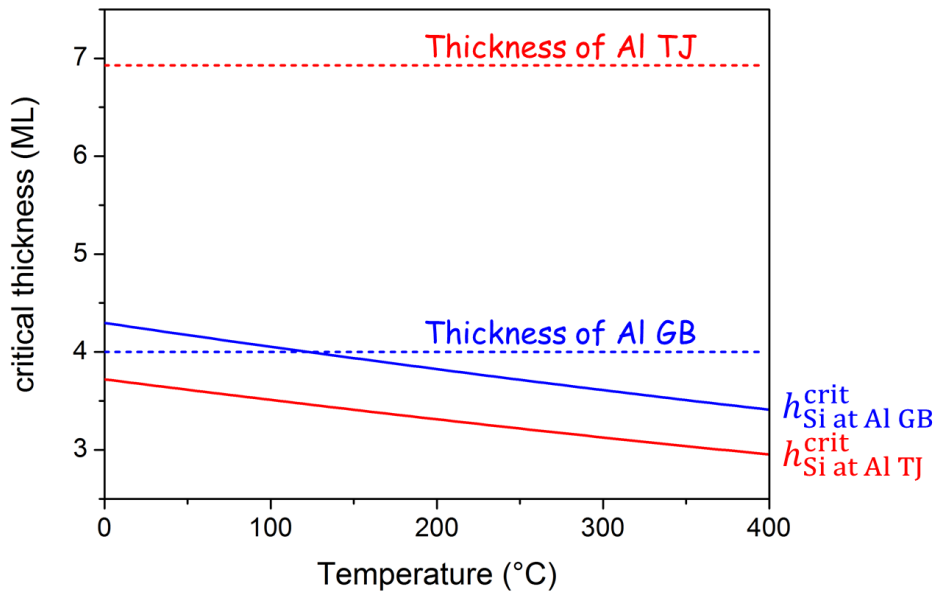
Fig. 5.24 **Theoretical critical thickness for the crystallization of Si inside the triple junction versus the annealing temperature (red curve). The spaces, which can be provided by the triple junction, are $4\sqrt{3}$ ML (red dashed line). Compare to the case of the crystallization in the Al grain boundaries (blue curve and blue dashed line), Si can crystallize in the Al triple junctions at lower temperature than in the Al grain boundaries.**

Furthermore, due to the abundant defect (e.g. vacancies) and the lower activation energy, the triple junctions are the fastest diffusion path. Generally, the diffusion coefficient in the triple junction is two to three order of magnitude higher than that at the grain boundaries at the low temperature.[78] Thus, at the low annealing temperatures the 'free' Si atoms would like to dif-

fuse along the triple junction of the Al grains at first. Therefore, nano-sized thin frameworks of c-Si can be constructed. At the higher temperature, the grain boundary diffusion is activated. The diffusion path as well as the crystallization zone of Si becomes 2-dimensional. Therefore, planar connected walls of c-Si can be formed.

5.3.2 Diffusion-controlled formation of various porous Si layers

The presented comprehensive investigation results deduce that distinctively different morphologies of the Si layer are formed at different annealing temperatures. This can be ascribed to different diffusion mechanisms of Si/Al bilayer at different temperatures. There are four basic types of diffusion mechanisms of Si in polycrystalline Al layer: triple junction diffusion, grain boundary diffusion, pipe diffusion and volume diffusion. Actually, it is incomplete to describe the whole diffusion process of Si in Al layer by a single above-named diffusion process. To describe this collective diffusion process, a new definition 'effective diffusivity' will be introduced. In the following section, the effective diffusivity of Si in Al layer and its influences on the annealing conditions will be discussed.

5.3.2.1 Effective diffusivity and diffusion processes

From the high-resolution transmission electron microscopy (HRTEM) a 'liquid-like' disordered structure was found in the triple junction.[79] Thus, the diffusion in the triple junction is comparable to the diffusion in the 'liquid-like' environment.[80] The diffusivity of Si in the triple junctions of Al grains can be found in Ref. [81]. The diffusivities of Si in Al in other three mechanisms, which are applied for this work to further discussion, are determined from the different diffusion experiments and listed in Tab. 1.

Tab. 1   Pre-exponential factor D_0 and the activation energy Q for Si diffusion in Al

Si diffusion in solid Al	D_0 (m²/s)	Q (kJ/mol)	T (K)	Ref.
volume diffusivity D_v	$2.6 \cdot 10^{-4}$	136.8	754 - 905	[82]
pipe diffusivity D_p	700	108.0	573 - 733	[83]
grain boundary diffusivity D_{gb}	760	174.6	393 - 423	[84]
triple junctions diffusivity D_{tj} (diffusivity in liquid Al)	$1.34 \cdot 10^{-7}$	30.0	> 933	[81]

For the further calculation, we assume that the diffusivities of Si in solid Al can be applied in the whole temperature range till the melting point of Al. Fig. 5.25 shows the comparison of the calculated diffusivity for the different diffusion mechanisms of Si in Al. In the whole temperature range up to the melting point of Al (T_m), the diffusivity of Si along the dislocation of

Al (bright blue line in Fig. 5.25) is larger than that in the Al grain boundaries (red line in Fig. 5.25) and larger than that in the bulk Si (blue line in Fig. 5.25). But up to a certain high temperature the pipe and triple junction diffusions of Si atoms are faster than the other two cases (green line in Fig. 5.25).

Besides the three dimensionally interconnected grain boundaries surrounding the Al grains, another important intergranular diffusion short circuit, triple junctions, should not be neglected, if the Al layer is a nanocrystalline layer. Moreover, the Al grains can also provide possible diffusion paths for Si atoms. Based on Fig. 5.25, the pipe diffusivity D_p is higher than the grain boundary diffusion. Therefore, the dislocations in the Al grains have also a partial contribution to the diffusion of Si in Al. Although the volume diffusivity of Si in Al grain is lower than the others, the flux from the volume diffusion of Si in Al grains should be considered above a certain high temperature due to its large diffusion area. Thus, the diffusion of Si in Al layer is a combined process of the Si diffusion in the intergranular regions and granular regions. In conclusion, to calculate the effective diffusivity of Si in Al layer (D_{eff}), the diffusion fluxes from these different diffusion mechanisms, which are described by the value of these four different diffusivities as well as the area fraction of respective contributing diffusion mechanisms, should be considered.
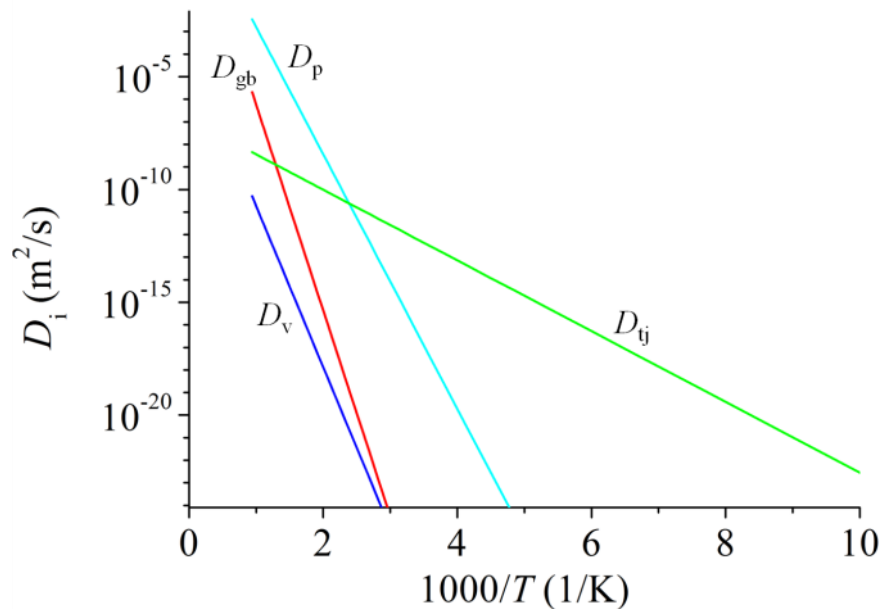
Fig. 5.25 **The diffusivities of Si in Al by four different diffusion mechanisms: triple junction diffusion (D_{tj}), grain boundary diffusion (D_{gb}), pipe diffusion (D_p) and volume diffusion (D_v)**

The area fractions of these four diffusion mechanisms, f_p (fraction of atomic sites in dislocation cores), f_{tj} (triple junction fraction), f_{gb} (grain boundary fraction) and f_v (intragranular volume fraction of Al layer), can be calculated by:[85]:

$$f_p = A_d \rho_d \qquad \text{Eq. 20}$$

$$f_{gb} = H_{gb} \frac{\delta}{d} \qquad \text{Eq. 21}$$

$$f_{tj} = H_{tj} \left(\frac{\delta}{d}\right)^2 \qquad \text{Eq. 22}$$

$$f_v = 1 - f_{gb} - f_{tj} \qquad \text{Eq. 23}$$

where H_{gb} and H_{tj} are dimensionless numerical factors that depend on the grain shape and grain size distribution. A_d is the pipe cross-section area. ρ_d stands for the dislocation density. δ and d denote the grain boundary thickness and average grain size, respectively. The grain size and grain size distribution can be easily investigated by electron backscattering diffraction measurement (EBSD).

According to Eq. 20, the dislocation density determines the contribution of the pipe diffusion on this diffusion mechanism. Actually, *Y. Chen et al.* found that even for the dislocation density as high as 10^{15} $1/m^2$, the calculated contribution of the pipe diffusion can be neglected here.[85] Due to the high area density of the triple junctions and grain boundaries in nanocrystalline materials, the effective diffusivity (D_{eff}) is also in dependence on the grain size of the Al layer.[80, 86]

Consequently, neglecting the effect of the pipe diffusion, *Y. Chen* et al. suggested that the effective diffusivity D_{eff} in the isotropic nanocrystalline materials can be calculated by:[85]

$$D_{eff} = \frac{1}{2 + f_v}\left[3f_v D_v + 2(f_{gb} + f_{tj})\frac{2f_{gb}D_{gb} + f_{tj}D_{tj}}{2f_{gb} + f_{tj}}\right] \qquad \text{Eq. 24}$$

Respectively, D_{tj}, D_{gb} and D_v stand for diffusivity of Si atom in the triple junction, grain boundaries of polycrystalline Al layer and bulk Al grains.

Similar to Eq. 21 and 22, the effective diffusivity D_{eff} has an exponential relationship to the grain size d. As a consequence, the types of the diffusion processes can be determined mathematically by the exponent of the grain size d. Therefore, the grain size exponent of the effective diffusivity m_a, which is suggested *by Y. Chen* et al., can reveal the dominant diffusion mechanism of Si in Al layer:[85]

$$m_a = -\left(\frac{\partial \ln D_{eff}}{\partial \ln d}\right)_T \qquad \text{Eq. 25}$$

According to the different diffusivity and its corresponding exponent of the grain size from aforementioned equations, the calculated m_a can be approximately classified to determine the dominant diffusion processes: volume diffusion ($m_a < 0.1$), dominant grain boundary diffusion ($m_a \to 1$) and triple junction diffusion ($m_a > 2$). $m_a = 0.5$ and $m_a = 1.5$ are the transi-

tion boundaries of dominance of volume diffusion to grain boundary diffusion to triple junction diffusion.

Based on the above-described interval of the grain size exponent of the effective diffusivity m_a, a calculated contour plot of the grain size exponent m_a of Si in Al layer in dependence on annealing temperature and Al grain size is established (Fig. 5.26). From this diagram a diffusion mechanism map can be constructed as function of the average grain size d and the temperature T. Because above the eutectic temperature $T_{eutectic}$ (577 °C) the liquid phase from Al and Si will be formed, the diffusion mechanism map was plotted till the homologous temperature at 0.9.
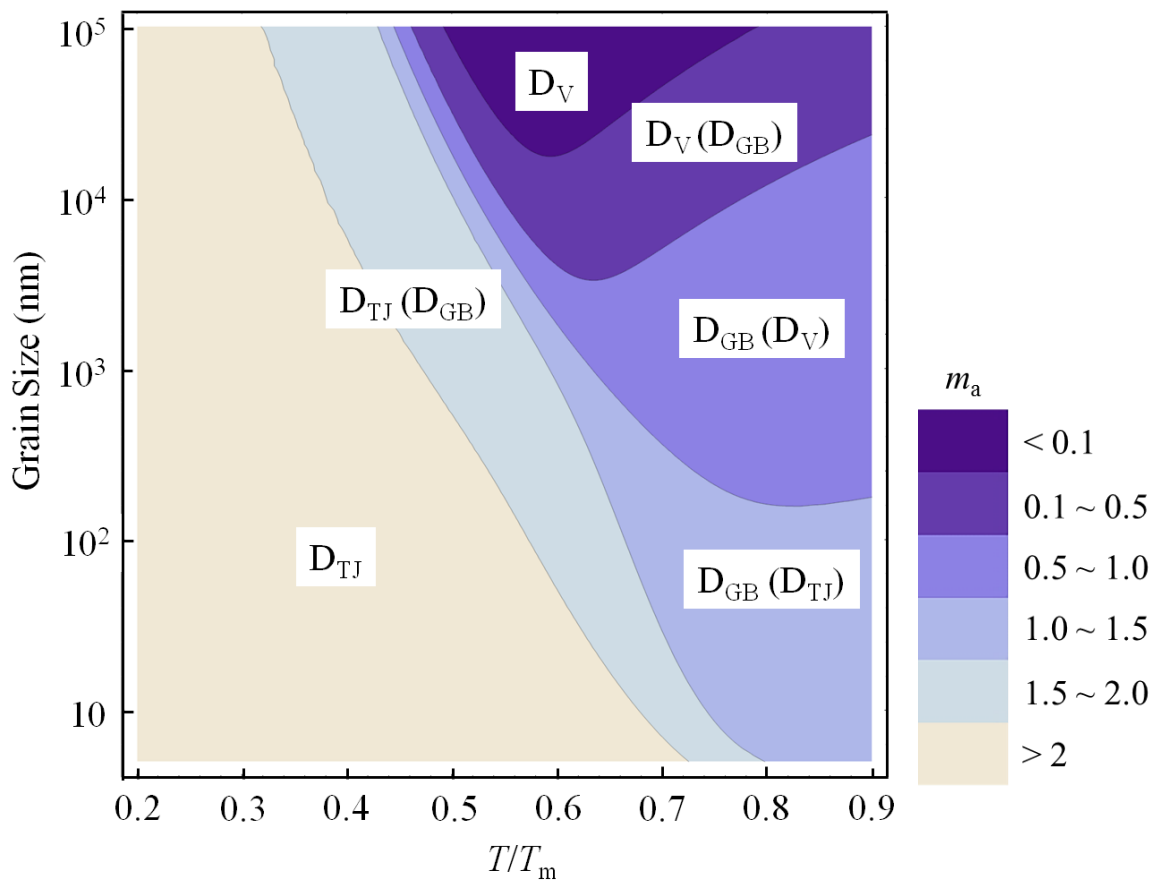
Fig. 5.26 **Diffusion mechanism map of Si in Al layer constructed using the contours of grain size exponents. The dominant diffusion process is denoted in each regime, while the secondary diffusion process was written in parentheses. 'D$_{TJ}$' stands for triple junction diffusion, 'D$_{GB}$' for grain boundary diffusion and 'D$_V$' for volume diffusion.**

In the Al layer with an average grain size smaller than 3 μm, Si diffuses along the triple junction at the low temperatures. Then the grain boundary and volume diffusion will be activated with the increasing temperature. In the Al layer with the coarse grains (above 3 μm) the grain boundary diffusion dominant regime (D$_{GB}$ (D$_V$)-regime) was divided by the volume diffusion

(D_V-regime) or volume diffusion dominant regimes (D_V (D_{GB})-regime). It can be explained that in Al layer with the coarse grains the density of the grain boundaries is low. According to Eq. 24, the effective diffusivity of Si in Al layer is determined not only by the diffusivity of the respective processes but also by the area fraction of respective diffusion path. Thus, in a certain temperature range the contribution from the volume diffusion can overweight that from the grain boundary diffusion.

5.3.2.2   Morphologies of porous Si layers formed by different diffusion processes

To investigate the diffusion processes of Si in Al in dependence on the annealing conditions as well as the developed morphologies of the crystallized Si, the Si/Al bilayer samples must be deposited under the same sputtering conditions. With the aid of the EBSD measurement, the information about the orientation and grain size distribution of the Al layer can be achieved (Fig. 5.27).
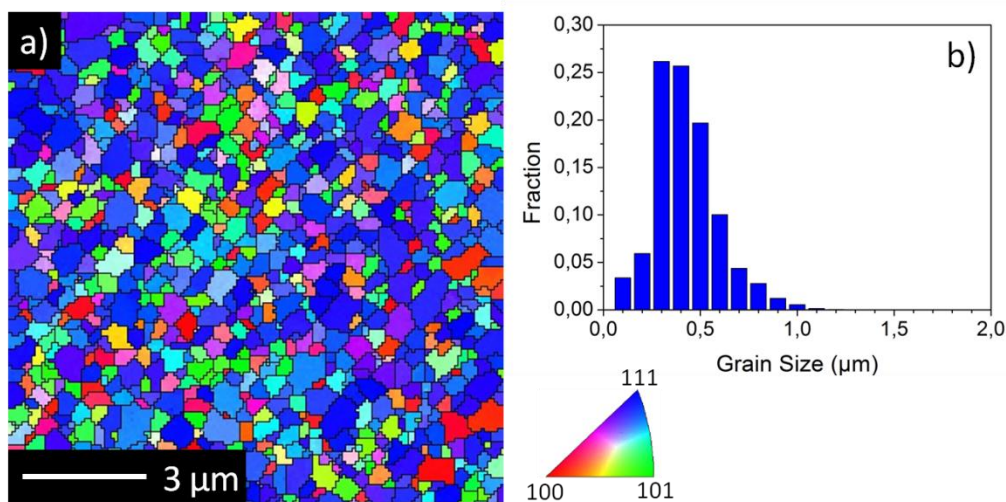
Fig. 5.27   a) Surface EBSD image with grain orientation mapping of as-deposited Al/Si bilayer film before annealing; b) grain size distribution of top Al calculated by EBSD analysis. The top Al layer shows typical polycrystalline characteristics with grain orientation mainly along (111) in the normal direction and grain size ranging mainly from 100 to 1100 nm.

With the calculated average grain size d 400 nm of the Al layer, the dominant diffusion process of Si in Al layer can be found out from the diffusion mechanism map in dependence on the annealing temperature range (dashed line in Fig. 5.26). Fig. 5.28d shows a plot of the grain size exponent m_a as a function of the homologous temperature T/T_m with an average grain size of 400 nm in the Al layer. In the various temperature ranges, in which different diffusion processes dominate, the morphology of the crystallized Si is also quite different (Fig. 5.28a, b and c).
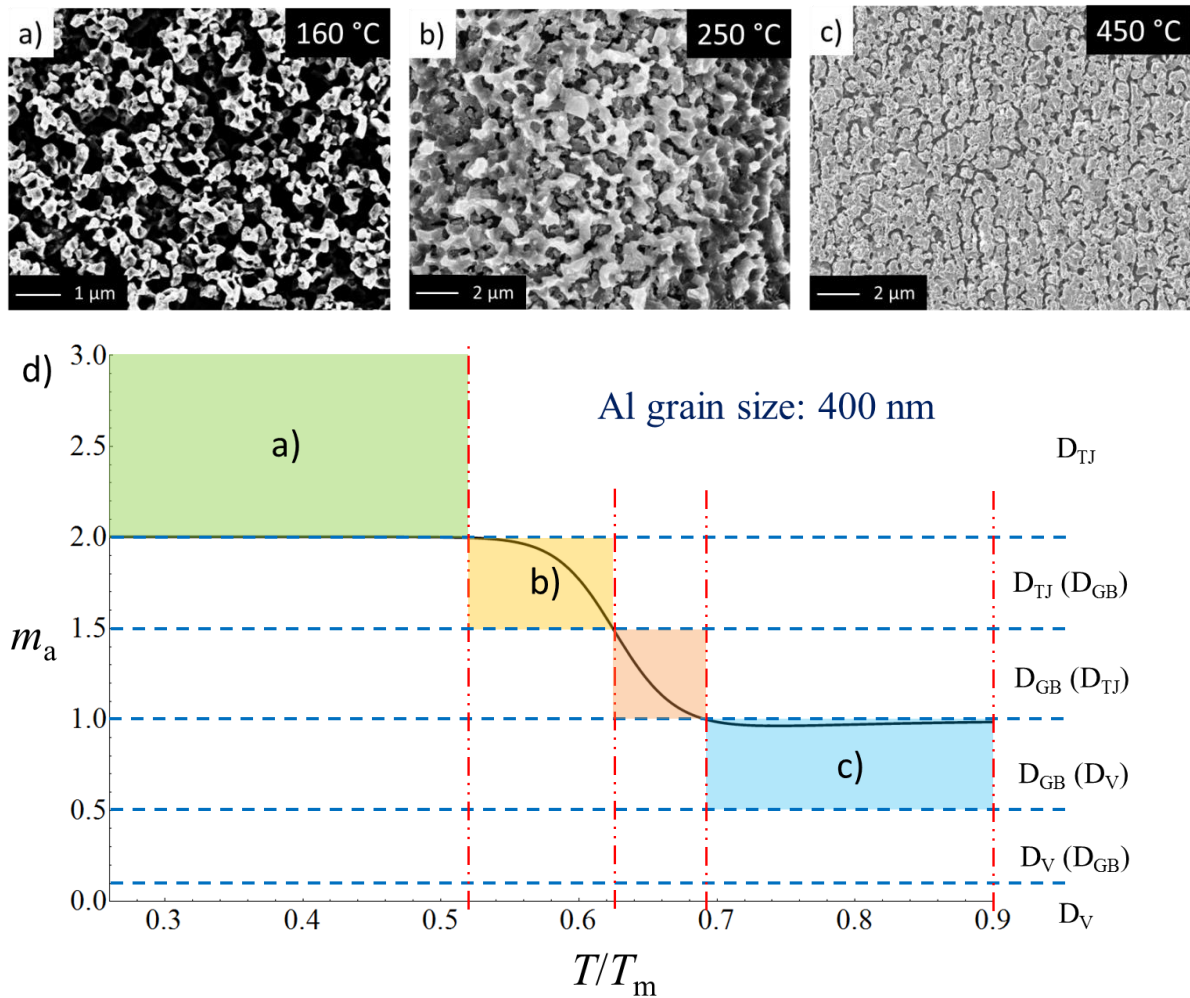
Fig. 5.28   The annealing temperature influences the morphology of the crystallized Si with the same average Al grain size, because in the various temperature ranges the different diffusion processes is dominant. d) shows the grain size exponent m_a in dependence on the homologous temperature T/T_m with a constant average grain size in Al layer (400 nm) and the diffusion processes in every temperature range which interpret the architecture of the crystalline Si. a) annealed at 160 °C the diffusion path of Si is one dimensional like a pipe along the triple junction. 3D frameworks of crystalline Si were constructed; b) annealed at 250 °C the grain boundary diffusion takes part in the process. The diffusion path looks like two dimensional walls. The crystalline Si walls are built; c) annealed at 450 °C the volume diffusion can be also activated. The diffusion front is three dimensional and leads to the formation of a corrugated structure from crystalline Si.

From Fig. 5.28d it can be predicted that in the low temperature range ($T < 215$ °C) the Si atoms preferred diffusing along the triple junctions of Al grains. This has been confirmed by the FIB investigation in the previous section (Fig. 5.2). Above the critical thickness the amorphous Si crystallized in the wetted Al triple junctions. The crystalline Si needles with hundred nanometers diameter connect to each other and form 3D frameworks (Fig. 5.28a). In a higher

annealing temperature range (215 °C < T < 310 °C) the grain boundary diffusion takes part in the diffusion process. The Si atoms diffuse not only along the triple junctions but also along the grain boundaries in the Al layer. The diffusion path is not one dimensional like in pipes any more but two dimensional like in walls. Thus, crystalline Si walls are finally formed (Fig. 5.28b). In still higher temperature range (370 °C < T < $T_{eutectic}$), the volume diffusion of Si occurs, which involves the intermixing process between Si and Al. The diffusion front of the Si atoms is three dimensional. It leads to a strong intermixing between the Si and Al layer and consequently to an evolution of a corrugated structure of crystalline Si (Fig. 5.28c).

5.3.3 Effect of fabrication conditions

5.3.3.1 Thickness ratio between Al and Si layer

It was found out that the thickness ratio of the Al and Si sublayer plays a pronounced role on the morphology of the Si layer after the complete procedure. The results obtained by annealing a 1500-nm Al/1500 nm a-Si bilayer (i.e. Al/Si thickness ratio of 1:1) under the same conditions is shown in Fig. 5.30. Unlike the specimen with an Al/Si thickness ratio of 1:10, in this case there is much less intermixing between Al and Si (Fig. 5.29b). Most of the Al remained at the top of the specimen after annealing. After etching off the Al selectively with alkali solution, the morphology of the Si was examined.
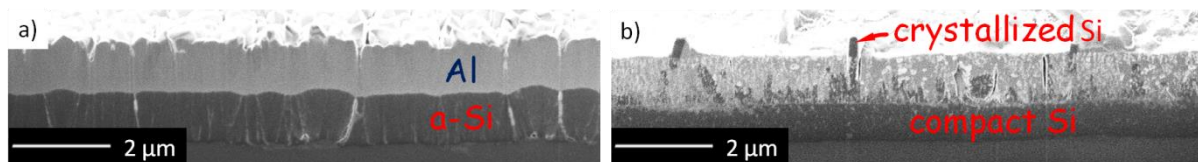
Fig. 5.29   **Cross-sectional FIB images of microstructure evolution in the sample with a ratio between Si and Al 1:1 in different fabrication stages: a) before annealing; b) after annealing but without etching.**

While the lower Si layer is still compact, the upper part of the Si layer has a very rough structure. Many thin-sheet-shaped Si structure stand irregularly on the top (Fig. 5.30a). Under these thin Si sheets, a porous Si layer appears. The lowest part of the specimen is a compact Si layer with a thickness of about 1 μm (Fig. 5.30b). Referring to the theoretical predication and experimental results, the critical cracking thickness for Si thin film as anodes of Li batteries is 130 nm. [38-40] The produced values are above this limit.
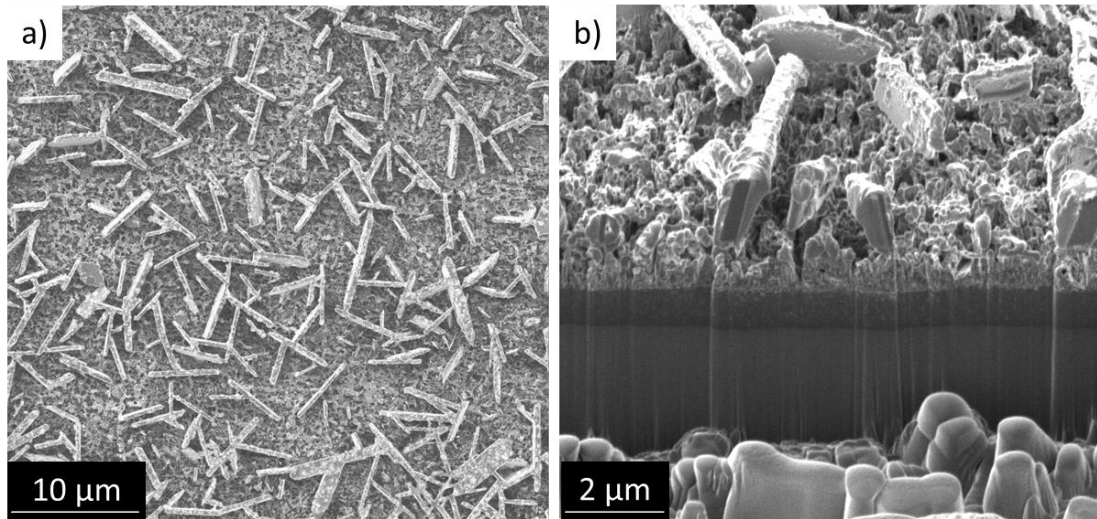
Fig. 5.30   **Morphology of the sample with the same thickness between Si and Al layer, which was annealed at 600 °C and etched with NaOH solution: a) top view, b) cross-section.**

5.3.3.2   Annealing conditions

This nano-columnar porous structure depends sensitively on the annealing temperatures and time. The insufficient annealing results in little layer exchange. Consequently, the stress gradient was not large enough to remove the top PC-Si layer with distilled water (Fig. 5.31a). The porous structure is clearly observed, but only appears at the upper part of original a-Si layer (Fig. 5.31a). In the lower sublayer no nano-columns from Si is built up (Fig. 5.31b and c).
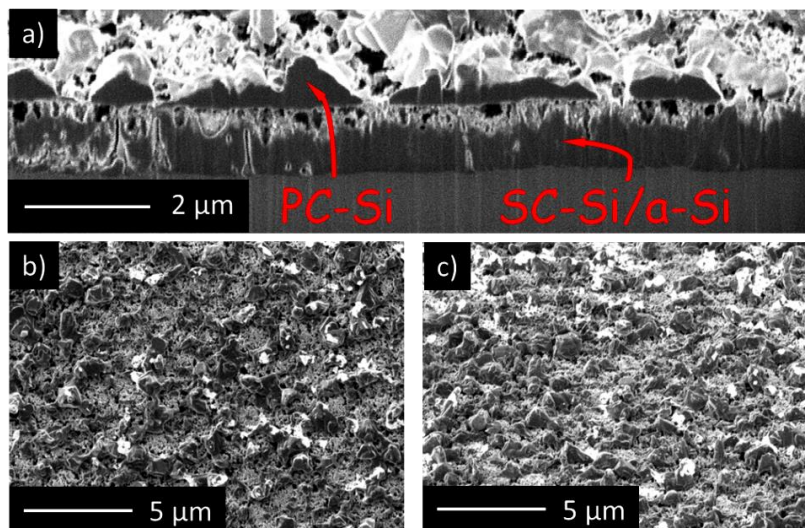
Fig. 5.31   **a) Cross-sectional FIB image of mixture of PC-Si (top) and SC/a-Si (below) prepared with insufficient annealing time (at 450°C for 10 min); b) Surface SEM image of a/a-Si mixture (10 min at 450°C) and c) the corresponding SEM image with 45°C tilt.**
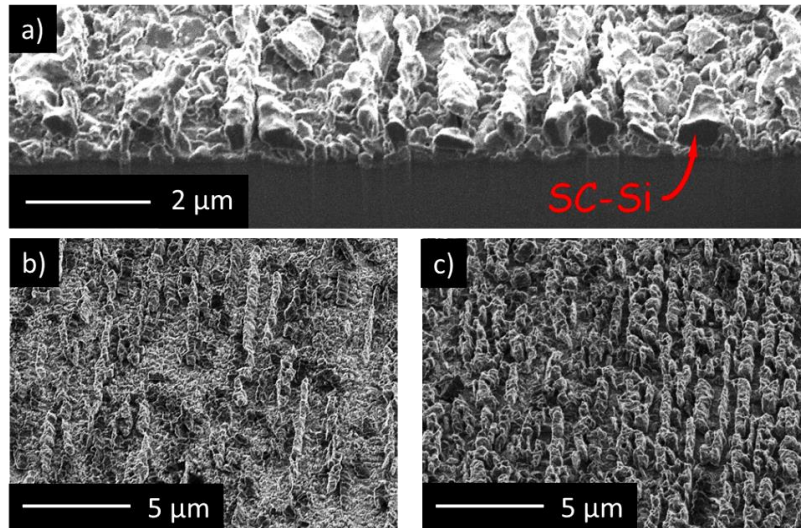
Fig. 5.32   a) Cross-sectional FIB image of SC-Si thick film prepared with overly long annealing (1.5 h at 450°C); b) Surface SEM image of SC-Si thick film (1.5 h at 450°C) and c) the corresponding SEM image with 45°C tilt

Fig. 5.32 shows the morphology of the porous Si film, which was overlong heated. When the sample was overlong heated, the segregated Al diffused towards the interface between lower Si sublayer and substrate. This can weaken the adhesion of the Si nano-columns with substrates. Once the Al is etched, the Si columns would separate from the substrates. On the other hand, the overly intermixing of Al and Si, the distance between Si nano-columns is increased (Fig. 5.32a). Thereby, the overlong annealing leads to a sparse distribution of Si columns (Fig. 5.32b and c).
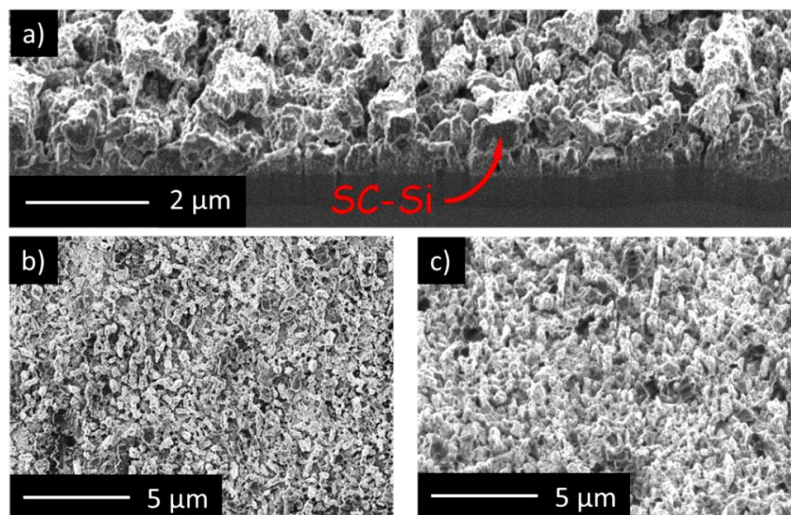
Fig. 5.33   a) Cross-sectional FIB image of SC-Si thick film prepared with overheated annealing (500°C for 30 min); b) Surface SEM image of SC-Si thick film (500°C for 30 min) and c) the corresponding SEM image with 45°C tilt.

Annealing at too high temperatures causes the disappearance of a well-defined morphology of Si nano-columns (Fig. 5.33). An irregular porous structure is formed, which is ascribed to the formation of the more nuclei and smaller Si grains at the higher temperature

Due to the not well formed nano-structure the contact between the Si layer and substrate would be quickly destroyed by material fatigue, which is caused from volume changing during the lithiation and delithiation. Consequently, the charge capacity degrades very quickly during the electrochemical testing (Fig. 5.34).
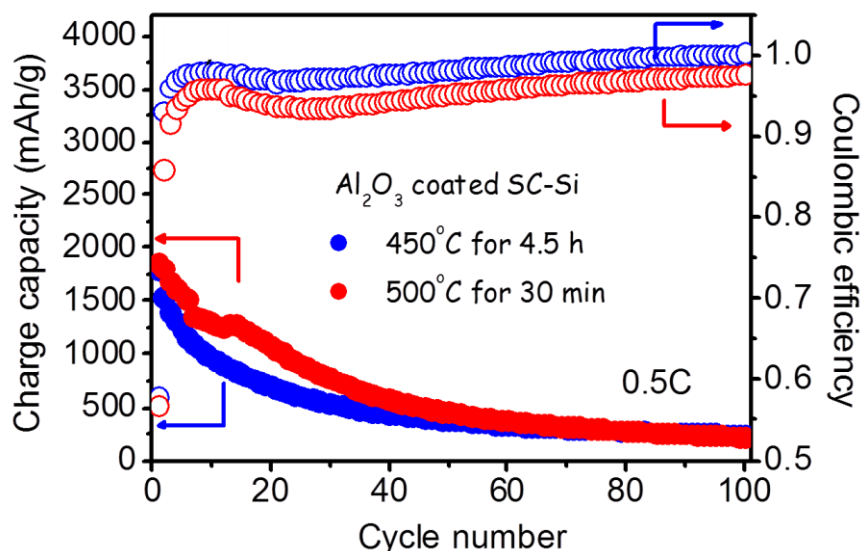
Fig. 5.34   **Electrochemical performance of the samples, which were annealed respectively at 450 °C for 4.5 h and at 500 °C for 30 min. The cycling performance of both samples were tested with 0.5 C charge and discharge velocity. Within the first 100 cycles, the charge capacity faded very quickly. After 100 cycles the charge capacity was almost just 10 % from the maximal capacity at the beginning.**

5.4 Conclusion

The diffusion mechanisms of Si in a nanocrystalline Al layer vary with the annealing temperatures and the Al grain sizes. In consequence, the Si layer is induced to crystallize into different morphologies.

At low temperatures, the Si 'free' atoms preferred to diffuse along the triple junctions of the Al grains, while the grain boundary diffusion at this temperature is 'frozen'. Thermodynamically, the crystallization of Si in triple junctions of Al grains can occur at lower temperatures compared to the conventional crystallization of Si in the Al grain boundaries. With this crystallization mechanism the nano-sized thin 3D frameworks of c-Si were developed on the surface. With a further increase of the annealing temperature, the grain boundary diffusion becomes dominant. Annealed at intermediate temperatures, which is near to the eutectic temper-

ature, Si diffuses practically in the Al grain boundaries. Thus, a corrugated Si film can be developed.

Above the eutectic temperature but still below the crystallization temperature of the pure amorphous Si, a thin Al layer can still induce the crystallization of Si. Different to the specimens annealed below the eutectic temperature, many nano-sized Al-rich precipitate droplets are formed in the bulk crystallized Si layer during this annealing. In addition, the Al layer to induce crystallization of Si needs to be much thinner than the Si layer. After the etching of the Al-rich droplets a 3D nano-porous c-Si frameworks structure is formed.

Due to the different diffusion mechanisms of Si in Al layer, the annealing conditions (e.g. annealing temperatures and annealing time) and the thickness ratios between Si and Al layer must be optimized to earn the suitable porous Si film.

The deposited Al layer can not only induce the crystallization of the Si layer at the lower temperature but also bring a several nanometres thick conformal oxide layer on the surface of the Si layer after etching with the alkali solution. This oxide layer can improve the columbic efficiency of the Si layer. Compared to the conventional fabrication of the nanoscale thick conformal oxide layer on the Si layer, atomic layer deposition (ALD process), this process may be a convenient and economical method.

These oxide layer coated Si porous films are suitable for the application as anode materials of the Li ion battery, e.g. the galvanic performance of this porous Si layer annealed at 450 °C is very outstanding. With 0.5 C charge rate a highly satisfactory retention of capacity as large as 1650 mAh/g is still achievable during not less than 500 cycles. The coulombic efficiency stays nearly 100%.

Chapter 6

Al-induced Crystallization of Al/Ge/Si Trilayers

The fundamentals of the Al-induced crystallization of pure amorphous Si or Ge layers are researched since the last century. Due to the difference on the thermodynamic fundamentals, Al induces the different crystallization behaviors of Si and Ge (see chapter Chapter 2). In this chapter, an amorphous Ge layer is introduced between the crystalline Al and amorphous Si layer to investigate the influence of this amorphous Ge layer to the crystallization behavior of the Si layer.

6.1 Fabrication

- **Substrate preparation**

Pure Titanium foils (99.6%, Goodfellow), Herasil 102 Glass and MgO (001) single crystal are used as substrates for growing Si/Ge/Al trilayers. The substrates were cleaned with ethanol in an ultrasonic bath to remove organic contaminants from the surface. Subsequently, they were dried with the flow Ar gas.

- **Layer Deposition**

The Si, Ge and Al targets were mounted in a high-vacuum multi-target DC sputtering system. After reaching a background vacuum pressure less than 1×10^{-7} mbar, the substrates were cleaned with Ar^+ ions for 1 min. Then a Al layer with a thickness of 750 nm (or 1500 nm) was deposited by using a sputtering power of 200 W in an Ar atmosphere of 5.9×10^{-3} mbar, followed by deposition of a Ge layer with different thicknesses (from 5 nm to 150 nm) at a power of 100 W under the same Ar pressure. Finally, a Si layer which varies from 750 nm to 1350 nm was deposited with the same sputtering power of 100 W. The whole sputtering process was operated at room temperature during the whole layer growth.
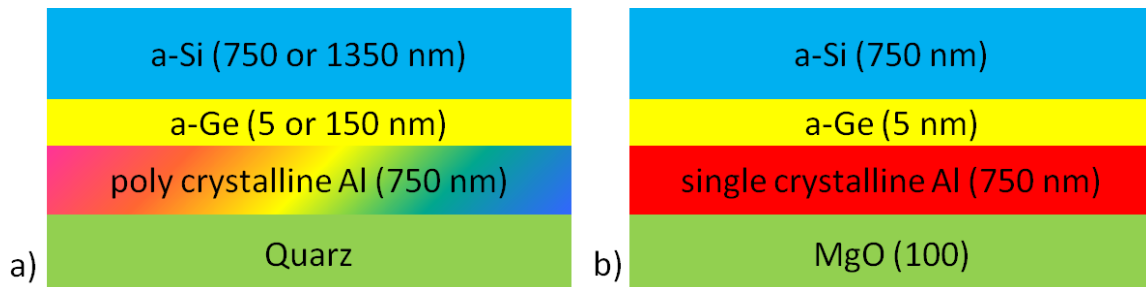
Fig. 6.1   **Structure construction of Al-Ge-Si trilayer system: a) amorphous semiconductor bilayer Ge/Si deposited on a single crystalline Al layer; b) amorphous semiconductor bilayer Ge/Si deposited on a poly crystalline Al layer as a reference sample**

- **Post Treatment**

To investigate the crystallization behavior of the amorphous semiconductors in the Al/Ge/Si trilayer system, the deposited Si/Ge/Al samples were then annealed in a vacuum oven at 400 °C for different time which varies from 5 to 60 minutes.

6.2 Results

6.2.1 Crystallographic analysis of poly and single crystalline Al layers

Al layer deposited on glass substrate shows a polycrystalline microstructure from the EBSD mapping. The crystallographic characters of the Al layer can be investigated graphically (Fig. 6.2a). The average grain size is 350 nm. In contrast, there are no grain boundaries in Al layer deposited on MgO (001) substrates. In this case, a single-crystalline Al layer is formed and orientated in (100) direction (Fig. 6.2b).
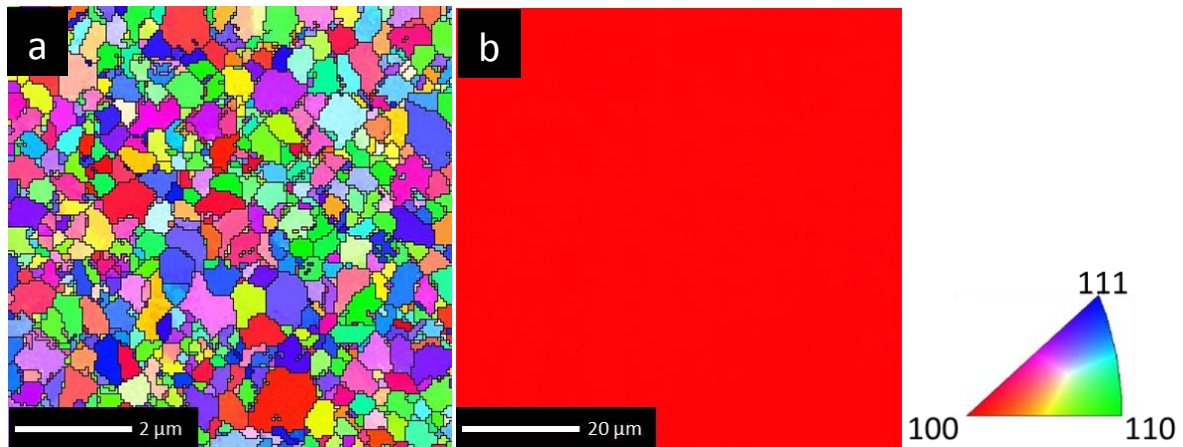
Fig. 6.2   Orientation mapping of Al layer on different substrates: a) poly-crystalline Al on MgO (001) substrate; b) single-crystalline Al on glass substrate.

6.2.2 Crystallization behavior of c-Al/a-Si/a-Ge trilayers

On the Al layers (750 nm) with different microstructures in dependence on the substrates (section 6.2.1), the Si (750 nm))/Ge (5 nm) bilayer was deposited. After annealing at 400 °C for 10 minutes, Al and Si intermixed in both samples (Fig. 6.3a and d). Unlike the Si/Al bilayer system, Al grain boundaries are not a necessary prerequisite for the crystallization of amorphous Si in a c-Al/a-Ge/a-Si trilayer system. The kinetics of the crystallization of Si layer can be evidenced by the cross-sectional images of the further annealing in both samples (induced by a poly-crystalline Al layer: Fig. 6.3a; induced by a single-crystalline Al layer). The crystallization kinetics in both specimens is very same.
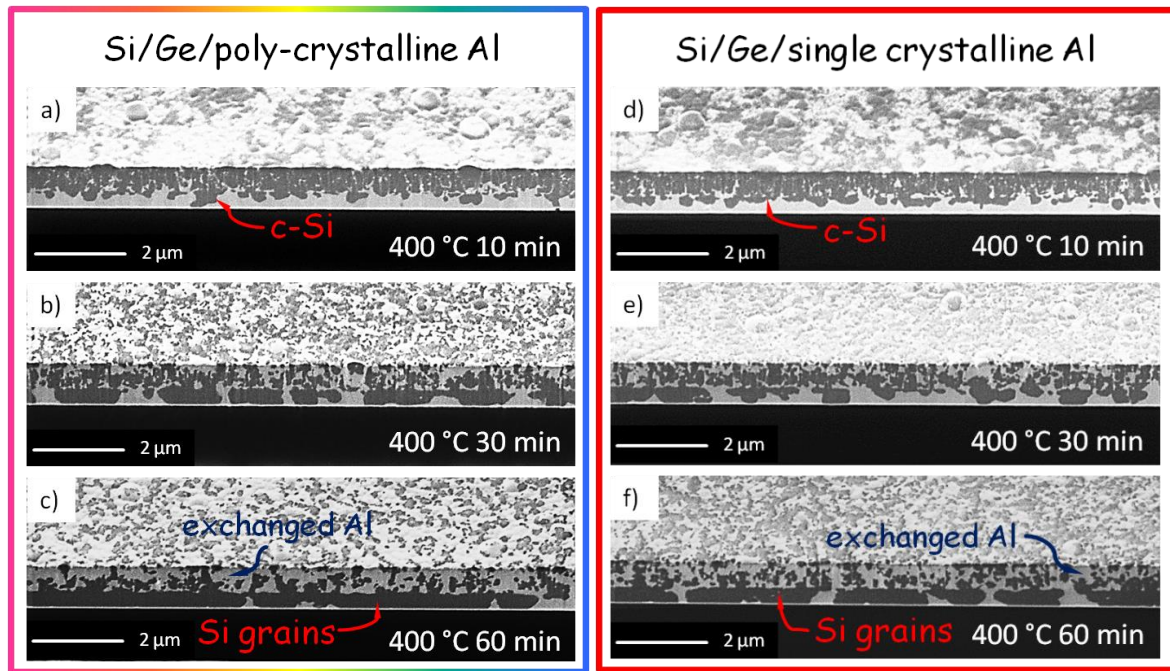
Fig. 6.3   **Comparison of crystallization behaviors of Si (750 nm)/Ge (5 nm)/Al (750 nm) trilayer system on different substrates: a), b) and c) on the glass substrate with poly crystalline Al layer; d), e) and f) on the MgO (001) substrate with single crystalline Al layer (bright phase: Al, dark phase: Si).**

On the Ti foils, a converse a-Si/a-Ge/c-Al trilayer system was deposited (Fig. 6.4a). To further investigate the crystallization process in c-Al/a-Ge/a-Si trilayers, a Ge layer was deposited with a larger thickness of 150 nm (bright phase in Fig. 6.4a). The cross-sections of the sample annealed at 400 °C with the increased annealing time are imaged with the aid of FIB (Fig. 6.4 b to f). At the initial state (after 5 minutes), amorphous Ge crystallizes at the interface between Al and Ge layer (bright phase in Fig. 6.4b). *Z. M. Wang* et al. constructed a thermodynamic model, which can explain this process. [50] Subsequently, Si diffuses into the interface between Al and crystallized Ge and crystallizes there (dark phase in Fig. 6.4c). From Fig. 6.4d to f, it seems that Si crystallizes continuously on the pre-crystallized phase. During the crystallization of Ge/Si bilayers the Al atoms diffuse more and more downwards into the original amorphous Ge/Si bilayers (bright phase in Fig. 6.4c, d, e and f).
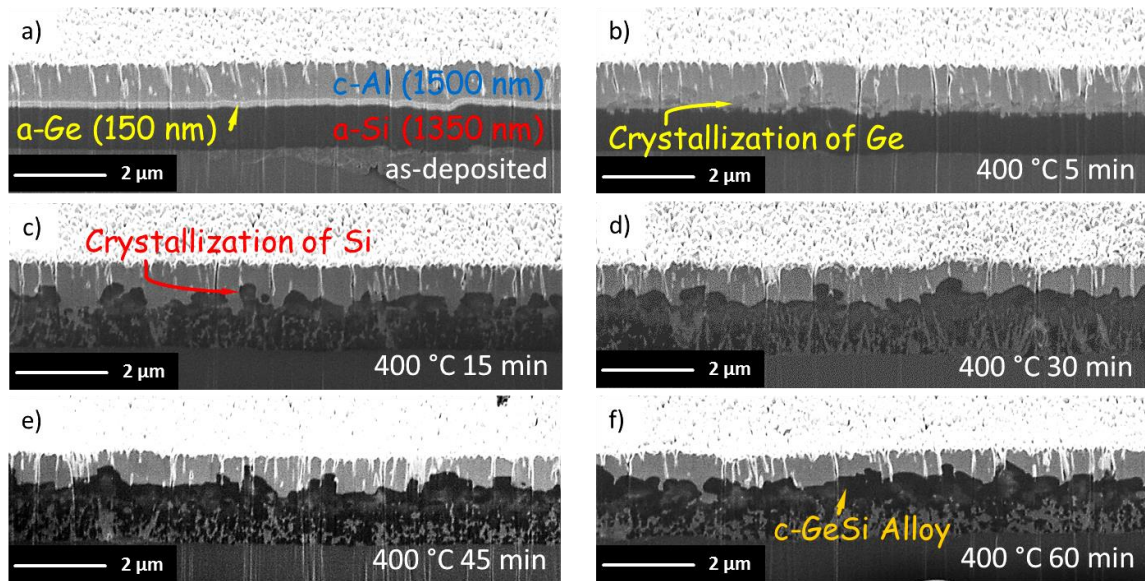
Fig. 6.4 **Crystallization prozess of Si (1350 nm)/Ge (150 nm)/Al (1500 nm) trilayer system on Ti substrate (bright phase: Ge; grey phase: Al; dark phase: Si): a) Ge layer crystallized first; b) Then Si crystallized epitactically on the crystalline Ge in the interface between Ge and Al. c) Later the c-Si grew with the time, mixed with Ge and formed a Ge/Si alloy in the upper layer. Al intermixed simultaneously into the original Si layer and formed porous Si frameworks.**

The XRD spectrum is a complementary way to investigate the crystallization process of the amorphous Ge/Si bilayers (Fig. 6.5). Due to the amorphous structure of Ge and Si in the as-deposited sample, neither the Ge nor the Si diffraction peaks are detected (green curve in Fig. 6.5). The detected peaks of this sample originate from the Ti foils. Annealing at 400 °C for 5 minutes, the crystallization of Ge layer is found as indicated by the emergence of Ge diffractions peaks (red curve in Fig. 6.5). With further annealing time the original Ge diffraction peaks move towards the Si diffraction peak positions. This demonstrates the crystallization of the Si above the crystallized Ge und may lead to the formation of a crystalline Si_xGe_{1-x} alloy.
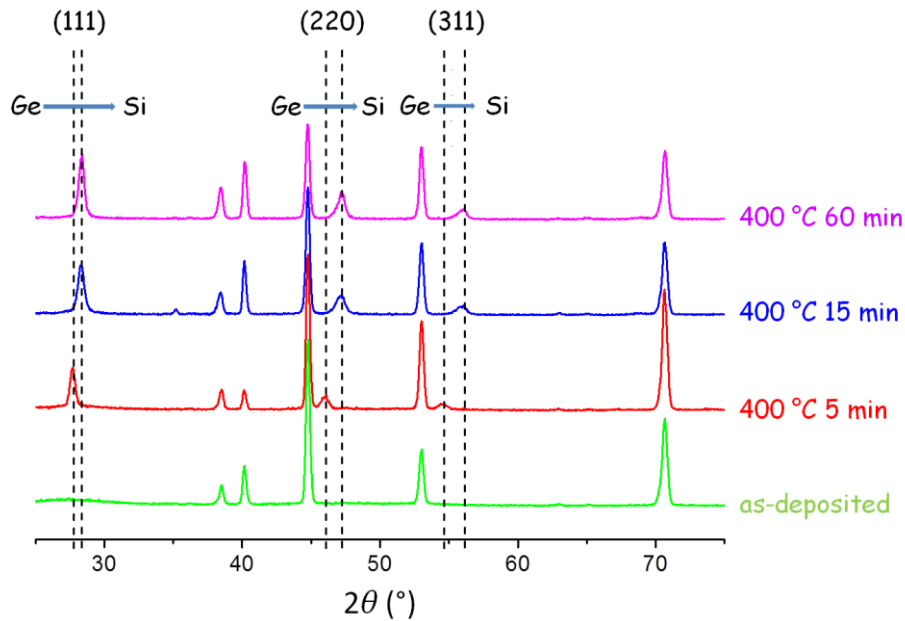
Fig. 6.5   XRD spectra on Si (1350 nm)/Ge (150 nm)/Al (1500 nm) trilayer system on Ti substrate: after
5 minutes the Ge layer crystallizes first (see Ge peaks in red curve). It conforms to the ob-
served FIB images (Fig. 6.4). Later the Si layer crystallizes continuously on the c-Ge and alloys
with Ge. Therefore the Ge peaks shift to the higher angles, which correspond to the expected
Si_xGe_{1-x} alloy.

After the selective etching of Al on the annealed sample with alkali solution, the surface turns
rough (Fig. 6.6). Many crystalline columns with several hundred nanometers stand vertically
to the surface. The EDX measurement indicates that the crystallized phase is a Si_xGe_{1-x} alloy,
which is consistent with the XRD results (Fig. 6.6). According to the element mapping, Ge
and Si are distributed homogeneously.
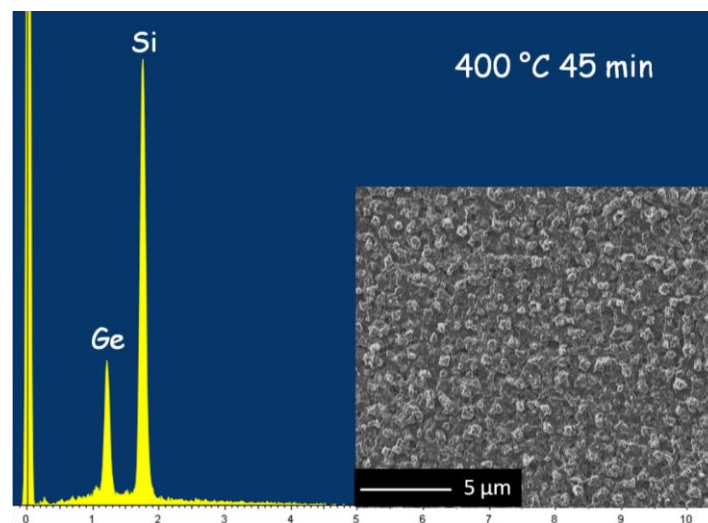
Fig. 6.6   EDX analysis of the chemical component on the surface of the sample annealed at 400 °C for
45 min, which was etched with alkali solution.

6.3 Discussion

The proposed steps of the crystallization of the Si/Ge/Al trilayer system are sketched in Fig. 6.7. At the initial stage the a-Ge layer crystallizes at the interface of the original a-Ge and Al layer. Then the 'free' Si atoms diffuse along the interface between crystallized Ge and Al and wet the interface. Up to the critical thickness of the crystallization the wetting Si layer crystallizes at the original c-Ge/c-Al interface and forms the crystalline Si_xGe_{1-x} alloy. The thermodynamic fundamental for the whole crystallization process of Si layer will be shown in the following sections.
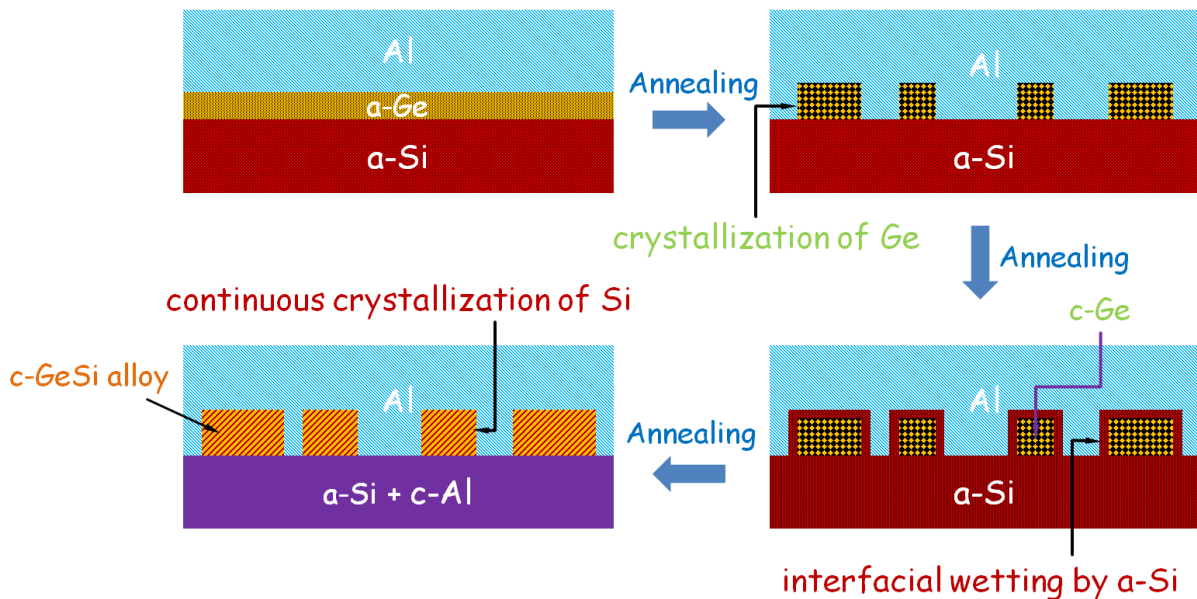
Fig. 6.7 **Crystallization process of Si/Ge/Al trilayer system: Ge crystallizes at the interface between original a-Ge and c-Al. Then the free Si atoms wet the phase interface of c-Ge and c-Al. Si crystallized continuously on the c-Ge nuclei and formed c-Si_xGe_{1-x} alloy.**

6.3.1 Crystallization of Ge

Referring to [50] the mechanism for Al induced crystallization of Ge is thermodynamically calculated (in chapter Chapter 2). The 'free' Ge atoms may wet the original a-Ge/c-Al interface or the original grain boundaries of c-Al layer to reduce the interface energy of the whole Ge/Al bilayer system. Up to the critical thickness for the crystallization of Ge the amorphous Ge crystallizes at the original a-Ge/c-Al interface or in the original grain boundaries of c-Al layer. Although the interface energy between c-Ge/c-Al increases compared to that between a-Ge/c-Al, the crystallization energy of Ge minimizes the Gibbs energy of the whole system.

6.3.2 Wetting of Si

By crystallization of Ge, an interface between c-Ge and c-Al is formed (Fig. 6.8a). Due to the screening effect, the Si atoms on the top of the a-Si layer are free to move. Generally, the interface diffusion is much easier than the volume diffusion.[78] Thermodynamically, only the two newly formed interface a-Si/c-Al and a-Si/c-Ge have totally a lower Gibbs interface energy ($\gamma_{\langle Al \rangle / \{Si\}} + \gamma_{\{Si\}/\langle Ge \rangle}$) than the original Gibbs interface energy of c-Ge/c-Al ($\gamma_{\langle Al \rangle / \langle Si \rangle}$), the 'free' Si atoms will prefer to migrate into the interface between c-Al and c-Ge and form a stable wetting layer of a-Si there (Fig. 6.8a).
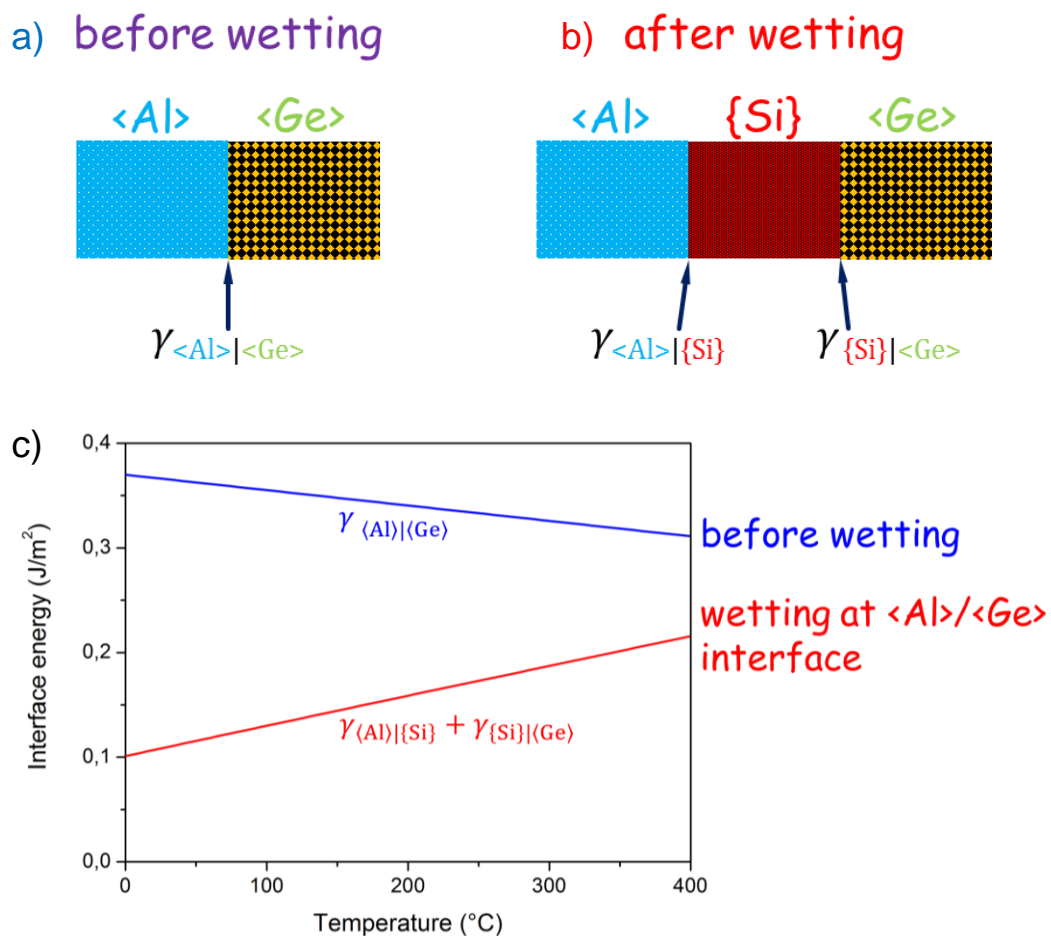
Fig. 6.8   **Instead of c-Si/c-Ge interface before the wetting a), two new interfaces were formed after the wetting with the free Si atoms. They are c-Al/a-Si and a-Si/c-Ge interface b); c) After wetting by free Si atoms, an amorphous interface phase of Ge forms. The total energy of c-Al/a-Si and a-Si/c-Ge interface (red curve) is lower than the c-Si/c-Ge interface energy before the wetting (blue curve).**

According to the Eq. 51, the dependence of the specific interface energy between c-Al/c-Ge ($\gamma_{\langle Al \rangle / \langle Ge \rangle}$) and the annealing temperature (T) can be calculated, which is plotted as a blue curve in Fig. 6.8b. Based on Eq. 25, the specific interface energy between c-Al/a-Si ($\gamma_{\langle Al \rangle / \{Si\}}$)

and a-Si/c-Ge ($\gamma_{\{Si\}/\langle Ge\rangle}$) can be calculated as a function of temperature. The function of the sum of both specific interface energies between the crystalline and amorphous phase is represented as a red curve in Fig. 6.8b. Comparing the calculated energies of the different interfaces, the totally interface energy between the crystalline and amorphous phase ($\gamma_{\langle Al\rangle/\{Si\}} + \gamma_{\{Si\}/\langle Ge\rangle}$) is lower. Thus, the wetting of the c-Ge/c-Al interface by the 'free' Si atoms is preferred thermodynamically.

6.3.3 Continuous Crystallization of Si

Similar to the case of Si/Al bilayer system, the amorphous Si wetting layer between c-Ge and c-Al (red phase in Fig. 6.8a) can crystallize, once its thickness exceeds the critical crystallization thickness of Si. There are two different possibilities for the crystallization of the Si layer at the initial stage: the continuous crystallization of Si based on the crystallized Ge or the new nucleation of Si between the c-Al and c-Ge (Fig. 6.9a).

When Si crystallizes continuously based on the preexisting c-Ge grains, a new interface between c-Al and c-Si$_x$Ge$_{1-x}$ alloy is formed. Si and Ge have the same structure (diamond structure) and relatively similar lattice constants (Ge: 5,66 Å, [51] Si: 5.43 Å, [51] the relative difference is about 4 %). For these reasons a continuous series of solid solutions can be formed between them.[87] Consequently, the specific interface energy between Al and Si$_x$Ge$_{1-x}$ ($\gamma_{\langle Al\rangle/\langle Si_xGe_{1-x}\rangle}$) alloys can be approximated by:

$$\gamma_{\langle Al\rangle/\langle Si_xGe_{1-x}\rangle} = x_{Ge} \cdot \gamma_{\langle Al\rangle/\langle Ge\rangle} + (1 - x_{Ge}) \cdot \gamma_{\langle Al\rangle/\langle Si\rangle} \qquad Eq.\,26$$

Where x_{Ge} stands for the concentration of Ge in the Si$_x$Ge$_{1-x}$ alloy. At the initial stage, the concentration of Si is almost zero. The specific interface energy at this initial state ($\gamma_{\langle Al\rangle/\langle Si_xGe_{1-x}\rangle}(c_{Si} \to 0)$), which depends on the temperature T, is plotted in Fig. 6.9b as a green line.

There is the alternative possibility that Si crystallizes directly between the crystalline Al and crystallized Ge grain and forms a new nucleus of pure Si (Fig. 6.9). Instead of the former $\langle Al\rangle/\{Si\}$ and $\{Si\}/\langle Ge\rangle$ interfaces, two interfaces $\langle Al\rangle/\langle Si\rangle$ and $\langle Si\rangle/\langle Ge\rangle$ are newly formed. The respective specific interface energies between the crystalline phases can be calculated referring to Eq. 51. The pink curve in Fig. 6.9b shows the sum of the specific interface energy from the newly formed interfaces as a function of the annealing temperature.
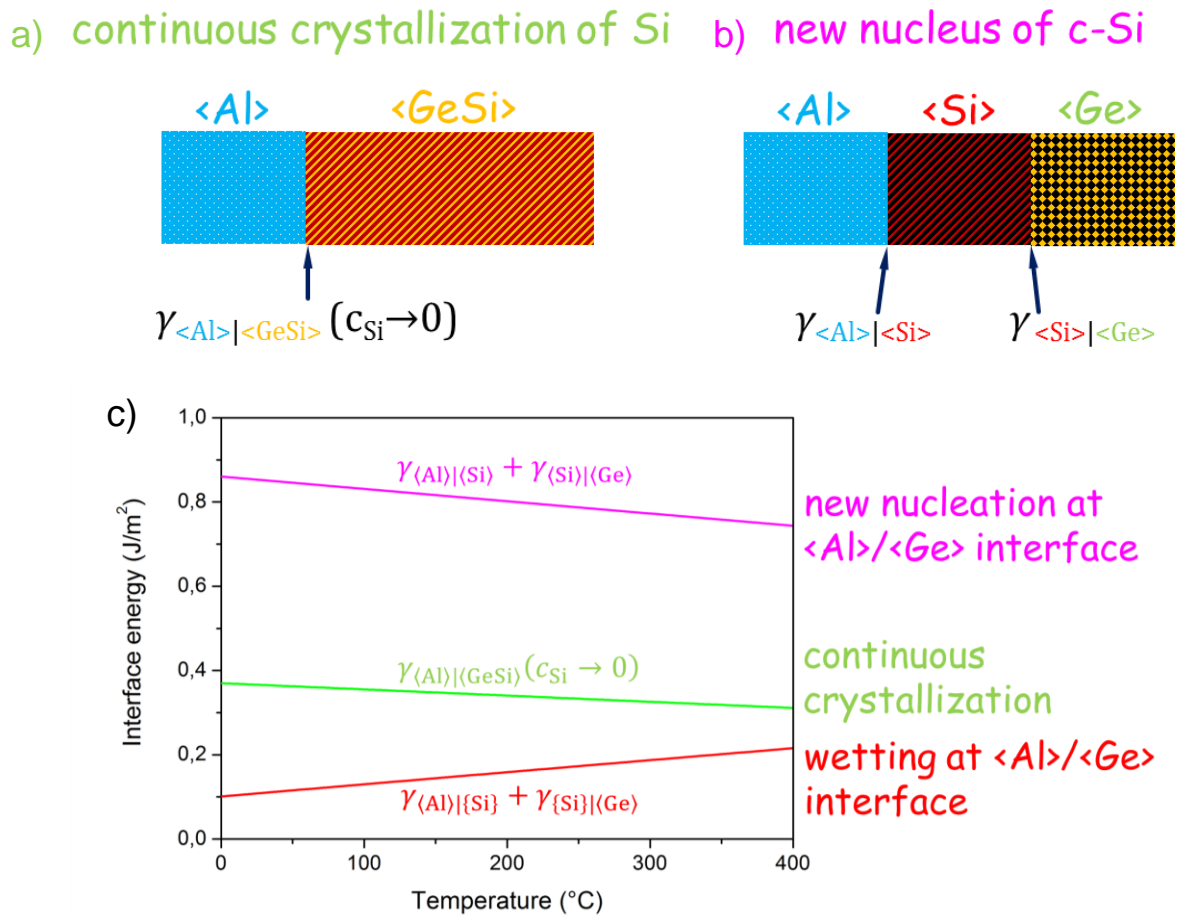
Fig. 6.9   **Two different crystallization possibilities of Si layer: a) continuous crystallization on the crystalline Ge, which results in a new formed interface between c-Al and c-Si_xGe$_{1-x}$ alloy; b) new nucleus of Si between the c-Al and c-Ge. Thereby it formed two new interfaces: c-Al/c-Si interface and c-Si/c-Ge interface; c) The total interface energy after continuous crystallization on c-Ge (green line) is much lower than the new nucleus of c-Si at the c-Ge/c-Al interface (pink line). The red line shows the total interface energy after the wetting with the free Si atoms.**

Compared to the new nucleation of Si, the specific interface energy of the continuous crystallization of Si based on Ge grains is much lower. Although the total specific interface energy of both crystallization possibilities is higher than that of the interface with the wetted a-Si, the total Gibbs energy of the whole system can be reduced by the crystallization of Si, if a critical thickness is exceeded.
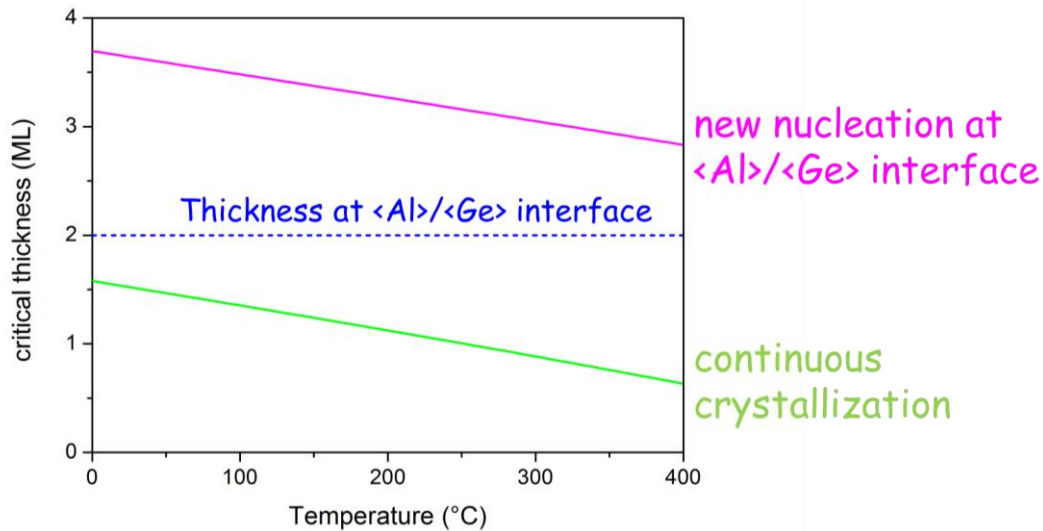
Fig. 6.10   **The critical crystallization thickness of lateral crystallization (pink curve) is lower than two mono layers, which are the thickness at the interface. There are more than two mono layer spaces needed for the new nucleus of c-Si (green curve). Thereby Si preferred to crystallize continuously on the c-Ge.**

The prerequisite for the low-temperature crystallization of Si is that the critical crystallization thickness must be smaller than 2 monolayers (ML).[50] Analog to the case of the bilayer system, the critical thickness of the Si layer based on the Ge crystallites can be calculated in dependence on the temperature. Fig. 6.10 shows the plot of the critical crystallization thickness (in ML) vs. the annealing temperature of both crystallization possibilities. The pink curve indicates the critical thickness of the new Si-nucleus, which is needed at the different annealing temperatures. Up to 400 °C it is still higher than 2 ML. Consequently, Si cannot nucleate at the interface between c-Al and c-Ge. In contrast, the continuous crystallization of Si based on the preexisting c-Ge grains needs less space, i.e. less than 2 ML (green curve in Fig. 6.10). Hence, Si preferred to crystallize laterally on the c-Ge and form the Si_xGe_{1-x} alloys. This thermodynamic model confirms the formation of the Si_xGe_{1-x} alloys from the XRD results (Fig. 6.5).

6.4 Conclusion

Compared to the conventional Al induced crystallization in Al-Si bilayer system, the presence of an amorphous Ge intralayer affects the crystallization behavior of the amorphous Si layer significantly. Al grain boundaries are not necessary any more. At first, the amorphous Ge layer may crystallize at the interface to the Al layer or also at the Al grain boundaries, if they exist. Then the 'free' Si atoms prefer to wet the interface between the c-Ge and c-Al, to reduce the total interface energy of the system. Due to the same lattice structure and small dif-

ference of the lattice constants of Ge and Si, the diffused a-Si may crystallize on the Ge seeds, grow continuously and form the Si_xGe_{1-x} alloys. The Al induced crystallization temperature of Ge is much lower than that of Si. Therefore, this process leads to a reduction of the crystallization temperature of a-Si.

Chapter 7

Summary

The Al-induced crystallization of amorphous semiconductors is a diffusion-controlled process. By varying the characteristics of the Al layer or the annealing condition in Al/Si bilayer system, the diffusion paths of the Si atoms in the Al layer are changed. A porous Al layer induced the crystallization of Si into large grains. Such large-grained Si layers can be applied as the seed layers for the thin film solar cells. By interrupting purposely the annealing of the Al/Si bilayers, porous Si layers can be developed. The c-Si layers with such a porous structure can be applied as the anode materials of Li ion batteries. In the c-Al/a-Ge/a-Si trilayer system, the introduction of an amorphous Ge layer changes the crystallization behavior of the Si layer. Different to the crystallization behavior of Si in the Al/Si bilayer system, the Al grain boundaries are not needed in such c-Al/a-Ge/a-Si trilayer system. The amorphous Si crystallizes continuously on the pre-crystallized Ge seeds as induced by the Al layer. Finally, crystalline Si_xGe_{1-x} alloys can be formed.

7.1 Large-grained Si induced by porous Al layer

By applying a bias voltage during the sputtering, a porous crystalline Al layer can be developed. In this porous Al layer, the Al grain boundaries are contaminated by, e.g. O. Therefore, the diffusion of the 'free' Si atoms in the Al grain boundaries is retarded. Different to the grain boundary diffusion of Si in the compact Al layer, a collective diffusion process of Si will be activated at a certain high temperature in this case, e.g. retarded grain boundary diffusion, pipe diffusion, volume diffusion.. This whole diffusion process leads to a lower nucleation density and crystallization velocity of amorphous Si.

An Al oxide buffer layer between the initial Si and porous Al layer can enhance the tendency to form a crystalline Si layer with larger grains. With this method, the average grain size of Si can exceed 20 μm. In addition, with increasing grain size of the crystallized Si layer, more Si grains orientate in (100) direction.

In these large-grained Si layers most of the grain boundaries are CSL Σ3 boundaries. The CSL Σ3 boundaries are formed to reduce the internal stress which originates from the asymmetric intermixing between Si and Al. Fortunately, the recombination activity between conducting electrons and holes of these twin boundaries is very low. Therefore, this fabrication method is presumably suitable to serve as the seed layer of thin film solar cells.

7.2 Porous Si layer by Al-induced crystallization

By purposely interrupting the post treatment of the a-Si/nanocrystalline Al bilayers and selectively etching of Al with alkali solution, a porous crystalline Si layer can be formed. In the nanocrystalline Al layers, there is a very high density of triple junctions and grain boundaries which provide the fast diffusion paths for Si atoms. The diffusion of free 'Si' atoms in Al layer may be a collective behavior of different diffusion types (pipe diffusion, volume diffusion, grain boundary diffusion and triple junction diffusion), which depends on the annealing temperature.

At relatively low temperatures (i.e. largely below the eutectic point), the crystallization of Si in the Al triple junctions is thermodynamically more favorable than that in the Al grain boundaries. Kinetically, the Si 'free' atoms can diffuse in the triple junctions of the Al layer, while the diffusion of Si into the Al grain boundaries are 'frozen' at this temperature. Due to this pipe-like diffusion path of Si in Al layer, 3D nanoscale c-Si frameworks can be developed.

By increasing the temperature, the diffusion of Si in the Al grain boundaries will be activated. At the intermediate temperatures (i.e. slightly below the eutectic point), Si atoms diffuse practically in the Al grain boundaries. Due to intermixing between the original a-Si and c-Al layers, a corrugated Si layer can be developed after the selectively etching of Al.

Above the eutectic temperature but still below the crystallization temperature of the pure a-Si, many nano-sized Al-rich droplets are formed throughout the Si layer. After fast cooling, these droplets solidify as a nonequilibrium phase and can be etched away with the alkali solution. Finally, porous Si frameworks are formed based on the Al-Si eutectic reaction.

In addition, Al can not only induce the crystallization of amorphous Si but also bring a functional conformal oxide coating with several nanometers on the porous Si layers upon etching. Since this oxide layer can prevent the formation of SEI phases, the coloumbic efficiency of these Si porous layers is near 100%.

These prepared oxide-coated porous Si layers are tested as the work electrodes of Li-ion battery. After several hundred cycles, their capacities stay still about 70% of that at the beginning. Therefore, with optimal annealing conditions and thicknesses of Al layer, this process may be applied as a potential method for the production of porous Si as anode material of lithium ion batteries.

7.3 Al-induced crystallization of amorphous Si/Ge bilayers

Using a crystallized Ge layer induced by Al layer, the crystallization conditions of the a-Si layer can be changed. In contrast to the crystallization of Si in the Al grain boundaries in the Al/Si bilayer system, the Al grain boundaries are not needed anymore in this Al/Ge/Si trilayer system. At first, a-Ge crystallizes at the interface to the Al layer. Thermodynamically, to reduce the interface energy of the total system, the 'free' Si atoms prefer to diffuse into the interface between the crystallized Ge and the Al grains and form a wetting layer of Si. As a consequence of the same lattice structure and similar lattice parameters between Ge and Si, a-Si can crystallize continuously on the c-Ge seeds and grow continuously. The complete miscibility of Si and Ge leads to the formation of the c- Si_xGe_{1-x} alloys. Due to the crystallization of the Ge layer as seeds, the crystallization temperature of the a-Si layer can be reduced. As a result, it is possible to fabricate a c-Si layer on the substrate with favorable functionalities but lower maximum processing temperature, e.g. the conductive polymer. By varying the initial Si/Ge thickness ratio composition of the Si_xGe_{1-x} alloys the morphological structure can be also be changed. In addition, due to the alloying with Ge, the newly formed layers could be also suitable for the anode material of the Na ion batteries.

.

Appendix

A1   Calculations of the crystallization energies

Generally, above the crystallization temperature T_c a pure amorphous phase {A} can transit to its crystalline phase ⟨A⟩. The Gibbs energy difference between the amorphous and crystalline phase is named crystallization energy ($\Delta G_{\langle A \rangle - \{A\}}^{cryst}$). The crystallization energy related to the temperature T can be determined by the following equations:[1]

$$\Delta G_{\langle A \rangle - \{A\}}^{cryst}(T) = \Delta H_{\langle A \rangle - \{A\}}^{cryst}(T) - T \cdot \Delta S_{\langle A \rangle - \{A\}}^{cryst}(T) \qquad \text{Eq. 27}$$

$$\Delta H_{\langle A \rangle - \{A\}}^{cryst}(T) = \Delta H_{\langle A \rangle - \{A\}}^{cryst}(T_c) + \int_{T_c}^{T} \Delta c_p(T) dT \qquad \text{Eq. 28}$$

$$\Delta S_{\langle A \rangle - \{A\}}^{cryst}(T) = -S_{\{A\}}^{0} + \int_{0}^{T} \frac{\Delta c_p}{T} dT \qquad \text{Eq. 29}$$

Here, $\Delta H_{\langle A \rangle - \{A\}}^{cryst}(T)$ is the crystallization enthalpy, where $\Delta H_{\langle A \rangle - \{A\}}^{cryst}(T_c)$ can be experimentally measured at the crystallization temperature by calorimetric methods, e.g. differential scanning calorimetry (DSC) or differential thermal analysis (DTA). $\Delta S_{\langle A \rangle - \{A\}}^{cryst}(T)$ is the entropy difference between the amorphous and crystalline phase. $\Delta c_p(T)$ is the difference of the specific heat capacity between the crystalline and amorphous phases. $S_{\{A\}}^{0}$ means the residual entropy of the amorphous phase at 0 K.

The parameters for the calculation of the crystallization energies of Si and Ge are listed in Tab. 2:

Tab. 2   Thermodynamic data for Si and Ge

	T_m (K)	T_c (K)	ΔH_c (kJ/mol)	S_a^0 (J/ mol·K)	ΔC_p (J/mol·K)
Ge	1210[88]	750[1]	11.5[89]	1.66[90]	$-0.224 + 4.8 \cdot (T/1210)$[89]
Si	1685[88]	960[1]	11.95[1]	1.66[90]	$-0.224 + 4.8 \cdot (T/1685)$[89]

T_m: Melting point of the crystalline phase

T_c: Crystallization temperature of the amorphous phase

ΔH_c: Crystallization enthalpy of the amorphous phase at T_c

S_a^0:   Residual entropy of the amorphous phase (estimated in Ref. [90])

ΔC_p: Specific heat capacity between the amorphous and crystalline phase

A2   Calculations of the surface energies

The molar surface Gibbs energy of a crystalline solid phase ($G_{\langle A \rangle}^{S}$) (here, S stands for surface) related to the temperature T can be described in terms of the molar surface enthalpy ($H_{\langle A \rangle}^{S}$) and the molar surface entropy ($S_{\langle A \rangle}^{S}$):[66]

$$G_{\langle A \rangle}^{S} = H_{\langle A \rangle}^{S} - T \cdot S_{\langle A \rangle}^{S} \qquad \text{Eq. 30}$$

Analog to the crystalline phase, the molar surface Gibbs energy of an amorphous phase ($G_{\{A\}}^{S}$) can be expressed by:[66]

$$G_{\{A\}}^{S} = H_{\{A\}}^{S} - T \cdot S_{\{A\}}^{S} \qquad \text{Eq. 31}$$

To calculate the surface energy per unit surface area, the contact surface area of the molar surface atoms O_i (i: $\langle A \rangle$ for crystalline phase A; $\{A\}$ for amorphous phase A) is needed. *F. R. de Boer* et al. suggested that the contact surface area of the molar surface atoms can be expressed by the following equations:[78]

$$O_{\langle A \rangle} = f_{\langle A \rangle} \cdot C_0 \cdot V_{\langle A \rangle}^{2/3} \qquad \text{Eq. 32}$$

$$O_{\{A\}} = f_{\{A\}} \cdot C_0 \cdot V_{\{A\}}^{2/3} \qquad \text{Eq. 33}$$

Where $V_{\langle A \rangle}$ und $V_{\{A\}}$ represent the molar volumes of the crystalline phase $\langle A \rangle$ and the amorphous phase $\{A\}$. $f_{\langle A \rangle}$ and $f_{\{A\}}$ stand for the average fraction of the surface of an atomic (Wigner-Seitz) cell around each atom of the specimen in contact at the surface with the vapor or vacuum. $f_{\langle A \rangle}$ is equal 0.35 for crystalline phase $\langle A \rangle$,[91] while for amorphous phase $\{A\}$ $f_{\{A\}}$ is $1/3$.[78] The constant C_0 depends on the shape of the atomic cell.. According to [78], it can be taken by the average value and consequently can be calculated:

$$C_0 = 5.42 \cdot N_{Av}^{1/3} = 4.5 \times 10^8 \text{ mol}^{1/3} \qquad \text{Eq. 34}$$

where N_{Av} stands for the Avogadro number.

Thus, the corresponding specific surface energy of the crystalline phase ($\gamma_{\langle A \rangle}^{S}(T)$) and the amorphous phase ($\gamma_{\{A\}}^{S}(T)$) can be determined by:[92]

$$\gamma_{\langle A \rangle}^{S}(T) = \frac{H_{\langle A \rangle}^{S} - T \cdot S_{\langle A \rangle}^{S}}{f_{\langle A \rangle} \cdot C_0 \cdot V_{\langle A \rangle}^{2/3}} \qquad \text{Eq. 35}$$

$$\gamma_{\{A\}}^{S}(T) = \frac{H_{\{A\}}^{S} - T \cdot S_{\{A\}}^{S}}{f_{\{A\}} \cdot C_0 \cdot V_{\{A\}}^{2/3}} \qquad \text{Eq. 36}$$

According to the model from *A. R. Miedema*, the surface entropies of the crystalline ($S_{\langle A \rangle}^{S}$) and amorphous phase ($S_{\{A\}}^{S}$) can be estimated which are in agreement with relevant experimental data:[78, 91, 92]

$$S_{\langle A \rangle}^{S} = 7.72 \frac{J}{mol \cdot K} \qquad Eq.\,37$$

$$S_{\{A\}}^{S} = 7.34 \frac{J}{mol \cdot K} \qquad Eq.\,38$$

With the experimental values of the specific surface energy $\gamma_{\langle A \rangle}^{S}(T_0)$ and $\gamma_{\{A\}}^{S}(T_0)$ at a certain temperature (T_0), the specific surface energy of the crystalline and amorphous phase at any temperature T can be calculated respectively:[50]

$$\gamma_{\langle A \rangle}^{S}(T) = \gamma_{\langle A \rangle}^{S}(T_0) + \frac{(T_0 - T) \cdot S_{\langle A \rangle}^{S}}{f_{\langle A \rangle} \cdot C_0 \cdot V_{\langle A \rangle}^{2/3}} \qquad Eq.\,39$$

$$\gamma_{\{A\}}^{S}(T) = \gamma_{\{A\}}^{S}(T_0) + \frac{(T_0 - T) \cdot S_{\{A\}}^{S}}{f_{\{A\}} \cdot C_0 \cdot V_{\{A\}}^{2/3}} \qquad Eq.\,40$$

The parameters for the calculation of the surface energy of crystalline and amorphous phase Si and Ge are listed in Tab. 3:

Tab. 3 Parameter for the surface energy calculation of different phases ($\langle A \rangle$: crystalline phase A; {A}: amorphous phase A)

	$\langle Ge \rangle$	{Ge}	$\langle Si \rangle$	{Si}	$\langle Al \rangle$
$\gamma^{S}(T_0)$ (J/m^2)	0.97[93]	0.62[94]	1.37[93]	0.87[95]	1.03[93]
T_0 (K)	473	1211	493	1685	500
V_m (m^3/mol)	13.65×10^{-6}	12.97×10^{-6}	12.13×10^{-6}	12.97×10^{-6}	11.10×10^{-6}

$\gamma^{S}(T_0)$:   Experimental surface energy at the Temperature T_0

V_m: Molar volume from Ref. [96]

A3 Calculations of the interface energies between the crystalline and amorphous phases

Similar to the Gibbs interface energy between crystalline phases $\langle A \rangle$ and $\langle B \rangle$ ($G^{\text{interf}}_{\langle A \rangle / \langle B \rangle}$), the Gibbs interface energy between the crystalline phase $\langle A \rangle$ and amorphous phase $\{B\}$ can be contributed by the interfacial enthalpy ($H^{\text{interf}}_{\langle A \rangle / \{B\}}$) and interfacial entropy ($S^{\text{interf}}_{\langle A \rangle / \{B\}}$):[92]

$$G^{\text{interf}}_{\langle A \rangle / \{B\}} = H^{\text{interf}}_{\langle A \rangle / \{B\}} - T \cdot S^{\text{interf}}_{\langle A \rangle / \{B\}} \qquad \text{Eq. 41}$$

The atomic interaction at the interface of crystalline and amorphous (undercooled liquid) phases is assumed to be similar to the case at the interface of crystalline and liquid phases.[92] Thus, the total interface enthalpy contribution ($H^{\text{interf}}_{\langle A \rangle / \{B\}}$) can be estimated:[50]

$$H^{\text{interf}}_{\langle A \rangle / \{B\}} = f_{\{A\}} \cdot \Bigg[H_{\{A\}}(T) - H_{\langle A \rangle}(T)$$

$$+ \frac{\Delta \bar{H}^0_{\{A\} \text{ in } \{B\}} + H_{\{B\}}(T) - H_{\langle B \rangle}(T) + \Delta \bar{H}^0_{\{B\} \text{ in } \{A\}} + H_{\{A\}}(T) - H_{\langle A \rangle}(T)}{2} \Bigg] \quad \text{Eq. 42}$$

where $\Delta \bar{H}^0_{\{A\} \text{ in } \{B\}}$ is the partial enthalpy of dissolution of the amorphous phase $\{A\}$ in the amorphous phase $\{B\}$. The thermodynamic values of the amorphous phase, which is also named undercooled liquid phase, can be given analogously with the value of the liquid phase for the calculation.[92] Consequently, $\Delta \bar{H}^0_{\{A\} \text{ in } \{B\}}$ can be taken from the partial enthalpy of dissolution of liquid phase A in liquid phase B.

F. Sommer assumed that there is no change in lattice vibration between the crystalline and amorphous phase by introducing an interface.[92] However, the configurational entropy of the amorphous phase is reduced at the interface by an ordering effect, due to the nearby crystalline phase.[92] The contribution of the configurational entropy at the interface between amorphous phase and crystalline phase can be expressed referring to [97]:

$$S^{\text{interf}}_{\langle A \rangle / \{B\}} = -0.678 \cdot \text{R} \qquad \text{Eq. 43}$$

Finally, the specific interface energy between crystalline phases $\langle A \rangle$ and amorphous phase $\{B\}$ can be calculated from:

$$\gamma^{\text{interf}}_{\langle A \rangle / \{B\}} = \frac{G^{\text{interf}}_{\langle A \rangle / \{B\}}}{f_{\{A\}} \cdot C_0 \cdot V^{2/3}_{\langle A \rangle - \{B\}}} \qquad \text{Eq. 44}$$

Where $V_{\langle A \rangle - \{B\}}$ stands for the average molar volume of the crystalline phase $\langle A \rangle$ and amorphous phase $\{B\}$.

The parameters for the calculation of the interface energy between the crystalline Al or Si and amorphous Ge are listed in Tab. 4:

Tab. 4   The partial mixing enthalpy between the amorphous phases

A	B	$\Delta H^0_{\{A\} \text{ in } \{B\}}$ (J/mol)	$\Delta H^0_{\{B\} \text{ in } \{A\}}$ (J/mol)
Al	Si	-11340[96]	-11340[96]
Si	Ge	-3000[98]	-20000[98]

A4   Calculations of the interface energies between the crystalline phases

At the interface between the crystalline phases $\langle A \rangle$ and $\langle B \rangle$, the atoms are completely surrounded by atoms. *F. Sommer* has presumed that the Gibbs energy of the $\langle A \rangle / \langle B \rangle$ interface can be contributed from the Gibbs elastic (or misfit) energy ($G_{\langle A \rangle / \langle B \rangle}^{mis}$) and the Gibbs interfacial chemical energy ($G_{\langle A \rangle / \langle B \rangle}^{chem}$):[92]

$$G_{\langle A \rangle / \langle B \rangle}^{interf} = G_{\langle A \rangle / \langle B \rangle}^{mis} + G_{\langle A \rangle / \langle B \rangle}^{chem} \qquad \text{Eq. 45}$$

The Gibbs interfacial elastic (or misfit) energy ($G_{\langle A \rangle / \langle B \rangle}^{mis}$) results from the mismatch at the interface of the lattice sites and orientations of the atomic cells along both aides of the interface. Therefore, the elastic (or misfit) energy can be approximated to the energy of a large angle grain boundary. Empirically, it is about a third of the Gibbs surface energy.[91] Consequently, the Gibbs interfacial elastic (or misfit) energy can be expressed by:[92]

$$G_{\langle A \rangle / \langle B \rangle}^{mis} = \frac{1}{3} \cdot \left(\frac{G_{\langle A \rangle}^{S} + G_{\langle B \rangle}^{S}}{2} \right) \qquad \text{Eq. 46}$$

The Gibbs interfacial chemical energy originates from the interactions between the interfacial atoms of crystalline phase $\langle A \rangle$ and $\langle B \rangle$. It can be described in terms of the interfacial chemical enthalpy $H_{\langle A \rangle / \langle B \rangle}^{chem}$ and the interfacial chemical entropy $S_{\langle A \rangle / \langle B \rangle}^{chem}$:

$$G_{\langle A \rangle / \langle B \rangle}^{chem} = H_{\langle A \rangle / \langle B \rangle}^{chem} - T \cdot S_{\langle A \rangle / \langle B \rangle}^{chem} \qquad \text{Eq. 47}$$

The interfacial chemical enthalpy ($H_{\langle A \rangle / \langle B \rangle}^{chem}$) can be related to the partial enthalpy of dissolution of crystalline phase $\langle A \rangle$ in crystalline phase $\langle B \rangle$ ($\Delta \bar{H}_{\langle A \rangle \, in \, \langle B \rangle}^{0}$) and crystalline phase $\langle B \rangle$ in crystalline phase $\langle A \rangle$ ($\Delta \bar{H}_{\langle B \rangle \, in \, \langle A \rangle}^{0}$) at infinite dilution. At the interface, only a fraction of 'A' ($f_{\langle A \rangle}$) is in contact with 'B', as is 'B' with 'A' ($f_{\langle B \rangle}$). As a consequence of the identical $f_{\langle A \rangle}$ and $f_{\langle B \rangle}$ ($f_{\langle A \rangle} = f_{\langle B \rangle} = 0.35$), the enthalpy contribution of the Gibbs interfacial chemical energy ($H_{\langle A \rangle / \langle B \rangle}^{chem}$) can be calculated by:[92]

$$H_{\langle A \rangle / \langle B \rangle}^{chem} = \frac{f_{\langle A \rangle} \cdot \left(\Delta \bar{H}_{\langle A \rangle \, in \, \langle B \rangle}^{0} + \Delta \bar{H}_{\langle B \rangle \, in \, \langle A \rangle}^{0} \right)}{2} \qquad \text{Eq. 48}$$

$\Delta \bar{H}_{\langle A \rangle \, in \, \langle B \rangle}^{0}$ and $\Delta \bar{H}_{\langle B \rangle \, in \, \langle A \rangle}^{0}$ are experimental available for many alloy systems [88, 99] or can be calculated based on the macroscopic atom model of Miedema.[78]

F. Sommer assumed that the formation of the interface between two different phases can be thermodynamically analog to the mixing of elements.[92] Since a further assumption was advanced that there is no change of the concentration of both elements at the interface, the main contribution to the interfacial chemical entropy can originate from the entropy due to the change of the lattice vibration upon solid solution formation.[100] Referring to [100], an identi-

cal approximation for the entropy of the vibration term can be developed according to *Debye* model. Thus, the change of the *Debye* temperature for A and B atoms at the interface ($\Delta\Theta_{\text{interf}}$) with equiatomic composition dominates the interfacial chemical entropy ($S_{\langle A\rangle/\langle B\rangle}^{\text{chem}}$):[92]

$$S_{\langle A\rangle/\langle B\rangle}^{\text{chem}} = f_{\langle A\rangle} \cdot 3R \cdot \ln \frac{\prod_j \Theta_j^{1/2}}{\sum_j 0.5 \cdot \Theta_j + \Delta\Theta_{\text{interf}}} \qquad \text{Eq. 49}$$

where Θ_j represents the *Debye* temperature of component j in the bulk crystalline phase and j is the bulk crystalline phases $\langle A\rangle$ or $\langle B\rangle$.

Based on the *Miedema* model and the experimental results, it is suggested that the change of the *Debye* temperature for A and B atoms at the interface ($\Delta\Theta_{\text{interf}}$) can be accessed by:[100]

$$\Delta\Theta_{\text{interf}} = 34.1 \times 10^{-3} \cdot \left(-\frac{\Delta H_{\langle AB\rangle}}{R}\right) \qquad \text{Eq. 50}$$

with $\Delta H_{\langle AB\rangle}$ as the enthalpy of formation of the crystalline phase $\langle AB\rangle$ solid solution and R as the gas constant.

Finally, the specific interface energy between crystalline phases $\langle A\rangle$ and $\langle B\rangle$ can be estimated from:

$$\gamma_{\langle A\rangle/\langle B\rangle}^{\text{interf}} = \frac{G_{\langle A\rangle/\langle B\rangle}^{\text{interf}}}{f_{\langle A\rangle} \cdot C_0 \cdot V_{\langle A\rangle-\langle B\rangle}^{2/3}} \qquad \text{Eq. 51}$$

Where $V_{\langle A\rangle-\langle B\rangle}$ represents the average molar volume of the crystalline phase $\langle A\rangle$ and $\langle B\rangle$.

The thermodynamic constants for the calculation of the interface energy between the crystalline Al, Si and Ge are listed in Tab. 5:

Tab. 5   The partial mixing enthalpy between the crystalline phases and their Debye temperatures

A	B	$\Delta H_{\langle A\rangle \text{ in } \langle B\rangle}^0$ (J/mol)	$\Delta H_{\langle B\rangle \text{ in } \langle A\rangle}^0$ (J/mol)	Θ_A (K)
Al	Ge	32857[96]	-3143[96]	428
Si	Al	-3143[96]	47857[96]	645
Ge	Si	3500[101]	3500[101]	374

A5   Calculations of the grain boundary energy

In a particular case, the high angle grain boundary in a crystalline phase $\langle A \rangle$ can be defined as a interface between the crystalline phase $\langle A \rangle$ and $\langle A \rangle$. Thus, the interfacial chemical contribution due to the heterogeneous crystalline phases will not be considered here anymore. Based on Eq. 45 and 46, *Z. M. Wang* et al. suggested an expression of the Gibbs grain boundary energy:[50]

$$G_{\langle A \rangle}^{\mathrm{GB}} = \frac{1}{3} \cdot G_{\langle A \rangle}^{\mathrm{S}} \qquad \mathrm{Eq.\,52}$$

Analog to the interface energy between the crystalline phases, the specific grain boundary energy of the crystalline phase $\langle A \rangle$ can be presented by:

$$\gamma_{\langle A \rangle}^{\mathrm{GB}} = \frac{G_{\langle A \rangle}^{\mathrm{S}}}{f_{\langle A \rangle} \cdot C_0 \cdot V_{\langle A \rangle}^{2/3}} \qquad \mathrm{Eq.\,53}$$

References

[1]   E. P. Donovan, F. Spaepen, D. Turnbull, J. M. Poate, and D. C. Jacobson, "Calorimetric studies of crystallization and relaxation of amorphous Si and Ge prepared by ion-implantation " *Journal of Applied Physics,* vol. 57, pp. 1795-1804, 1985.

[2]   S. Yamaguchi, N. Sugii, S. K. Park, K. Nakagawa, and M. Miyao, "Solid-phase crystallization of $Si_{1-x}Ge_x$ alloy layers," *Journal of Applied Physics,* vol. 89, pp. 2091-2095, Feb 2001.

[3]   K. Toko, I. Nakao, T. Sadoh, T. Noguchi, and M. Miyao, "Electrical properties of poly-Ge on glass substrate grown by two-step solid-phase crystallization," *Solid-State Electronics,* vol. 53, pp. 1159-1164, Nov 2009.

[4]   R. B. Bergmann, G. Oswald, M. Albrecht, and V. Gross, "Solid-phase crystallized Si films on glass substrates for thin film solar cells," *Solar Energy Materials and Solar Cells,* vol. 46, pp. 147-155, May 1997.

[5]   T. Matsuyama, N. Terada, T. Baba, T. Sawada, S. Tsuge, K. Wakisaka*, et al.*, "High-quality polycrystalline silicon thin film prepared by a solid phase crystallization method," *Journal of Non-Crystalline Solids,* vol. 198, pp. 940-944, May 1996.

[6]   C. Y. Tsao, J. W. Weber, P. Campbell, P. I. Widenborg, D. Y. Song, and M. A. Green, "Low-temperature growth of polycrystalline Ge thin film on glass by in situ deposition and ex situ solid-phase crystallization for photovoltaic applications," *Applied Surface Science,* vol. 255, pp. 7028-7035, May 2009.

[7]   K. Toko, T. Sadoh, and M. Miyao, "Indentation-induced low-temperature solid-phase crystallization of $Si_{1-x}Ge_x$ (x=0-1) on insulator," *Applied Physics Letters,* vol. 94, May 2009.

[8]   T. E. Dyer, J. M. Marshall, W. Pickin, A. R. Hepburn, and J. F. Davies, "Polysilicon produced by excimer (ARF) laser crystallization of hydrogenated amorphous-silicon (a-Si-H)," *Journal of Non-Crystalline Solids,* vol. 166, pp. 1001-1004, Dec 1993.

[9]   T. E. Dyer, J. M. Marshall, W. Pickin, A. R. Hepburn, and J. F. Davies, "Optoelectronic and structural properties of polysilicon produced by excimer-laser and furnace crystallization of hydrogenated amorphous-silicon (a-Si-H)," *Iee Proceedings-Circuits Devices and Systems,* vol. 141, pp. 15-18, Feb 1994.

[10]   W. C. Yeh, H. C. Chen, H. G. Huang, C. P. Hsiao, and J. Y. Jeng, "Superlateral growth of a-Ge film by excimer laser annealing," *Applied Physics Letters,* vol. 93, Sep 2008.

[11]   A. Slaoui, C. Deng, S. Talwar, K. J. Kramer, T. W. Sigmon, J. P. Stoquert*, et al.*, "Formation of poly-$Si_{1-x}Ge_x$ using excimer-laser processing," *Applied Surface Science,* vol. 86, pp. 346-352, Feb 1995.

[12]   L. Pereira, H. Aguas, R. M. S. Martins, P. Vilarinho, E. Fortunato, and R. Martins, "Polycrystalline silicon obtained by metal induced crystallization using different metals," *Thin Solid Films,* vol. 451, pp. 334-339, Mar 2004.

[13]   O. Nast, T. Puzzer, L. M. Koschier, A. B. Sproul, and S. R. Wenham, "Aluminum-induced crystallization of amorphous silicon on glass substrates above and below the eutectic temperature," *Applied Physics Letters,* vol. 73, pp. 3214-3216, Nov 1998.

[14]   N. Usami, M. N. Jung, and T. Suemasu, "On the growth mechanism of polycrystalline silicon thin film by Al-induced layer exchange process," *Journal of Crystal Growth,* vol. 362, pp. 16-19, Jan 2013.

[15]   F. Katsuki, K. Hanafusa, M. Yonemura, T. Koyama, and M. Doi, "Crystallization of amorphous germanium in an Al/a-Ge bilayer film deposited on a SiO2 substrate," *Journal of Applied Physics,* vol. 89, pp. 4643-4647, Apr 2001.

[16]   L. Hultman, A. Robertsson, H. T. G. Hentzell, I. Engstrom, and P. A. Psaras, "Crystallization of amorphous-silicon during thin-flim gold reaction," *Journal of Applied Physics,* vol. 62, pp. 3647-3655, Nov 1987.

[17]   E. R. Jing, B. Xiong, and Y. L. Wang, "Low-temperature wafer bonding based on gold-induced crystallization of amorphous silicon," *IEEE Electron Device Letters,* vol. 31, pp. 1011-1013, Sep 2010.

[18]   S. Sakiyama, T. Kaneko, T. Ootsubo, T. Sakai, K. Nakashima, K. Moto*, et al.*, "Enhanced Au induced lateral crystallization in electron-irradiated amorphous Ge on SiO2," *Thin Solid Films,* vol. 557, pp. 151-154, 2014.

[19]   J.-H. Park, M. Kurosawa, N. Kawabata, M. Miyao, and T. Sadoh, "Low temperature (~ 250 °C) layer exchange crystallization of $Si_{1-x}Ge_x$ (x =1–0) on insulator for advanced flexible devices," *Thin Solid Films,* vol. 520, pp. 3293-3295, 2012.

[20]   S. Y. Yoon, K. H. Kim, C. O. Kim, J. Y. Oh, and J. Jang, "Low temperature metal induced crystallization of amorphous silicon using a Ni solution," *Journal of Applied Physics,* vol. 82, pp. 5865-5867, Dec 1997.

[21]   H. Kanno, K. Toko, T. Sadoh, and M. Miyao, "Temperature dependent metal-induced lateral crystallization of amorphous SiGe on insulating substrate," *Applied Physics Letters,* vol. 89, Oct 2006.

[22]   T. Antesberger, T. A. Wassner, M. Kashani, M. Scholz, R. Lechner, S. Matich*, et al.*, "Fabrication of large-grained thin polycrystalline silicon films on foreign substrates by titanium-assisted metal-induced layer exchange," *Journal of Applied Physics,* vol. 112, Dec 2012.

[23]   Z. Yong, W. Jian, H. Qiang, and L. Dejie, "Crystallization of sputtered amorphous silicon induced by silver-copper alloy with high crystalline volume ratio," *Journal of Crystal Growth,* vol. 312, pp. 3599-3602, 1 December 2010.

[24]   Y. Matsumoto and Z. R. Yu, "P-type polycrystalline Si films prepared by aluminum-induced crystallization and doping method," *Japanese Journal of Applied Physics Part 1-Regular Papers Short Notes & Review Papers,* vol. 40, pp. 2110-2114, Apr 2001.

[25]   J. Chen, T. Sekiguchi, D. Yang, F. Yin, K. Kido, and S. Tsurekawa, "Electron-beam-induced current study of grain boundaries in multicrystalline silicon," *Journal of Applied Physics,* vol. 96, pp. 5490-5495, Nov 2004.

[26]   J. Poortmans and V. Arkhipov, *Thin film solar cells: fabrication, characterization and application.* London: John Wiley & Sons Ltd, 2006.

[27]   D. P. Gosain, A. Machida, T. Fujino, Y. Hitsuda, K. Nakano, and J. Sato, "Formation of (100)-textured Si film using an excimer laser on a glass substrate," *Japanese Journal of Applied Physics Part 2-Letters,* vol. 42, pp. L135-L137, Feb 2003.

[28] J. R. Kohler, R. Dassow, R. B. Bergmann, J. Krinke, H. P. Strunk, and J. H. Werner, "Large-grained polycrystalline silicon on glass by copper vapor laser annealing," *Thin Solid Films,* vol. 337, pp. 129-132, Jan 1999.

[29] B. Bian, J. A. Yie, B. Q. Li, and Z. Q. Wu, "Fractal formation in a-Si:H/Ag/a-Si:H films after annealing," *Journal of Applied Physics,* vol. 73, pp. 7402-7406, Jun 1993.

[30] J. H. Choi, D. Y. Kim, S. S. Kim, S. J. Park, and J. Jang, "Polycrystalline silicon prepared by metal induced crystallization," *Thin Solid Films,* vol. 440, pp. 1-4, Sep 2003.

[31] E. Stinzianni, K. Dunn, Z. Y. Zhao, M. Rane-Fondacaro, H. Efstathiadis, and P. Haldar, "Relationship of aluminum grain size to the grain size of polycrystalline silicon produced by the aluminum induced crystallization of amorphous slilicon," in *2009 34th Ieee Photovoltaic Specialists Conference, Vols 1-3*, ed New York: Ieee, 2009, pp. 1057-1062.

[32] H. Kim, D. Kim, G. Lee, and S. H. Lee, "Polycrystalline Si films formed by Al-induced crystallization (AIC) with and without Al oxides at Al/a-Si interface," *Solar Energy Materials and Solar Cells,* vol. 74, pp. 323-329, Oct 2002.

[33] O. Tuzun, J. M. Auger, I. Gordon, A. Focsa, P. C. Montgomery, C. Maurice*, et al.*, "EBSD analysis of polysilicon films formed by aluminium induced crystallization of amorphous silicon," *Thin Solid Films,* vol. 516, pp. 6882-6887, Aug 2008.

[34] J. Schneider, J. Klein, M. Muske, S. Gall, and W. Fuhs, "Aluminum-induced crystallization of amorphous silicon: preparation effect on growth kinetics," *Journal of Non-Crystalline Solids,* vol. 338, pp. 127-130, Jun 2004.

[35] B. A. Boukamp, G. C. Lesh, and R. A. Huggins, "All-solid lithium electrodes with mixed-conductor matrix," *Journal of the Electrochemical Society,* vol. 128, pp. 725-729, 1981.

[36] R. Krishnan, T. M. Lu, and N. Koratkar, "Functionally Strain-Graded Nanoscoops for High Power Li-Ion Battery Anodes," *Nano Letters,* vol. 11, pp. 377-384, Feb 2011.

[37] J. P. Maranchi, A. F. Hepp, and P. N. Kumta, "High capacity, reversible silicon thin-film anodes for lithium-ion batteries," *Electrochemical and Solid State Letters,* vol. 6, pp. A198-A201, Sep 2003.

[38] K. J. Zhao, M. Pharr, J. J. Vlassak, and Z. G. Suo, "Inelastic hosts as electrodes for high-capacity lithium-ion batteries," *Journal of Applied Physics,* vol. 109, Jan 2011.

[39] J. P. Maranchi, A. F. Hepp, A. G. Evans, N. T. Nuhfer, and P. N. Kumta, "Interfacial properties of the a-Si/Cu : active-inactive thin-film anode system for lithium-ion batteries," *Journal of the Electrochemical Society,* vol. 153, pp. A1246-A1253, 2006.

[40] T. Takamura, S. Ohara, M. Uehara, J. Suzuki, and K. Sekine, "A vacuum deposited Si film having a Li extraction capacity over 2000 mAh/g with a long cycle life," *Journal of Power Sources,* vol. 129, pp. 96-100, Apr 2004.

[41] C. K. Chan, H. L. Peng, G. Liu, K. McIlwrath, X. F. Zhang, R. A. Huggins*, et al.*, "High-performance lithium battery anodes using silicon nanowires," *Nature Nanotechnology,* vol. 3, pp. 31-35, Jan 2008.

[42] H. Wu, G. Y. Zheng, N. A. Liu, T. J. Carney, Y. Yang, and Y. Cui, "Engineering Empty Space between Si Nanoparticles for Lithium-Ion Battery Anodes," *Nano Letters,* vol. 12, pp. 904-909, Feb 2012.

[43]   I. Kovalenko, B. Zdyrko, A. Magasinski, B. Hertzberg, Z. Milicev, R. Burtovyy, *et al.*, "A Major Constituent of Brown Algae for Use in High-Capacity Li-Ion Batteries," *Science,* vol. 334, pp. 75-79, Oct 2011.

[44]   L. Baggetto, J. F. M. Oudenhoven, T. van Dongen, J. H. Klootwijk, M. Mulder, R. A. H. Niessen, *et al.*, "On the electrochemistry of an anode stack for all-solid-state 3D-integrated batteries," *Journal of Power Sources,* vol. 189, pp. 402-410, 2009.

[45]   Y. He, X. Q. Yu, Y. H. Wang, H. Li, and X. J. Huang, "Alumina-Coated Patterned Amorphous Silicon as the Anode for a Lithium-Ion Battery with High Coulombic Efficiency," *Advanced Materials,* vol. 23, pp. 4938-4941, Nov 2011.

[46]   V. Etacheri, O. Haik, Y. Goffer, G. A. Roberts, I. C. Stefan, R. Fasching, *et al.*, "Effect of fluoroethylene carbonate (FEC) on the performance and surface chemistry of Si-nanowire Li-ion battery anodes," *Langmuir,* vol. 28, pp. 965-976, Jan 2012.

[47]   J. Li, R. B. Lewis, and J. R. Dahn, "Sodium carboxymethyl cellulose - A potential binder for Si negative electrodes for Li-ion batteries," *Electrochemical and Solid State Letters,* vol. 10, pp. A17-A20, 2007.

[48]   J. X. Song, M. J. Zhou, R. Yi, T. Xu, M. L. Gordin, D. H. Tang, *et al.*, "Interpenetrated Gel polymer binder for high-performance silicon anodes in lithium-ion batteries," *Advanced Functional Materials,* vol. 24, pp. 5904-5910, Oct 2014.

[49]   D. He, J. Y. Wang, and E. J. Mittemeijer, "The initial stage of the reaction between amorphous silicon and crystalline aluminum," *Journal of Applied Physics,* vol. 97, May 2005.

[50]   Z. M. Wang, J. Y. Wang, L. P. H. Jeurgens, and E. J. Mittemeijer, "Thermodynamics and mechanism of metal-induced crystallization in immiscible alloy systems: Experiments and calculations on Al/a-Ge and Al/a-Si bilayers," *Physical Review B,* vol. 77, p. 045424, 2008.

[51]   J. P. Dismukes, R. J. Paff, and L. Ekstrom, "Lattice parameter and density in germanium-silicon alloys," *Journal of Physical Chemistry,* vol. 68, pp. 3021-&, 1964 1964.

[52]   C. A. Niedermeier, Z. Wang, and E. J. Mittemeijer, "Al-induced crystallization of amorphous Si_xGe_{1-x} (0<x<1): Diffusion, phase development and layer exchange," *Acta Materialia,* vol. 72, pp. 211-222, 2014.

[53]   W. C. Moshier, J. S. Ahearn, and D. C. Cooke, "Interaction of Al-Si, Al-Ge and Zn-Al eutectic alloys with SiC/Al discontinuously reinforced metal matrix composites," *Journal of Materials Science,* vol. 22, pp. 115-122, Jan 1987.

[54]   Z. M. Wang, L. Gu, L. P. H. Jeurgens, F. Phillipp, and E. J. Mittemeijer, "Real-time visualization of convective transportation of solid materials at nanoscale," *Nano Letters,* vol. 12, pp. 6126-6132, Dec 2012.

[55]   A. Hiraki, "Low temperature reactions at Si/metall interfaces; What is going on at the interfaces?," *Surface Science Reports,* vol. 3, pp. 357-341, 1984.

[56]   Y. H. Zhao, J. Y. Wang, and E. J. Mittemeijer, "Microstructural changes in amorphous Si/crystalline Al thin bilayer films upon annealing," *Applied Physics a-Materials Science & Processing,* vol. 79, pp. 681-690, Aug 2004.

[57]   G. A. Lopez, E. J. Mittemeijer, and B. B. Straumal, "Grain boundary wetting by a solid phase; microstructural development in a Zn-5 wt% Al alloy," *Acta Materialia,* vol. 52, pp. 4537-4545, Sep 2004.

[58]   *Electron Backscattered Diffraction: Explained*: Oxford Instruments Analytical Limited, 2004.

[59]   B. Schaffer, W. Grogger, and G. Kothleitner, "Automated spatial drift correction for EFTEM image series," *Ultramicroscopy,* vol. 102, pp. 27-36, Dec 2004.

[60]   E. Pihan, A. Slaoui, and C. Maurice, "Growth kinetics and crystallographic properties of polysilicon thin films formed by aluminium-induced crystallization," *Journal of Crystal Growth,* vol. 305, pp. 88-98, Jul 2007.

[61]   A. Bary and G. Nouet, "Electrical activity of the 1st order and 2nd order twins and grain boundaries in silicon," *Journal of Applied Physics,* vol. 63, pp. 435-438, Jan 1988.

[62]   P. Sonnweber-Ribic, "Grain growth and texture evolution in copper thin films," Doctor, Max-Planck-Institute für Metallforschung Stuttgart, University Stuttgart, Stuttgart, 2010.

[63]   J. M. Zhang, K. W. Xu, and V. Ji, "Dependence of strain energy on the grain orientations in an FCC-polycrystalline film on rigid substrate," *Applied Surface Science,* vol. 185, pp. 177-182, Jan 2002.

[64]   H. P. Strunk and F. Qu, "Method for producing a porous nanocrystalline semiconductor layer, porous nanocrystalline semiconductor layer, use thereof, anode, and secondary lithium-ion battery," WO/2015/096854, 2015.

[65]   F. Qu, C. L. Li, Z. M. Wang, H. P. Strunk, and J. Maier, "Metal-induced crystallization of highly corrugated silicon thick films as potential anodes for Li-ion batteries," *Acs Applied Materials & Interfaces,* vol. 6, pp. 8782-8788, Jun 2014.

[66]   Z. M. Wang, L. P. H. Jeurgens, J. Y. Wang, and E. J. Mittemeijer, "Fundamentals of metal-induced crystallization of amorphous semiconductors," *Advanced Engineering Materials,* vol. 11, pp. 131-135, Mar 2009.

[67]   T. N. Nguyen, S. Jung, and J. Yi, "Advanced solid-phase crystallization of amorphous silicon on a glass substrate," *Journal of the Korean Physical Society,* vol. 54, pp. 2367-2372, Jun 2009.

[68]   J. Y. Wang, Z. M. Wang, and E. J. Mittemeijer, "Mechanism of aluminum-induced layer exchange upon low-temperature annealing of amorphous Si/polycrystalline Al bilayers," *Journal of Applied Physics,* vol. 102, Dec 2007.

[69]   F. Qu, C. L. Li, Z. M. Wang, Y. R. Wen, G. Richter, and H. P. Strunk, "Eutectic nano-droplet template injection into bulk silicon to construct porous frameworks with concomitant conformal coating as anodes for Li-ion batteries," *Scientific Reports,* vol. 5, p. 11, May 2015.

[70]   B. Philippe, R. Dedryvere, M. Gorgoi, H. Rensmo, D. Gonbeau, and K. Edstrom, "Improved performances of nanosilicon electrodes using the salt LiFSI: A photoelectron spectroscopy study," *Journal of the American Chemical Society,* vol. 135, pp. 9829-9842, Jul 2013.

[71]   E. Paparazzo, "XPS, AES and EELS studies of Al surfaces," *Vacuum,* vol. 62, pp. 47-60, May 2001.

[72]   C. D. Wanger, W. M. Riggs, L. E. Davis, J. F. Moulder, and G. E. Muilenberg, *Handbook of X-ray photoelectron spectroscopy* vol. 3: Heyden & Son Ltd., 1981.

[73]   C. C. Ahn and O. L. Krivanek, *A reference guide of electron energy loss spectra covering all stable element*. Warrendale: Gatan, Inc., 1983.

[74]   D. B. Williams and C. B. Carter, *Transmission Electron Microscopy: a textbook for materilas science*. New York: Springer Press, 1996.

[75]   N. Liu, H. Wu, M. T. McDowell, Y. Yao, C. M. Wang, and Y. Cui, "A yolk-shell design for stabilized and scalable Li-ion battery alloy anodes," *Nano Letters,* vol. 12, pp. 3315-3321, Jun 2012.

[76]   P. Limthongkul, Y. I. Jang, N. J. Dudney, and Y. M. Chiang, "Electrochemically-driven solid-state amorphization in lithium-silicon alloys and implications for lithium storage," *Acta Materialia,* vol. 51, pp. 1103-1113, Feb 2003.

[77]   B. Straumal, O. Kogtenkova, S. Protasova, A. Mazilkin, P. Zieba, T. Czeppe*, et al.*, "Wetting and premelting of triple junctions and grain boundaries in the Al-Zn alloys," *Materials Science and Engineering a-Structural Materials Properties Microstructure and Processing,* vol. 495, pp. 126-131, Nov 2008.

[78]   R. B. F. R. de Boer, W. C. M. Mattens, A. R. Miedema, A. K. Niessen, *Cohesion in Metals: Transition Metals alloys*. Amsterdam: North Holland, 1988.

[79]   S. Ranganathan, R. Divakar, and V. S. Raghunathan, "Interface structures in nanocrystalline materials," *Scripta Materialia,* vol. 44, pp. 1169-1174, May 2001.

[80]   Y. Chen and C. A. Schuh, "Contribution of triple junctions to the diffusion anomaly in nanocrystalline materials," *Scripta Materialia,* vol. 57, pp. 253-256, Aug 2007.

[81]   Y. Du, Y. A. Chang, B. Y. Huang, W. P. Gong, Z. P. Jin, H. H. Xu*, et al.*, "Diffusion coefficients of some solutes in fcc and liquid Al: critical evaluation and correlation," *Materials Science and Engineering a-Structural Materials Properties Microstructure and Processing,* vol. 363, pp. 140-151, Dec 2003.

[82]   K. Hirano and S. Fujikawa, "Impurity diffusion in aluminum," *Journal of Nuclear Materials,* vol. 69-7, pp. 564-566, 1978.

[83]   M. Legros, G. Dehm, E. Arzt, and T. J. Balk, "Observation of giant diffusivity along dislocation cores," *Science,* vol. 319, pp. 1646-1649, Mar 2008.

[84]   J. Y. Wang and E. J. Mittemeijer, "A new method for the determination of the diffusion-induced concentration profile and the interdiffusion coefficient for thin film systems by Auger electron spectroscopical sputter depth profiling," *Journal of Materials Research,* vol. 19, pp. 3389-3397, Nov 2004.

[85]   Y. Chen and C. A. Schuh, "Geometric considerations for diffusion in polycrystalline solids," *Journal of Applied Physics,* vol. 101, Mar 2007.

[86]   Z. B. Wang, N. R. Tao, W. P. Tong, J. Lu, and K. Lu, "Diffusion of chromium in nanocrystalline iron produced by means of surface mechanical attrition treatment," *Acta Materialia,* vol. 51, pp. 4319-4329, Aug 2003.

[87]   H. Stohr and W. Klemm, "On two-component systems with germanium I Germanium/aluminium, germanium/tin and germanium/silicon," *Zeitschrift Fur Anorganische Und Allgemeine Chemie,* vol. 241, pp. 305-323, Jun 1939.

[88]   P. D. D. R. Hultgren, D. T. Hawkins, M. Gleiser, K. K. Kelley, *Selected values of the thermodynamic properties of binary alloys*. Ohio: Am. Soc. Met., Metals Park, 1973.

[89]   H. S. Chen and D. Turnbull, "Specific heat and heat of crystallization of amorphous germanium," *Journal of Applied Physics,* vol. 40, pp. 4214-&, 1969.

[90]   F. Spaepen, "Configurational entropy of amorphous Si and Ge," *Philosophical Magazine,* vol. 30, pp. 417-422, 1974.

[91]   A. R. Miedema and R. Boom, "Surface tension and electron density of pure liquid metals," *Zeitschrift Fur Metallkunde,* vol. 69, pp. 183-190, 1978.

[92]   F. Sommer, R. N. Singh, and E. J. Mittemeijer, "Interface thermodynamics of nano-sized crystalline, amorphous and liquid metallic systems," *Journal of Alloys and Compounds,* vol. 467, pp. 142-153, Jan 2009.

[93]   H. Wawra, "Surface energy of solid materials as measured by ultrasonic and conventional test methods 1," *Zeitschrift Fuer Metallkunde,* vol. 66, pp. 395-401, 1975.

[94]   T. Iida and R. I. L. Guthrie, *The Physical Properties of Liquid Metals*. Oxford: Clarendon, 1988.

[95]   S. Hara, S. Izumi, T. Kumagai, and S. Sakai, "Surface energy, stress and structure of well-relaxed amorphous silicon: A combination approach of ab initio and classical molecular dynamics," *Surface Science,* vol. 585, pp. 17-24, Jul 2005.

[96]   *CRC Handbook of Chemistry and Physics*, 85 ed. Boca Raton: CRC, 2004.

[97]   R. Benedictus, A. Bottger, and E. J. Mittemeijer, "Thermodynamic model for solid-state amorphization in binary systems at interfaces and grain boundaries," *Physical Review B,* vol. 54, pp. 9109-9125, Oct 1996.

[98]   V. S. Sudavtsova and V. G. Kudin, "Thermodynamic properties of Si-Ge and Si-Sn melts," *Inorganic Materials,* vol. 37, pp. 319-320, Apr 2001.

[99]   A. R. Miedema, "Formation enthalpy of monovacancies in metals and intermetallic compounds," *Zeitschrift Fur Metallkunde,* vol. 70, pp. 345-353, 1979.

[100]   F. Sommer, R. N. Singh, and V. Witusiewicz, "On the entropy of mixing," *Journal of Alloys and Compounds,* vol. 325, pp. 118-128, Jul 2001.

[101]   G. J. A. R. W. Olesinski, *The Ge-Si (Germainium-Silicon) System* vol. 5: Springer, 1984.

Danksagung

Statement

I hereby certify that the dissertation entitled:

‚Aluminum-induced Crystallization of Semiconductor Thin Films'

is entirely my own work except where otherwise indicated. Passages and ideas from other sources have been clearly indicated.

Ich versichere, dass ich die vorliegende Arbeit mit dem Titel:

‚Aluminum-induced Crystallization of Semiconductor Thin Films'

selbständig verfasst und keine anderen als die angegebenen Quellen und Hilfsmittel benutzt habe; aus fremden Quellen entnommene Passagen und Gedanken sind als solche kenntlich gemacht.

Ort/Datum   Unterschrift